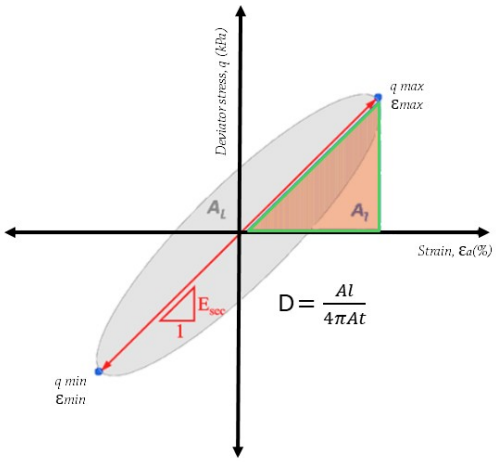

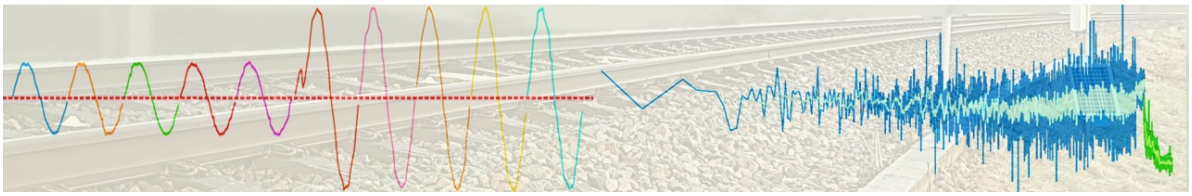

Effect of cyclic loading on stiffness degradation of Lime cement mixed clays for railway embankment

A comparative study on Swedish natural clay and stabilized clay

Master's thesis in the Master's Programme Infrastructure and Environmental Engineering

ZAKI ALZAKI
MUHAMMAD ASAD

DEPARTMENT OF ARCHITECTURE AND CIVIL ENGINEERING
DEVISION OF GEOLOGY AND GEOTECHNICS

CHALMERS UNIVERSITY OF TECHNOLOGY
Master's thesis ACEX30
Gothenburg, Sweden 2024

MASTER'S THESIS ACEX30

Effect of cyclic loading on stiffness degradation of Lime cement mixed clays for railway embankment

A comparative study on Swedish natural clay and stabilized clay

Master's Thesis in the Master's Programme Infrastructure and Environmental Engineering

ZAKI ALZAKI
MUHAMMAD ASAD

Department of Architecture and Civil Engineering
Division of Geology and Geotechnics
CHALMERS UNIVERSITY OF TECHNOLOGY
Gothenburg, Sweden 2024

Effect of cyclic loading on stiffness degradation of Lime cement mixed clays for railway embankment
A comparative study on Swedish natural clay and stabilized clay

Master's Thesis in the Master's Programme Infrastructure and Environmental Engineering

ZAKI ALZAKI
MUHAMMAD ASAD

Examensarbete ACEX30
Institutionen för Arkitektur och Samhällsbyggnadsteknik
Chalmers Tekniska Högskola, 2024

Department of Architecture and Civil Engineering
Division of Geology and Geotechnics
Chalmers University of Technology
SE-412 96 Göteborg
Sweden
Telephone +46 31 772 1000

Cover:
Top left: GDS Dynamic Triaxial Testing System, adapted from the website (Link) and GDS LVDT local strain transducer, adapted from the website (Link).
Top right: The figure shows the Stress-strain loop and the damping ratio equation.
Bottom left: The background photo is a railway embankment in Aarhus, Denmark, adapted from the website (Link) and the foreground figure shows the cycles of the deviatoric stress over time. For more details,refer to the section 3.2.2.
Bottom right: The figure shows the results of damping ratio (D) for LCC03 in global transducer case. For more details,refer to the section 4.2.

Department of Architecture and Civil Engineering
Göteborg, Sweden, 2024

Effect of cyclic loading on stiffness degradation of Lime cement mixed clays for railway embankment
A comparative study on Swedish natural clay and stabilized clay

Master's thesis in the Master's Programme Infrastructure and Environmental Engineering

ZAKI ALZAKI

MUHAMMAD ASAD

Department of Architecture and Civil Engineering
Division of Geology and Geotechnics
Chalmers University of Technology

ABSTRACT

Railway embankments in Sweden are subject to significant settlements caused by repeated cyclic loading from train movements, resulting in alignment issues and substantial maintenance expenses. The leading cause of embankment degradation is the dynamic response of natural soft soils to prolonged train-induced loading, leading to evolving soil stiffness properties over time. Ground improvement techniques, such as lime cementation of clays, have shown promise in enhancing soil conditions. However, the dynamic stiffness properties of these improved soils still uncertain under repeated loading cycles.

This research project investigated the dynamic stiffness properties of lime cement mixed clays (LCC) and conducted a comprehensive comparative study with properties of natural clays (NC) by using a developed Python tool a significant advancement in the field. Furthermore, IQR method was utilized as a pre-processing step to filter outliers, enhancing the analysis's effectiveness and reliability. The research involved undrained cyclic triaxial testing of clay samples at Chalmers Geotechnical Lab, with cyclic data collection using GDSlab software. Advanced data pre-processing techniques were employed to refine the cyclic raw data and extract critical cycle stage information for each test. The tool's automation facilitates accurate computation of stiffness parameters, such as damping ratio (D), secant stiffness modulus (E), and secant shear modulus (G), under varying cyclic loading (q_{cyc}) and stress-strain conditions. The investigation also addresses the uncertainties inherent in laboratory measurements by calculating propagation errors to determine their impact on the calculations of the stiffness parameter. The cyclic response under undrained conditions exhibits complex, non-linear stress-strain behavior.

The findings revealed a slight trend in the stiffness parameters (D), (E), and (G) for LCC samples with two local cycle amplitudes, accompanied by an unclear trend with four global cycle amplitudes, which reflect the quality of those measurements. In contrast, the NC samples, which underwent four global cycle amplitudes, exhibited a distinct trend in the parameters, indicating a clear degradation within the sample.

Keywords: Cyclic loading, Lime Cement, Clay, Stiffness modulus, Shear modulus, Ellipse, Cycle amplitude, CSR, IQR

Effekt av cyklisk belastning på styvhetsnedbrytning av kalk-cementblandade leror för järnvägsbankar
En jämförande studie av svensk naturlig lera och stabiliserad lera

Examensarbete inom masterprogrammet Master

ZAKI ALZAKI

MUHAMMAD ASAD

Institutionen för arkitektur och samhällsbyggnadsteknik
Avdelningen för Geologi och Geoteknik
Chalmers tekniska högskola

SAMMANFATTNING

Järnvägsbankar i Sverige utsätts för avsevärda sättningar orsakade av upprepade cykliska belastningar från tågrörelser, vilket resulterar i linjeproblem och betydande underhållskostnader. Den främsta orsaken till banknedbrytning är den dynamiska responsen hos naturliga, mjuka jordar på långvarig tåginducerad belastning, vilket leder till förändrade jordstyvhetsegenskaper över tid. Markförbättringstekniker, såsom kalkcementering av leror, har visat lovande resultat för att förbättra jordens egenskaper. De dynamiska styvhetsegenskaperna hos dessa förbättrade jordar är dock fortfarande osäkra under upprepade lastcykler.

Detta forskningsprojekt undersökte de dynamiska styvhetsegenskaperna hos kalkcementblandade leror (LCC) och genomförde en omfattande jämförande studie med egenskaper hos naturliga leror (NC) genom att använda ett utvecklat Python-verktyg, vilket utgör en betydande framgång inom området. Vidare användes IQR-metoden som ett förbehandlingssteg för att filtrera bort avvikelser, vilket förbättrar analysens effektivitet och tillförlitlighet. Forskningen omfattade odränerad cyklisk triaxialprovning av lerprover vid Chalmers Geotekniska Laboratorium, där cyklisk data samlades in med hjälp av GDSlab-programvara. Avancerade dataförbehandlingstekniker användes för att förfina de cykliska rådata och extrahera kritisk information om cyklstadier för varje test. Verktygets automatisering underlättar noggrann beräkning av styvhetsparametrar såsom dämpningsförhållande (D), sekantstyvhetsmodul (E) och sekantskjuvmodul (G) under olika cykliska belastnings- (q_{cyc}) och spännings-töjningsförhållanden. Undersökningen behandlar även de osäkerheter som är inneboende i laboratoriemätningar genom att beräkna propageringarfel för att bestämma deras påverkan på beräkningarna av styvhetsparametern. Den cykliska responsen under odränerade förhållanden uppvisar ett komplext, icke-linjärt spännings-töjningsbeteende.

Resultaten avslöjade en svag trend i styvhetsparametrarna (D), (E) och (G) för LCC-prover med två lokala cykelamplituder, åtföljt av en oklar trend med fyra globala cykelamplituder, vilket återspeglar kvaliteten på dessa mätningar. Däremot uppvisade NC-proverna, som genomgick fyra globala cykelamplituder, en tydlig tendens i parametrarna, vilket indikerar en klar nedbrytning inom provet.

Nyckelord: Cyklisk belastning, Kalkcement, Lera, Styvhetsmodul, Skjuvmodul, Ellips, Cykelamplitud, CSR, IQR

Contents

Preface

This Master's thesis was carried out at Chalmers University of Technology at the Division of Geology and Geotechnics during the spring semester of 2024.

We would like to express our gratitude to our supervisors, Ayman Abed and Dawn Yun-Cheng Wong, for their invaluable guidance throughout this project. Your insightful feedback and valuable contacts have significantly contributed to the success of our work. We also wish to thank our examiner Jelke Dijkstra for his guidance and providing us with the opportunity to conduct this study.

Furthermore, we would like to extend our gratitude to Chalmers laboratory staff who provided calibration data and information on uncertainties associated with triaxial sensors, which facilitated the calculation of propagation error for the project results.

It is our hope that this project serves as a precursor to more subsequent projects that will investigate stabilized clay more thoroughly.

Zaki Alzaki & Muhammad Asad
Gothenburg, June 2024

Nomenclature / Notations

Roman letters

u	Track modulus	$[Pa]$
k	Track stiffness	$[Pa]$
D	Damping ratio	$[-]$
q	Deviatoric stress	[kPa]
ν	Poisson's ratio	$[-]$
P'	Effective mean pressure	[kPa]
$P_{o'}$	Effective confining pressure	[kPa]
e	Void ratio	$[-]$
e_o	Void ratio at start of loading	$[-]$
s_t	Sensitivity	$[-]$
s_u	Undrained shear strength	[Pa]
$s_{u_{\text{avg}}}$	Average undrained shear strength	[Pa]
w_N	Natural water content	[%]
LL	Liquid limit	[%]
PL	Plastic limit	[%]
PI	Plastic index	[%]
T	Time period of cycles	[s]
q_o	In-situ deviatoric stress	[kPa]
q_p	Pre-shearing amplitude	[%]
q_{avg}	Average deviatoric stress in cyclic loading	[kPa]
q_m	Intial deviatoric stress in cyclic loading	[kPa]
q_f	Peak deviatoric stress	[kPa]
u	Porewater pressure	[kPa]
t_g	Geologic age	[Yr]
v_s^2	Shear wave velocity	$[\text{ms}^{-1}]$
u_p	Permanent component of porepressure	[Pa]
u_{cy}	Cyclic component of porepressure	[Pa]
q_{cyc}	Cyclic loading amplitude	[kPa]
G_{sec}	Secant shear's modulus	[MPa]
G_{o}	Initial shear's modulus	[MPa]
G_{50}	Global Secant shear's modulus	[MPa]
G_{max}	Maximum shear's modulus	[MPa]
G/G_{max}	Normalized shear's modulus	$[-]$
G_{sec}/G_{o}	Normalized stiffness degradation	$[-]$
N	Number of cycles	$[-]$
r	constant	$[-]$
E_{50}	Global Secant Young's modulus	[MPa]
E_{local}	Local Secant Young's modulus	[MPa]
E_{max}	Maximum Young's modulus	[MPa]
H_0	Initial height of the specimen	[mm]
Lg	Initial length of gauge	[mm]
F	Axial loads applied on the specimen	[kN]
D	Initial diameter of specimen	[mm]

A_0	Initial area of specimen	$[\mathrm{mm}]$
ΔA	Loop area	$[-]$
A	Triangle area	$[-]$
ΔH	Change in the height of the specimen during global strain	$[\mathrm{mm}]$
Δu	Porewater pressure change	$[\mathrm{kPa}]$
Δh	Change in the height of the specimen during local strain	$[\mathrm{mm}]$
P	Vertical force exerted by train wheel	$[\mathrm{kN}]$
$Ru_{d\cdot global}$	Relative uncertainty in axial displacement transducer for global strain	$[\%]$
$Ru_{d\cdot local}$	Relative uncertainty in axial displacement transducer for local strain	$[\%]$
Ru_l	Relative uncertainty in axial loading sensor	$[\%]$
Ru_w	Relative uncertainty in pore pressure trandsucer	$[\%]$
Ru_c3	Relative uncertainty in cell pressure pump	$[\%]$
$q_{max_{\text{(LCC)}}}$	Maximum critical stress limit for LCC	$[kPa]$
$q_{max_{\text{(NC)}}}$	Maximum critical stress limit for NC	$[kPa]$
R_ε	Strain resistance	$[-]$
M_ε	Strain resistance number	$[-]$

Greek letters

λ	Damping ratio	$[-]$
δ_m	Maximum rail deflection	$[\mathrm{m}]$
δ_n	Degradation index	$[-]$
δ_v	Uncertainty error of vernier caliper	$[\%]$
t	Degradation parameter	$[\mathrm{s}]$
σ_1	Major principal stress	$[\mathrm{kPa}]$
σ_3	Minor principal stress	$[\mathrm{kPa}]$
σ_i	Principal stress in the ith direction	$[\mathrm{kPa}]$
σ'	Effective stress	$[\mathrm{kPa}]$
σ_a	Axial compressive stress	$[\mathrm{kPa}]$
σ_r	Radial compressive stress	$[\mathrm{kPa}]$
ε_a	Axial compressive strain	$[\%]$
ε_r	Radial compressive strain	$[\%]$
ε_{ar}	Recoverable rebound strain	$[\%]$
ε_{ap}	Non-recoverable accumulated plastic strain	$[\%]$
ε_{at}	Total strain	$[\%]$
ε_{peak}	Peak strain	$[\%]$
$\varepsilon_{aN,max}$	Maximum axial strain	$[\%]$
$\varepsilon_{aN,min}$	Minimum axial strain	$[\%]$
ε_d	Dynamic strain	$[\%]$
τ	Shear stress	$[\mathrm{kPa}]$
γ	Shear strain	$[\%]$
τ_{cy}	Cyclic shear stress	$[\mathrm{kPa}]$
τ_a	Constant shear stress	$[\mathrm{kPa}]$
γ_{cy}	Cyclic shear strain	$[\%]$
γ_p	Permanent shear strain	$[\%]$
γ_n	Natural unit weight	$[\mathrm{kNm}^{-3}]$
α	Inclination of ellipse major axis	[Degree]

s_{ij}	Deviatoric stress tensor	$[\mathrm{kPa}]$
de^p_{ij}	Deviatoric strain tensor	$[\%]$
Δe^p	Plastic component of void ratio change due to loading	$[-]$
ε^p_v	Plastic volumetric strain	$[-]$
$\overline{\varepsilon}^p$	Plastic shear distortions	$[-]$
c_u	shear strength	$[\mathrm{kPa}]$
σ_x	Axial stress	$[\mathrm{kPa}]$
ρ_T	Clay mass density	$[\mathrm{kgm}^{-3}]$
ρ_b	Bulk density	$[\mathrm{kNm}^{-3}]$
ε_{cu}	cumulative strain	$[\%]$
m_ε	dimensionless resistance number	$[-]$
δ_v	Uncertainty error in Vernier caliper	$[\%]$
$\Delta\sigma$	Increment of axial stress	$[\mathrm{kPa}]$
$\Delta\varepsilon$	Increment of axial strain	$[\%]$
$\Delta\tau$	Increment of shear stress	$[\mathrm{kPa}]$
$\Delta\gamma$	Increment of shear strain	$[\%]$

Abbreviations

CSR	Cyclic Stress Ratio
LCC	Lime Cement Clay
NC	Natural Clay
SLS	Serviceability Limit State
OCR	Over Consolidated Ratio
CSSM	Critical State Soil Mechanics
DDM	Dry Deep Mixing
USCS	Unified Soil Classification System
GDSTTS	GDS Triaxial Testing System
LVDTs	Linear Variable Differential Transducers
SEM	Scanning Electron Microscope
CMS	Cement Mixed Soils
RMS	Remolded Mixed Soils
FC	Fine Content
CH	Highly Plastic Clay
XCT	X-Ray Computed Tomography
IQR	Inter-Quartile Range
VC	Vernier Caliper
FS	Factor of Safety

1 Introduction

Railways provide an excellent transportation option due to their environmental friendliness, cost-effectiveness, efficiency, and safety compared to other methods (Roshan et al., 2022). The past few decades have seen a surge in high-speed rail infrastructure due to its inherent advantages (Fernández-Ruiz et al., 2022). Amid rapid growth in transportation, coastal railway and subway projects are increasingly being constructed on soft ground (Liu et al., 2022). Railway projects on cohesive soil often experience post-construction embankment subsidence due to the degradation of soft clay, which is influenced by weather and the dynamic loads from moving trains (Roshan et al., 2022). In developed countries, track maintenance is the dominant operational cost for extensive railway networks (Tahershamsi et al., 2023). Railway operators allocate significant annual funding to maintain and renew extensive tracks. According to the report by Trafikverket, it is estimated that Sweden will need to allocate SEK 30 billion for the maintenance of its railway infrastructure from 2022 to 2033 (Anna Wildt, P, 2021). The Swedish rail network requires maintenance and modernization to ensure operational efficiency and safety standards (Trafikverket, 2021).

Roshan et al., states that the track deformations originate from the granular materials in the ballast and sub-ballast, as well as the soil properties of the subgrade. The soil type used in subgrade and embankment construction is critical to railway track degradation. Weak, soft, collapsible soil increases system failure risk. The response of dynamic soil properties over time is significantly impacted by its sensitivity, anisotropy, bonding, and rate dependence under varying cyclic loads (Zuada Coelho et al., 2021). The authors (Dijkstra et al., 2019), in the technical report have acknowledged that repeated cyclic loads by railway structures over time induce gradual settling and degradation of railway tracks in soft soil (natural clays) by changing their behavior. This can specifically lead to fluctuations in the soil's dynamic properties (damping & secant stiffness) due to varying levels of excessive porewater pressure within the soil. This generates problems such as track alignment issues, disruption to the railway network, and high track maintenance costs.

Therefore, it is important to stabilize such soft soil with the help of some binding agents (lime and cement). Literature studies mainly focused on the changes in the mechanical properties of lime-cement-mixed clays (LCC). However, more research needs to be done on how these clays respond to dynamic cyclic loading in terms of stiffness degradation. Additionally, there is a lack of available data on how the dynamic stiffness properties of Swedish clays are affected under improved soil conditions. The cyclic degradation of soft soils is a complex phenomenon that requires understanding multiple influencing parameters (Staubach et al., 2022). The cyclic raw data was obtained from the Chalmers triaxial setup upgraded with local instruments for small and large loading amplitudes. Previous studies, such as (Tahershamsi et al., 2023), have provided experimental validation for the impact of cyclic loading on the dynamic properties of soft natural clay, particularly Swedish-sensitive clays.

However, a significant research gap exists in studying the impact of dynamic cyclic loading on lime-cement mixed clays (LCC). Therefore, it is essential to address this gap through further research. This would involve explicitly studying the raw data of Swedish-sensitive natural clay (NC) and lime-cement mixed clay (LCC) together to

understand the evolution of their dynamic stiffness properties.

1.1 Aims and objectives

The primary aim of this project is to conduct a comprehensive study on the degradation behavior of two types of clay samples, stabilized clay (LCC), and natural clays (NC). These clays are commonly encountered in railway embankments. By subjecting them to cyclic triaxial loading conditions in the laboratory, the aim is to evaluate their stiffness response and compare their performance. To achieve this, an automated Python-based tool will be developed. The focus will be on understanding the underlying mechanisms that govern the degradation process in clays. Specifically, the interest is to investigate how various intricate cyclic loading components — such as stress and strain amplitudes, loading amplitudes, and cycle numbers — affect stiffness degradation.

To accomplish the specified aims, the research is driven by four sub-objectives.

1. Develop an automated Python-based pre-processing tool for cyclic raw data acquired from the Chalmers Geotechnical Lab.
2. Estimate the systematic propagation error in uncertainties associated with laboratory measurements by utilizing calibration data of the triaxial setup.
3. Investigate and compare the cyclic degradation behavior of LCC clays with that of NC soft clays based on different cyclic loading amplitudes applied during the cyclic triaxial test by using the Python tool.
4. Investigating the proximity of samples to failure behavior by estimating strain resistance.

1.2 Assumptions and Limitations

The following are the assumptions and limitations stated for the project study.

1. Only a single sample of lime-cementation clay was utilized to analyze stiffness degradation in the local transducer case.
2. The Poisson's ratio $\nu = 0.2$ was assumed for both sample types, LCC and NC, based on the previous projects for the same soil in the area.
3. The project assumed the value of undrained shear strength (s_u) from unconfined compressive strength values (q_u) from the UCS monotonic test based on the previous project for the same soil in the area.
4. The stress-strain loop was approximated to resemble the ellipse-fitting model closely.
5. The cyclic amplitudes (q_{cyc}) used for LCC samples were very small for the thorough investigation of stiffness degradation.
6. There was no available data for local transducers for NC samples, making it difficult to compare with LCC local transducer case data.

2 Background

2.1 Degradation of track infrastructure

2.1.1 Serviceability limit state, SLS

The serviceability limit state (SLS) refers to a point in structural engineering at which the structure does not fulfill the requirements for its intended use. During the research Roshan et al. (2022), identified permanent deformation/strain as a frequent challenge in railway track management. The SLS designs tolerate overall settlement but may allow for differential settlements within limits (Randolph & Gourvenec, 2017). Some overall settlements are unavoidable, they must also be checked within acceptable limits to control issues such as alignment and track geometry degradation. It mainly addresses (SLS) concerns (Tahershamsi et al., 2023). Larsson (2021) in his study emphasized the importance of time-dependent deformation properties for SLS calculations. Settlements lead to track alignment issues, which lead to time and money spent on repairing them before the train can run on the track again. Therefore, ensuring the serviceability limit state (SLS) for railway track infrastructure is very important. Railway embankment design prioritizes track serviceability, considering train loads, embankment geometry, and site geotechnics to manage differential settlement (Bogusz & Godlewski, 2019).

2.1.2 Railway track and foundation

Most of Sweden's railway embankments were constructed in the late 19th century (Lundström & Dehlbom, 2019). Historical embankments had limited reinforcement options, unlike modern methods involving piling and ground improvement. Linear structural alignment and layout problems, like those involving railway tracks, have drawn a lot of attention in the last few years (Guler et al., 2011; Nielsen & Li, 2018). Because of cumulative deformations from cyclic loads and decreased load-bearing capacity, railway tracks deteriorate (Esveld, 2001). When it comes to managing vibrations and settlements on railway embankments, stiffness is more important than strength (Wong et al., 2023).

Railway tracks consist of two main components: the permanent way (Superstructure) and the foundation (Substructure) (Lazorenko et al., 2019). The cross-section of a railway track is shown in Figure 2.1. The superstructure includes (rails, sleepers, pads, fasteners), while the substructure comprises (ballast, sub-ballast, subgrade) (Riyad et al., 2021). Dense railway tracks utilize ballast and sub-ballast layers to support rails and sleepers (Bharti & Dixit, 2019). In other words, ballastless tracks, with a concrete base, show less settlement than ballasted tracks, where granular layers with large voids cause more deformation (Roshan et al., 2022). Railway tracks on soft soils like peat, clay, or silt can deform and deteriorate, posing a high risk of derailment (Zhang et al., 2023). Bogusz and Godlewski (2019) in their article have discussed the railway soil-structure interaction and stability issues impacted by operational traffic load. They recommended safety factors of 2.0, 1.5, and 1.3 for new, operational, and post-maintenance railway tracks, respectively.

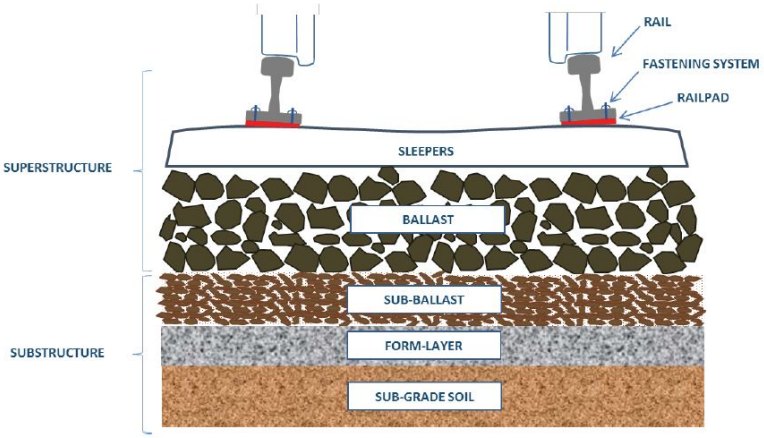

Figure 2.1: *Illustration of a railway track's cross-section and foundation, depicting the ballast and formation layers, adapted from Luca Pirozzolo (2017)*

In their research, Selig and Li (1994) explained the impact of track modulus (u) and track stiffness (k) on rail foundation health and performance. Quantifying these parameters and understanding their influencing factors for track assessment and improvement is crucial. The rail can be observed as a continuous beam on a flexible foundation, as shown in Figure 2.2. A train wheel exerts a vertical force, P, causes maximum rail deflection, δm, beneath the wheel.

The track stiffness (k) and track modulus (u) defined by Selig and Li (1994), are as follows:

$$k = \frac{P}{\delta_m} \tag{2.1}$$

Track modulus (u) quantifies the foundation's support for the rail, calculated by dividing the vertical foundation force (q) by the rail length.

$$u = -\frac{q}{\delta} \tag{2.2}$$

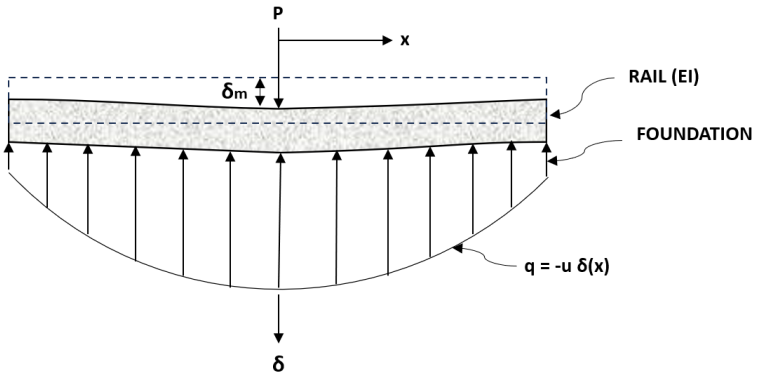

Figure 2.2: *Rail beam on an elastic foundation model redeveloped from, Selig and Li (1994)*

2.2 Gothenberg's natural clay, NC

The widespread occurrence of sensitive clay in the Nordic region has a profound impact on construction, particularly in densely populated areas near rivers and coasts. According to the study by Birmpilis and Dijkstra (2021), these clays display unique behaviors under stress, such as anisotropy and sensitivity to temperature and loading rate, resulting in reduced stiffness. Their high water content and void ratio often exceed the liquid limits measured in laboratory tests. Tornborg et al. (2021), reported that the geology of the Gota River valley mainly consists of soft, sensitive clay that formed after the last ice age. These deep clay layers, which can be as deep as 100 meters, are particularly prevalent in central Gothenburg. The clay's bulk density (γ_b) ranges from 15 kNm^{-3} at the surface to 18 kNm^{-3} at greater depths, and its sensitivity varies between 10 and 25. The clay displays anisotropic behavior and becomes softer under strain. Obtaining accurate laboratory measurements of its stiffness parameters is difficult due to the potential disruption of the clay's natural structure during sample collection, storage, preparation, and testing.

The clays in this area have a complex, directionally variable (anisotropic) structure and are over-consolidated (OCR < 2). They exhibit time-dependent viscosity (thixotropic behavior), a non-linear stress-strain relationship, and are sensitive to loading rates. Significant creep effects result in gradual deformation, compromising the area's stability (Wood & Karstunen, 2022).

2.3 Lime-cement stabilisation, LCC

Gothenburg's clay presents serious financial and safety risks for building projects. Nagaraj and Miura (2001), propose a method of improving the engineering properties of soft clay by strengthening the soil bonding with the addition of cementing agents. Larsson (2021) investigated unconfined compressive strength tests in his conference paper. He discovered that some binders steadily increase soil strength, while others only work best with particular kinds of soil. To improve soil bonding and increase the load-bearing capacity of soft clays, engineers employ chemical treatments, deep mixing, jet grouting, mass stabilization, and other engineering approaches (D. Wang & Korkiala-Tanttu, 2020).

For more than 45 years, Sweden has implemented the "Nordic dry deep mixing (DDM)" in-situ technique to enhance soil quality. This method involves the use of compressed air to blend binders such as cement and lime. During the 1980s, lime columns were predominantly used to mitigate ground settlement and stabilize embankments. The SGF 2000 guidelines from the Swedish Geotechnical Society state that soil columns of enhanced quality should exhibit a critical undrained shear stress of 100 kPa and compressive strength of 300 kPa to ensure serviceability limit state, SLS. However, actual field strengths often exceed these specified values (Larsson, 2021).

The addition of cement considerably enhances the bearing capacity and compressive strength of stabilized marine soils. D. X. Wang et al. (2012), recommended a 6 % cement dose as a practical and cost-effective method for stabilizing fine soil. (D. Wang & Korkiala-Tanttu, 2020), have suggested the suitable option for stabilizing clay in

Sweden and Finland as Nordkalk Terra^{TM} KC50, which is a mixture of (50% cement and 50% lime) that is both reasonably priced and very efficient. In soft and sensitive clay, it is especially preferred for enhancing stiffness properties.

2.3.1 Factors that affect strength and stiffness of cemented soil

Like natural clays, stabilized clays also exhibit stiffness degradation influenced by factors like cement type, mix ratio, curing time & temperature, and loading conditions (Subramaniam & Banerjee, 2014). Curing time (days) affects both the strength (c_u) and stiffness (E_{50}) of lime-cement-treated clays. Longer curing durations lead to increased (c_u) and a similar trend existed for (E_{50}) as shown in Figure 2.3 (Paniagua et al., 2022). Wong et al. (2023) described the observed fluctuations in the properties of lime-cement columns as being due to differences in the number of mixing blades, the speed of extraction, and the speed of rotation during the in-situ installation of lime cement columns.

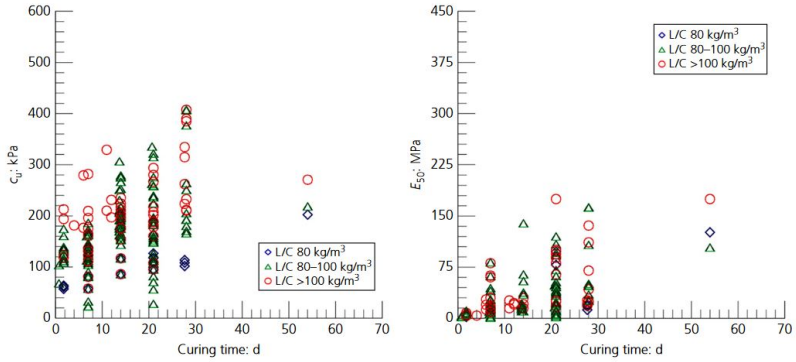

Figure 2.3: *Shear strength, (c_u) and secant stiffness, (E_{50}) variation with curing time, (d) for stabilized clay, adapted from, Paniagua et al. (2022)*

The Figure 2.4, illustrates the impact of cement type and water content on the strength of stabilized clay. The data indicates that Portland cement demonstrates superior strength and maximum shear modulus (G_{max}) compared to gypsum across a spectrum of clay samples (Yang & Woods, 2015).

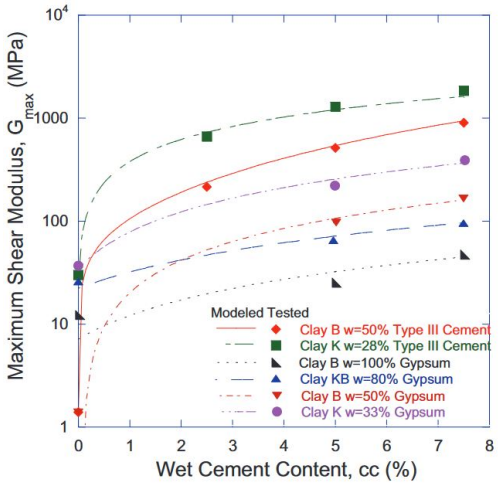

Figure 2.4: *Variation of treated clay strength with increase in cement content, cc $(\%)$, adapted from, Yang and Woods (2015)*

2.4 Stress, Strain, Invariants and Tensors

The lab work at the Chalmers geotechnics lab involved the conduction of undrained cyclic triaxial tests, where:

$$p' = \frac{1}{3}(\sigma'_a + 2\sigma'_r) \tag{2.3}$$

$$q = \sigma'_a - \sigma'_r \tag{2.4}$$

$\sigma'_2 = \sigma'_3$ for triaxial test condition

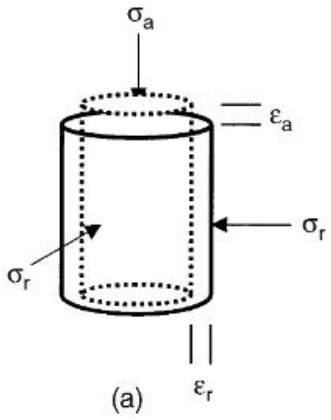

Figure 2.5: *(a) Cylindrical sample with axial and radial compressive stresses (σ_a, σ_r) and strains ($\varepsilon_a, \varepsilon_r$), adapted from, Atkinson (2000)*

.

In Figure 2.5a, the perfect cylindrical sample exhibits effective axial (σ'_a) and radial compressive stresses (σ'_r), as well as corresponding strains (ϵ_a, ϵ_r). The specimen's state is characterized by p' (effective mean pressure), q (deviatoric stress, where $q = \sigma'_1 - \sigma'_3$), and e (void ratio). In soil mechanics, compressive stresses and strains are conventionally considered positive, and all stresses are presumed effective unless otherwise specified (Prevost & Hoeg, 1975)

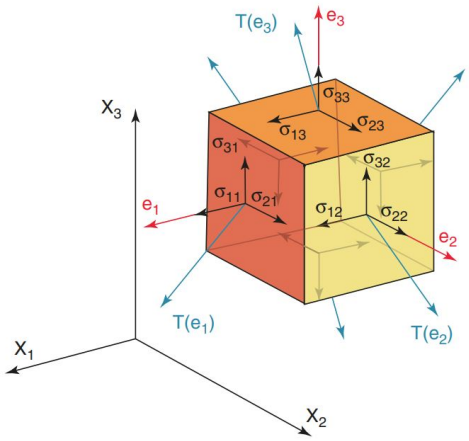

Figure 2.6: *Components of the stress tensor in cartesian coordinates, adapted from, (Massobrio & Mora, 2021)*

.

Stress invariants p' and q are expressed as:

$$p' = \frac{1}{3}(\sigma_{ii}) = \frac{1}{3}(\sigma'_1 + \sigma'_2 + \sigma'_3) \tag{2.5}$$

$$q = \left(\frac{3}{2}s_{ij}s_{ij}\right)^{\frac{1}{2}} = \frac{1}{\sqrt{2}}\left[(\sigma'_1 - \sigma'_2)^2 + (\sigma'_2 - \sigma'_3)^2 + (\sigma'_3 - \sigma'_1)^2\right]^{\frac{1}{2}} \tag{2.6}$$

where $s_{ij} = \sigma_{ij} - \frac{1}{3}(\sigma_{kk})\delta_{ij}$

are the components of the deviatoric stress tensor; σ_i = principal stress in the ith direction. Similarly, for corresponding stress invariants, p, and q, the incremental plastic strain invariants are defined as:

$$d\epsilon_v^p = d\varepsilon_{ii}^p \tag{2.7}$$

$$d\bar{\varepsilon}^p = \left(\frac{2}{3}de_{ij}^p de_{ij}^p\right)^{\frac{1}{2}} \tag{2.8}$$

where $de_{ij}^p = d\varepsilon_{ij}^p - \frac{1}{3}(d\varepsilon_{kk}^p)\delta_{ij}$
are the components of the deviatoric strain tensor; and a superscript, p = a plastic parameter. The total plastic strains are defined as;

$$\varepsilon_v^p = \int d\varepsilon_v^p = \frac{\Delta e^p}{1 + e_0} \tag{2.9}$$

$$\overline{\varepsilon}^p = \int d\overline{\varepsilon}^p \tag{2.10}$$

in which e_o = void ratio at the start of loading; Δe^p = the plastic component of void ratio change due to the loading; the integrations are carried out over the strain path; and ε_v^p and $\overline{\varepsilon}^p$ provide measures of the plastic volumetric strains and plastic shear distortions occurring during loading, respectively (Prevost & Hoeg, 1975).

2.5 Sources of uncertainties in geotechnical engineering

In geotechnical engineering, uncertainties arise from the heterogeneity found within soils (Staubach et al., 2022; Zuada Coelho et al., 2021). Tang et al. (1976), categorizes the origins of uncertainty into three primary groups: 1) inherent variations; 2) inaccuracies in measurements; and 3) uncertainty in transformations (models). Soil properties fluctuate due to a combination of geological events, environmental influences, and human activities, which occur over various spatial and temporal extents. Differences between hydro-mechanical characteristics measured in lab environments and those seen in real-world situations are the source of measurement errors. These mistakes can be caused by a number of things, including equipment limitations, test procedures, and sample disruptions (Tahershamsi, 2023). The observational method is valuable because it allows engineers to adapt to unexpected uncertainties from ground conditions encountered during construction, rather than rigidly adhering to a pre-determined plan (Peck, 1969).

In this thesis project, the uncertainties arising from laboratory measurements are very crucial and will be discussed in the methodology chapter 3.

2.6 Cyclic behavior and degradation of natural clays

2.6.1 Undrained cyclic loading

Numerous academic papers extensively examined how natural clays degrade under cyclic loading (Andersen et al., 1980; Idriss et al., 1978; Matasovic & Vucetic, 1992). Figure 2.7 shows, cyclic loading with three loading components as in-situ deviatoric stress (q_o), pre-shearing amplitude (q_p), and cyclic loading amplitude (q_{cyc}). Due to poor pore water drainage, rapid loading on saturated seabed soils causes undrained behavior (Bear & Verruijt, 2012). Pre-shearing means here applying an initial shear stress or strain to the soil sample before commencing the cyclic loading phase.

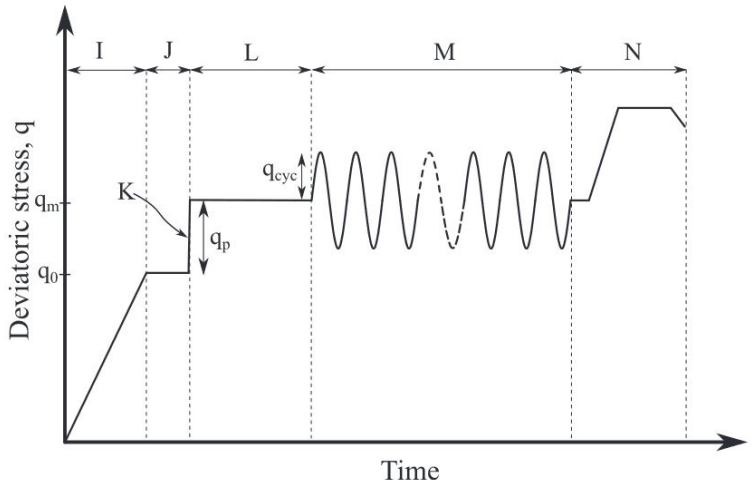

Definition of stages: I – anisotropic consolidation; J – saturation; K– pre–shearing; L – creep; M – cyclic loading; N – post-cyclic monotonic shearing.

Figure 2.7: *Illustration of cyclic load under undrained test, adapted from, Tahershamsi et al. (2023)*

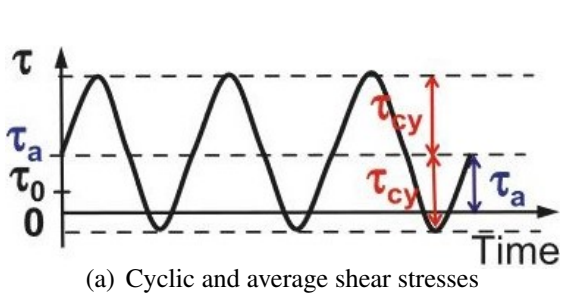

(a) Cyclic and average shear stresses

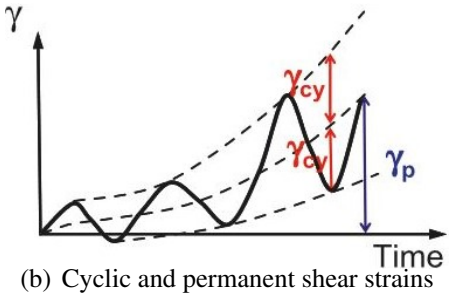

(b) Cyclic and permanent shear strains

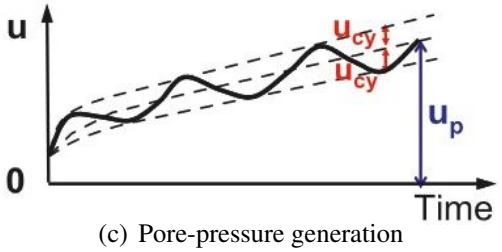

(c) Pore-pressure generation

Figure 2.8: *Temporal Evolution of Pore Pressure (u) and Shear Strain (γ) during undrained cyclic loading, adapted from, Andersen (2009)*

The Figure 2.8b,c illustrates the changes in pore pressure (u) and shear strain (γ) in a soil element subjected to repeated loading under constant cyclic shear stress (τ_{cy}) and constant shear stress (τ_a). Pore pressure is created by the combination of a permanent component (u_p) and a cyclic component (u_{cy}) due to cyclic loading. The increase in pore pressure reduces effective stresses (σ'), leading to the gradual accumulation of cyclic (γ_{cy}) and permanent (γ_p) shear strains.

Higher stress levels expedite pore pressure build-up, resulting in quicker material failure due to increased cyclic shear stresses and earlier surpassing of the failure threshold. This phenomenon is known as cyclic stiffness degradation (Andersen, 2009; Lee & Sheu, 2007). Refer to Figure 2.9 for pore pressure build-up under confining stresses of 100 kPa and 200 kPa. Here, it can be noticed that the cyclic stress ratio (CSR) also plays a significant role in stiffness degradation.

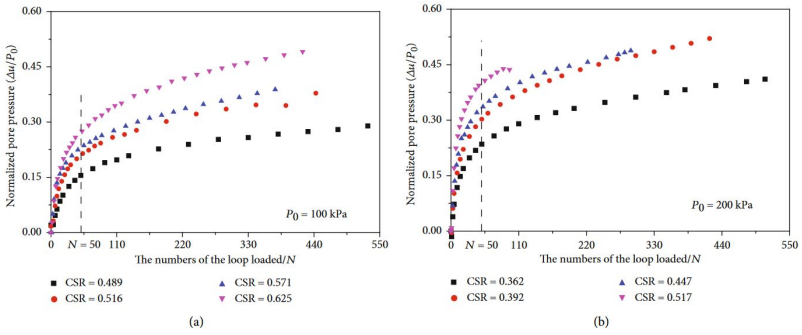

Figure 2.9: *Pore pressure accumulation at different CSRs in natural soft clay (a) Confining stress 100 kPa, (b) Confining stress 200 kPa, adapted from, Zhu et al. (2021)*

The Figure 2.10b visually represents how soil responds to repeated undrained cyclic loading under constant shear stress. Andersen (2009), in his research study, noticed that the center point of the cycle moves along with increasing shear strain from the left (1st cycle) to the right (Nth cycle). He also explained the difference between cyclic and monotonic testing. The soil undergoes compression in monotonic testing until reaching failure at the black failure envelope. Conversely, in cyclic tests, the effective stress diminishes due to the fluctuating tension induced by cyclic shear stress (τ_{cy}). Upon reaching collapse at cycle N under cyclic loading, as opposed to monotonic loading, the same soil may experience failure at a lower shear stress as shown in the Figure 2.10a.

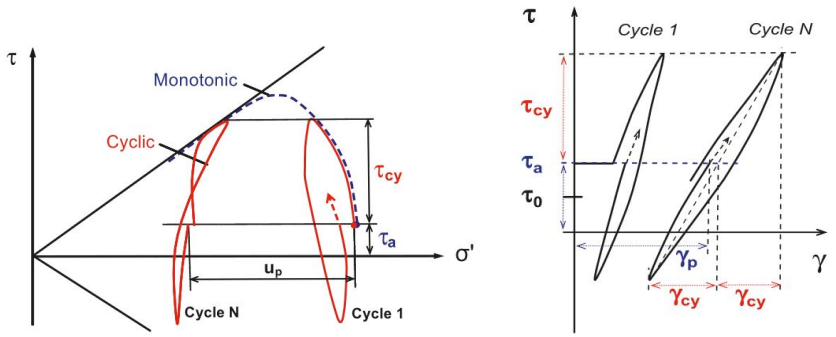

(a) Cyclic loading and monotonic loading (b) Undrained cyclic loading

Figure 2.10: *Effective stress reduction due to cyclic loading and monotonic loading, adapted from, Andersen (2009)*

2.6.2 Cyclic response

In a study by (Zhu et al., 2021), biaxial cycling curves obtained from cyclic triaxial tests were examined. The research found that during the unloading phase, strain splits into recoverable rebound strain ($\epsilon_{a,r}$) and non-recoverable accumulated plastic strain ($\epsilon_{a,p}$) components, as illustrated in Figure 2.11. The total strain for both components was calculated as ($\epsilon_{a,t} = \epsilon_{a,r} + \epsilon_{a,p}$).

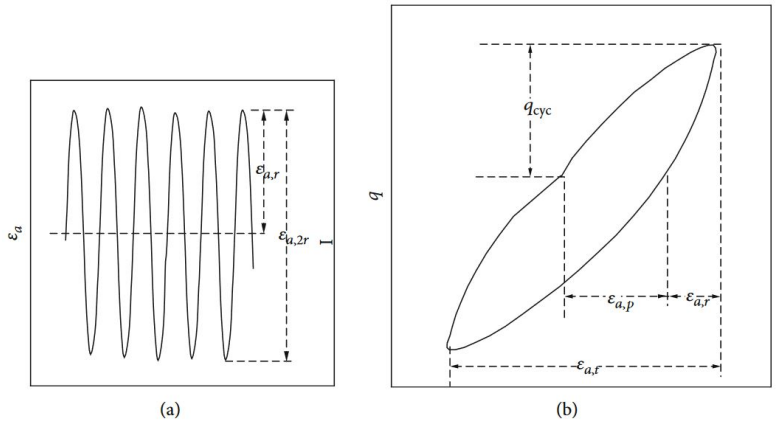

Figure 2.11: *(a) Biaxial cyclic curves from triaxial test results, (b) A typical hysteresis loop adapted from, Zhu et al. (2021)*

Various scholarly publications revealed that clay loses strength and stiffness with each successive cycle when cyclic loading (stress and strain amplitudes) exceeds a critical threshold. Narasimha Rao and Panda (1998), in their article, explained the reduction of post-cyclic strength of soft marine clay with a downward shift in the backbone curve during strain-controlled cyclic loading test as shown in Figure 2.12.

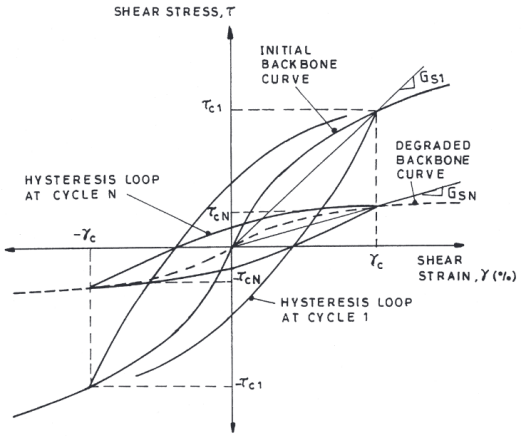

Figure 2.12: *(Stress-strain loops for the initial cycle and a subsequent cycle following a defined level of degradation, adapted from, Narasimha Rao and Panda (1998)*

Lee and Sheu (2007), present an equation for the initial backbone curve as;

$$\epsilon_c = \varepsilon_y \left(\frac{\sigma_d}{E_{\max} \varepsilon_y} \right) \left(1 + \alpha \mid \frac{\sigma_d}{E_{\max} \varepsilon_y} \mid^{r-1} \right) \tag{2.11}$$

In the equation, α and r are constants, ε_y is a reference axial strain, and ε_c and σ_d are the loop tip coordinates.

Several studies have examined the interconnected behavior of the subsurface and railway track when trains are in motion (Alves Costa et al., 2010; Hall, 2003; Tahershamsi et al., 2023). Shih et al. (2017) and Woodward et al. (2015), emphasize the importance of accurate models for non-linear soft soil behavior, particularly for the degradation of shear modulus (G) and elastic stiffness (E). Suiker and De Borst (2003), proposed a model to predict cyclic accumulation in granular materials under significant cyclic loading. When strain levels exceed 10^{-2}, soil properties change significantly with shear strain and cycle progression (Hall, 2000).

2.6.3 Cyclic response of cemented soils

Although repeated loading cycles can produce bond breakage and a noticeable drop in stiffness, adding cement greatly increases the soil's shear stiffness. Yu and Liu (2020), both researchers conducted a comparative analysis of the cyclic response exhibited by cement-mixed soils (CMS) and remolded mixed soils (RMS) during undrained cyclic triaxial testing at a confining pressure of 100 kPa. Their findings suggest that introducing a 50 % cement fine content (FC) led to notable improvements in stiffness properties, characterized by reduced pore pressure development and axial strain, as evidenced by the data represented by the black plotting lines in Figure 2.13. The observed difference in behavior was less pronounced during the initial cycles but exhibited a gradual and notable escalation with progressive cycles.

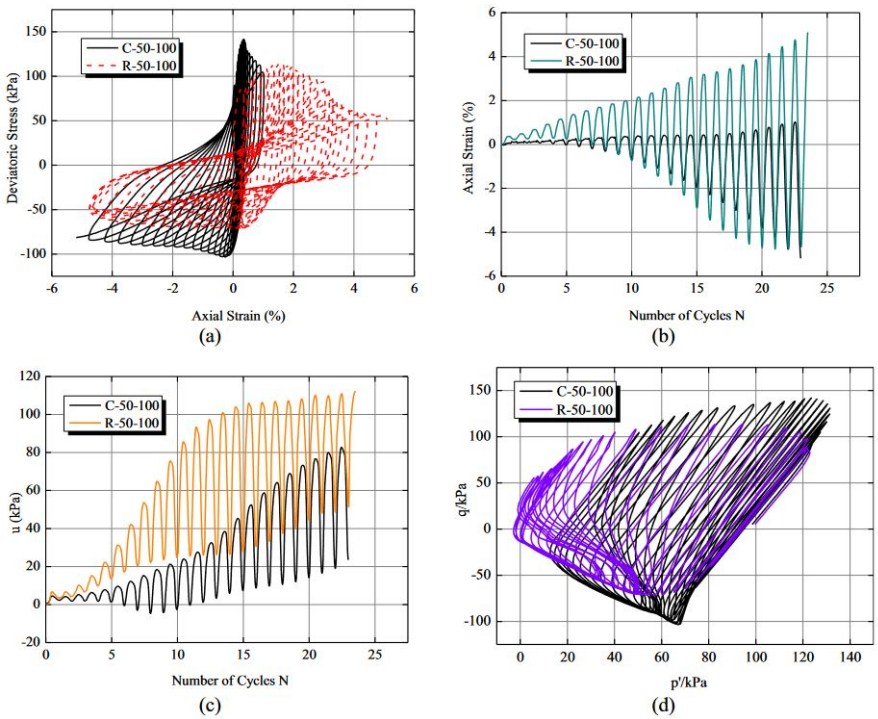

Figure 2.13: *Undrained cyclic triaxial response comparison: RMS vs. CMS, FC=50%, σ_3 = 100 kPa* a) Deviatoric stress, b) Axial strain, c) Porepressure, d) Effective stress path, adapted from, Yu and Liu (2020)

According to research by Sharma and Fahey (2003), undrained cyclic triaxial tests were performed on cement-treated and untreated samples that were isotropically consolidated at a pressure of 200 kPa as shown in Figure 2.14. The secant shear modulus (G_{sec}) and the ratio of secant shear modulus to initial shear modulus (G_{sec}/G_o) exhibited similar stiffness degradation trends with respect to deviatoric strain (ϵ_s). It is worth noting that the cemented soil displayed significantly higher initial stiffness (G_o) compared to the untreated soil. A significant degradation trend can be observed between the strain range of 10^{-2} and 10^{0} %. This trend aligns with the stiffness degradation curve explained in Figure 2.22.

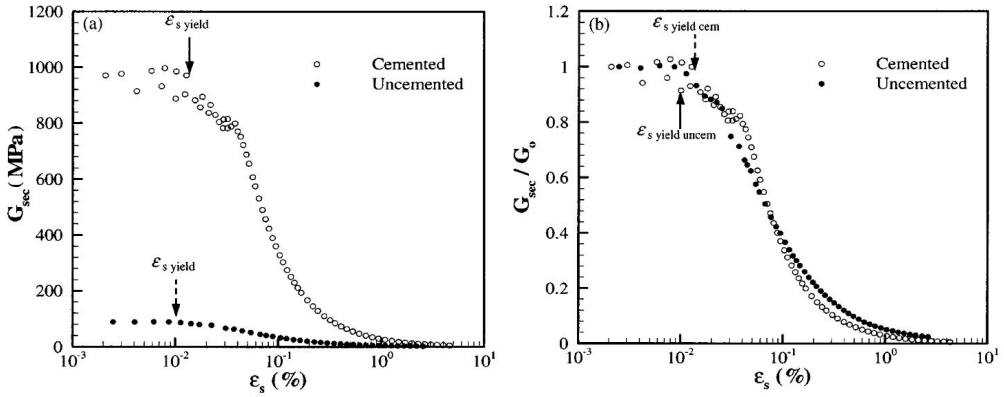

Figure 2.14: *Comparison of stiffness degradation G_{sec} and normalized stiffness degradation G_{sec}/G_o, both for cement treated and uncemented samples at confining pressure $Po' = 200$ kPa, adapted from Sharma and Fahey (2003)*

Bozkurt et al. (2023) cited, the amount of excess porewater pressure that builds up inside stabilized clay during undrained triaxial tests depends on several factors, including the type of minerals the clay contains, the amount of pressure it was under before the test, and the external force applied during the test.

On the other side, as dynamic strain increases, the damping ratio also rises. Under shear stress, soil samples loosen up and need more energy and rubbing, which causes the damping ratio to increase with dynamic strain (M. Wang et al., 2012). The figure 2.15 shows the trend between damping ratio (λ), and dynamic strain (ε_d).

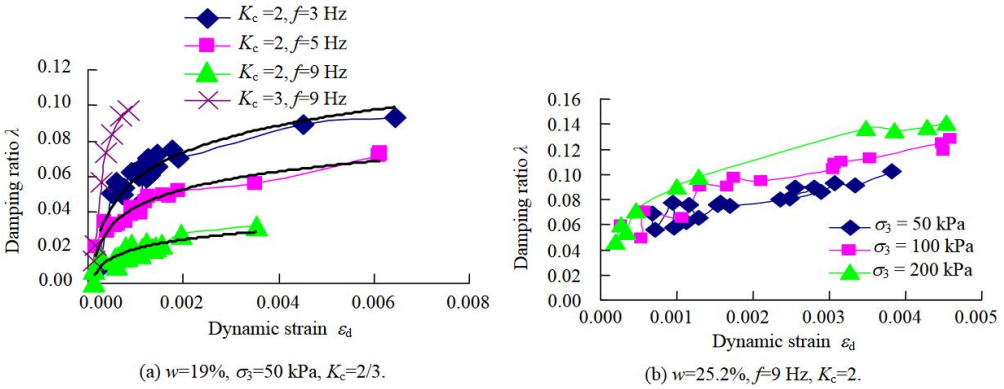

Figure 2.15: *Dynamic damping ratio (λ) Versus strain ϵ_d curves for lime treated expansive soil, adapted from M. Wang et al. (2012)*

2.7 Factors that affect dynamic stiffness properties

Evaluating the dynamic characteristics of clays is essential to understand how they react to dynamic cyclic loading precisely.

2.7.1 Cyclic stress ratio, CSR

Cyclic loading induces peak strain (ε_{peak}), comprising recoverable resilient strain (ε_r) and permanent strain (ε_p). The magnitude of (ε_r) is influenced by CSR as shown in the previous Figure 2.9. Figure 2.16 illustrates the loading sequence for two distinct sets of multi-stage tests with varying strain levels.

Researchers, Okur and Ansal (2007), conducted cyclic loading tests on a material in two stages to evaluate its behavior at different strain levels. The first approach, used when samples were limited, involved gradually increasing cyclic stress amplitudes in a single test to cover a wide strain range. The second approach involved pre-straining the material at a higher level before applying smaller cyclic strains. Using varying amplitudes, this method aimed to minimize pre-straining effects and provide a clearer understanding of the material's properties across different strain levels.

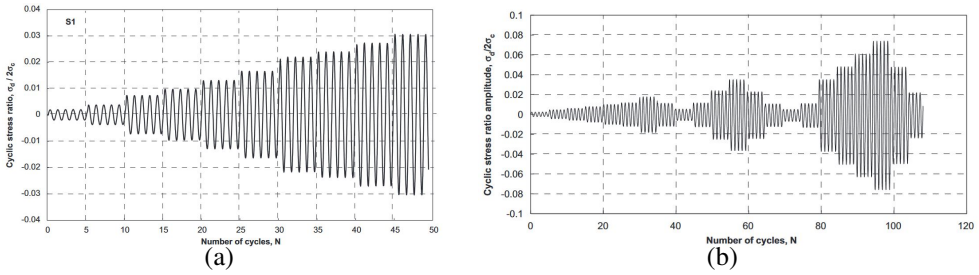

(a) (b)

Figure 2.16: *Trends between $CSRs$ and number of cycles (N) for 2 different groups of multi-stage tests, adapted from, Okur and Ansal (2007)*

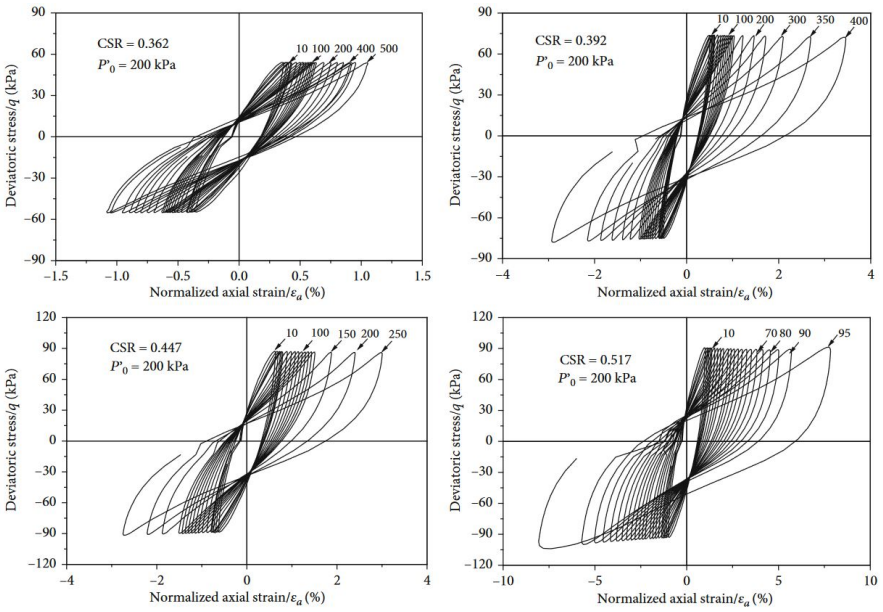

Figure 2.17: *(Stress-strain hysteretic loops for different CSRs for fixed stress value (200 kPa), adapted from, Zhu et al. (2021)*

In his research, J. Wang et al. (2013) demonstrated that lower CSR (cyclic stress ratio) results in a stable, resilient strain (ε_r) at low cycle numbers, such as 1000 cycles. On the other hand, higher CSR values lead to a continuous increase in resilient strain (ε_r) even beyond 50,000 cycles. The permanent strain (ε_p) shows non-linear growth with CSR. The strain increases gradually below a CSR of 0.3, but it accelerates exponentially above this value. The behavior of axial strains under increasing CSR values for a fixed-stress mode (200 kPa) can be observed in Figure 2.17. Cyclic loading promotes pore pressure accumulation, which weakens the material's structure, reducing its stiffness and strength. This deterioration significantly affects resilient and permanent strains.

According to (Lei et al., 2017), the CSR, is determined by dividing the cyclic loading amplitude (q_{cyc}) by twice the peak deviatoric stress (q_f) from monotonic tests. This approach facilitates the classification of cyclic stress levels applied to the specimens.

$$CSR = \frac{q_{\text{cyc}}}{2q_f} \tag{2.12}$$

2.7.2 Secant Young's modulus, E

According to a research article by (Kokusho, 1980), When a material is subjected to equal stress in all directions (triaxial stress), two crucial measures can be determined: the extent to which the material deforms (Secant Young's modulus, E) and its resistance to shearing (secant Shear modulus, G).

$$E = \frac{\Delta\sigma}{\Delta\varepsilon} \tag{2.13}$$

$$G = \frac{\Delta\tau}{\Delta\gamma} \tag{2.14}$$

$$\Delta\tau = \frac{\Delta\sigma}{2} \tag{2.15}$$

$$\Delta\gamma = (1+\nu).\Delta\varepsilon \tag{2.16}$$

The parameters denote various amplitudes in a material: axial stress ($\Delta\sigma$), axial strain ($\Delta\varepsilon$), shear stress ($\Delta\tau$), and shear strain ($\Delta\gamma$). Under radial stress, these four quantities correlate. Poisson's ratio (ν) is roughly 0.5 in fully saturated, undrained conditions, which calculates shear strain ($\Delta\gamma$) and shear modulus (G). Drained tests yield only axial strain ($\Delta\varepsilon$) and axial modulus (E).

The figure 2.18 shows a single cycle's ideal stress-strain hysteresis loop. In a standard triaxial test, the ACBDA loop, with its key points A, B, and E_{max}, provides essential data on the peak cyclic axial strain (ϵ_c) and deviatoric stress (σ_d). These points are not just theoretical markers but have practical implications in the engineering work. The secant Young's modulus (E) is calculated from the slope of the line connecting these extreme points (A, B) of the hysteresis loop, which reflects stiffness. The initial steepest slope of the backbone curve starting from the origin indicates the maximum Young's modulus (E_{max}) (Lee & Sheu, 2007).

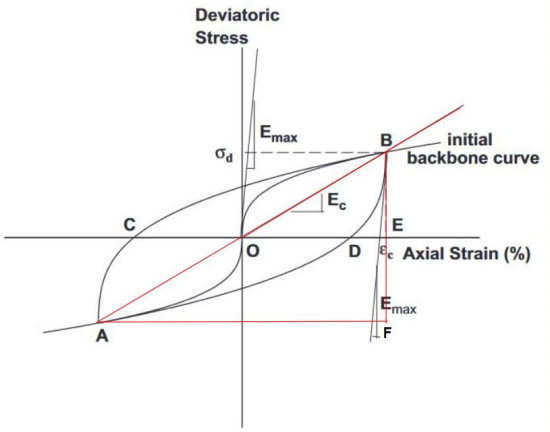

Figure 2.18: *A stress-strain loop, representing an idealized scenario, illustrates the response of a sample under symmetric cyclic loading adapted from, Lee and Sheu (2007)*

The equivalent damping ratio (D) in Figure 2.18 is defined by Kokusho (1980), using the loop area (ΔA) in relation to a triangle area (A).

$$\Delta A = Loop\ A - C - B - D - A$$
$$A = A - B - F$$

$$D = \frac{\Delta A}{\pi A} \tag{2.17}$$

Adopting the assumptions made by Lee and Sheu, If the soil behaves both elastically and isotropically, the values of G, G_{max}, and γ can be determined using the following two equations:

$$G = \frac{E}{2(1+\nu)} \tag{2.18}$$

$$\gamma = \epsilon(1+\nu) \tag{2.19}$$

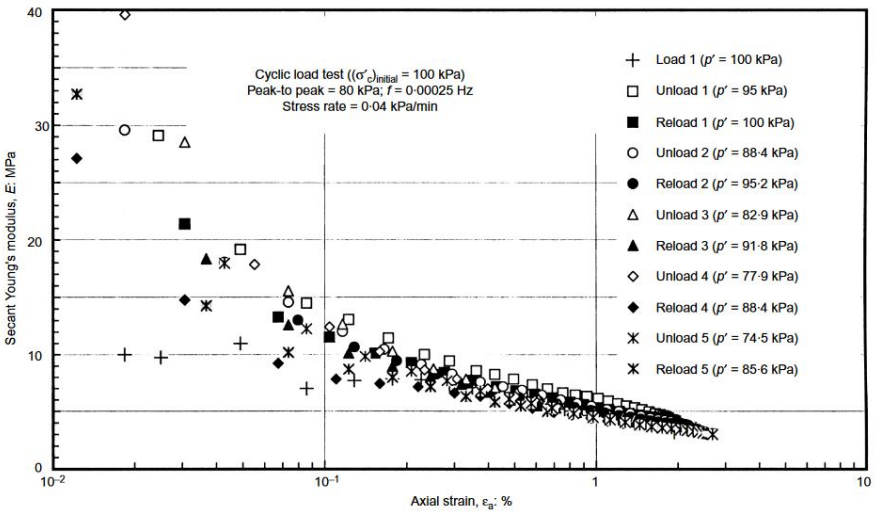

Figure 2.19: *Secant stiffness degradation (E_{sec}) during unload and reload cycles for soft natural clay, adapted from, Teachavorasinskun et al. (2002)*

The calculations involve the utilization of the secant shear modulus (G), secant Young's modulus (E), axial strain (ε), shear strain (γ), and Poisson's ratio (ν = 0.20 for undrained Gothenburg clay). The accuracy of (G) is heavily reliant on the precision of (E). Inaccurate computation of (E) will consequently impact the remaining stiffness parameters.

The plot in Figure 2.19 illustrates the progressive decline in secant stiffness (E_{sec}), starting from 40 MPa, for a soft natural clay sample subjected to specified cyclic testing.

2.7.3 Shear modulus, G_{max} and Damping ratio, D

Estimating shear modulus (G) and equivalent damping ratio (D) is crucial in assessing soil response to dynamic loads (Abdellaziz et al., 2021). To understand soil-structure interactions, it is essential to accurately determine the soil's stiffness. The initial shear modulus (G) has become critical in numerous engineering applications. It is a fundamental parameter for standard designs and advanced simulations, enabling the study and prediction of structural behavior under different cyclic loading conditions (Sharma & Fahey, 2003).

Shear modulus (G_{max}) which is an elastic property of soil with relation to shear wave velocity, is given as:

$$G_{max} = \rho_T . V_s^2 \tag{2.20}$$

where, G_{max} shows maximum shear modulus, ρ_T shows clay sample mass density, and V_s^2 shows shear wave velocity at small strains. Figure 2.20 shows the trend between secant shear modulus (G) and normalized shear modulus (G/G_{max}) with shear strain (γ) for natural clays originating from diverse global regions. The below Table 2.1 shows the factors that affect the ($G/G_{\max}$).

Increasing Factor	$G/G_{\max}$
Confining pressure, σ'_m	Increases with σ'_m; effect decreases with increasing Pl
Void ratio, e	Increases with e
Geologic age, t_g	May increase with t_g
Cementation, c	May increase with c
Overconsolidation ratio, OCR	Not affected
Plasticity index, PI	Increases with PI
Cyclic strain, γ_c	Decreases with γ_c
Strain rate, $\dot{\gamma}$	G increases with $\dot{\gamma}$ but $G/G_{\max}$ probably not affected if G and $G_{\max}$ are measured at same γ
Number of loading cycles, N	Decreases after N cycles of large γ_c (G_{max} measured before N cycles) for clays; for sands, can increase (under drained conditions) or decrease (under undrained conditions)

Table 2.1: Factors that affect (G/G_{max}) redeveloped from (Vucetic & Dobry, 1991)

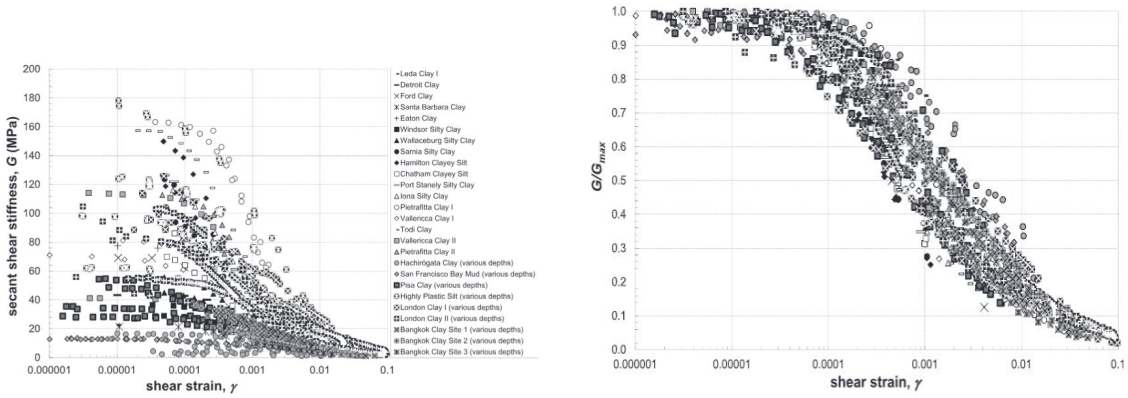

(a) (b)

Figure 2.20: *Trend between secant shear modulus, and normalized modulus with shear strain for natural clay from different regions, adapted from, Vardanega and Bolton (2013)*

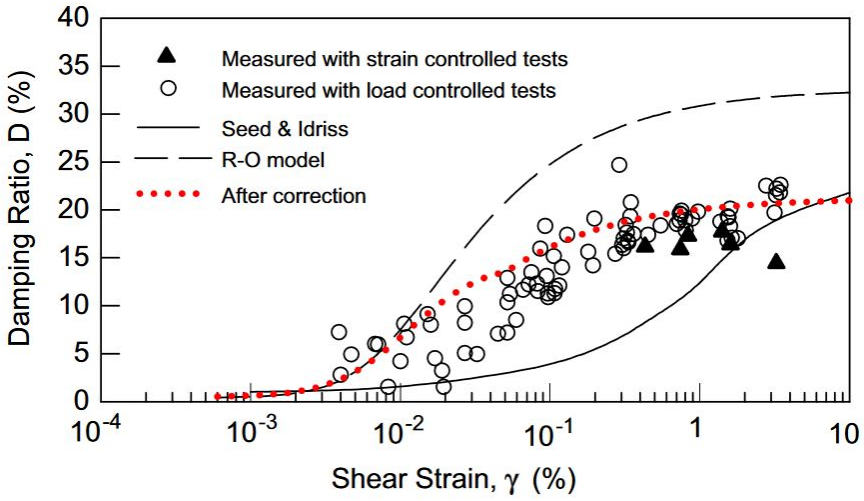

Figure 2.21: *Trend between damping ratio (D), and shear strain amplitude (γ) for the first cycle for soft clay, adapted from, Lee and Sheu (2007)*

Under cyclic loading, clay shows notable hysteretic and nonlinear behavior. There is a reduction in shear modulus curve (G/G_{max}) and an increase in the damping curve (h) as strain amplitude (γ) increases, as shown in Figure 2.21. This is because the clay structure is damaged and loses its stiffness with increasing shear stains. This behavior highlights the dynamic complexity of clay under cyclic loading conditions (Lee & Sheu, 2007). Refer to Table 2.2 for factors affecting damping ratio.

2.7.4 Modulus reduction curve, G/G_{max} (v/s) γ_c

The normalized stiffness degradation curve is shown in Figure 2.22. Despite a great deal of research work on the characteristics of soft clay under cyclic loading, the evolution of (G_{max}), small-strain shear modulus, and deformation behavior under cyclic loading are still uncertain (Zhu et al., 2021).

Increasing Factor	Damping ratio, ξ
Confining pressure, σ'_m	Decreases with σ'_m; effect decreases with increasing PI
Void ratio, c	Decreases with e
Geologic age, t_g	Decreases with t_g
Cementation, c	May decrease with c
Overconsolidarion ratio, OCR	Not affected
Plasticity index, PI	Decreases with PI
Cyclic strain, γ_c	Increases with γ_c
Strain rate, $\dot{\gamma}$	Stays constant or may increase with $\dot{\gamma}$
Number of loading cycles, N	Not significant for moderate γ_c and N

Table 2.2: Factors that affect damping ratio (ξ) redeveloped from (Vucetic & Dobry, 1991)

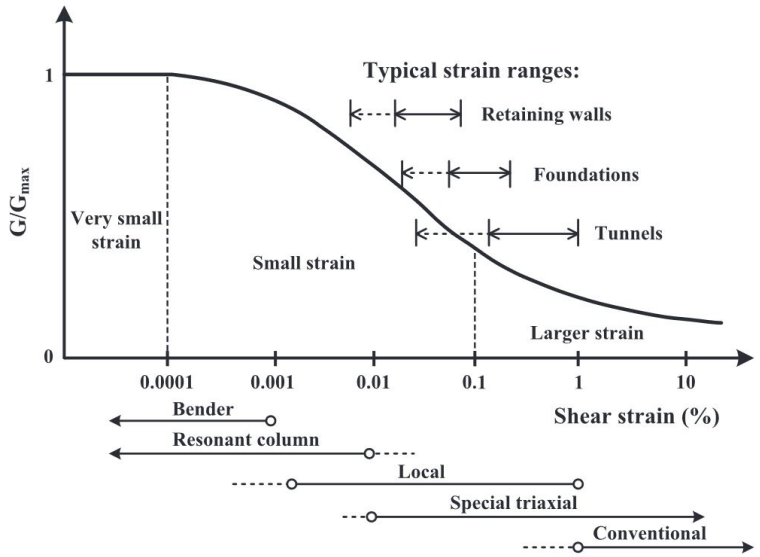

Figure 2.22: *Normalized stiffness degradation curve between (G/G_{max}) and (γ), adapted from, Likitlersuang et al. (2013)*

The stiffness degradation curve is characterized by three distinct segments based on strain ranges. The initial segment, termed "very small strain," encompasses strain values less than 0.0001 %. Following this, the "small strain" range spans from 0.0001 % to 0.1 %, while the "large strain" category encompasses values exceeding 0.1 %. The accompanying figure illustrates the typical strain ranges applicable to geotechnical structures.

2.7.5 Degradation index, δ_n

Figure 2.23 displays the cyclic loops observed during the first and last cycles of the cyclic triaxial test, where a constant cyclic stress amplitude was applied. The figure shows various parameters: N represents the cycle number, ($q = \sigma_1 - \sigma_3$) signifies the deviator stress. $\varepsilon_{aN,max}$ and $\varepsilon_{aN,min}$denote the maximum and minimum axial strains at cycle N, respectively, and G_N denotes the secant shear modulus at cycle N.

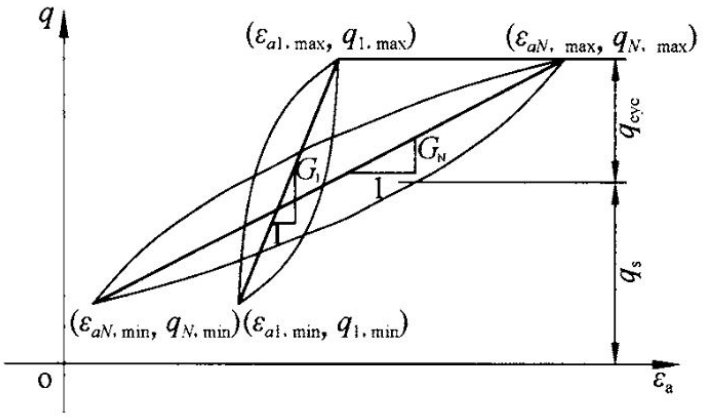

Figure 2.23: *Illustration of degradation index adapted from, Cai and Wang (2008)*

.

(Idriss et al., 1978) first proposed the degradation index to measure soil degradation, which has since been refined as:

$$\delta = \frac{G_N}{G_1} = \frac{2q_{\text{cyc}}/(\varepsilon_{aN,\max} - \varepsilon_{aN,\min})}{2q_{\text{cyc}}/(\varepsilon_{a1,\max} - \varepsilon_{a1,\min})} = \frac{(\varepsilon_{a1,\max} - \varepsilon_{a1,\min})}{(\varepsilon_{aN,\max} - \varepsilon_{aN,\min})} \tag{2.21}$$

The plots in Figure 2.24 illustrate the correlation between the degradation index (δ) and (N) across various cyclic stress ratios. Observing the trend, it's evident that the degradation index (δ) declines as the number of cycles increases (Cai & Wang, 2008).

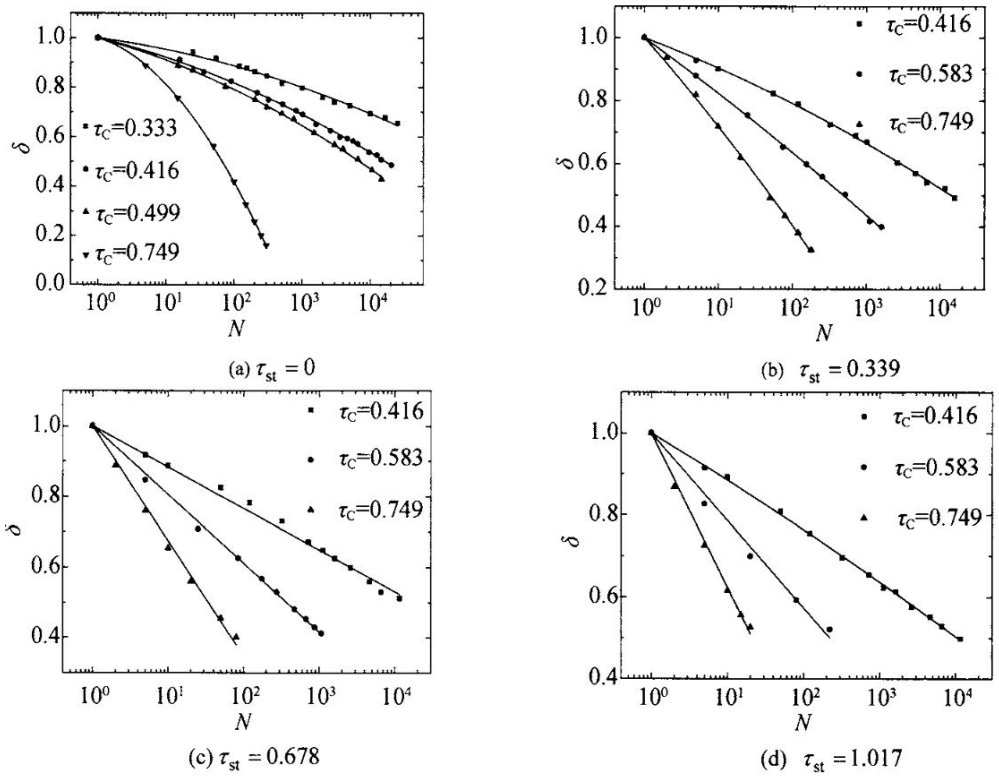

Figure 2.24: *Decline in degradation index (δ) with increasing number of loops (N) adapted from, Cai and Wang (2008)*

3 Methodology

This chapter provides a short description of the sample collection sites. Additionally, it outlines the laboratory triaxial setup and discusses test plans for LCC and NC. Furthermore, it explains the workflow of data pre-processing utilizing Python for cyclic raw data obtained directly from GDSLab software. It also provides a detailed explanation of each pre-processing step to ensure the generation of insightful outputs and plots illustrating stiffness degradation, thereby facilitating a thorough comparative study of LCC and NC. While Tahershamsi et al. previously analyzed the NC samples, the data processing technique is not clear for the authors in the project and to facilitate a more rigorous and transparent comparison, this project reanalyzes the NC samples using the identical computational strategy employed for the LCC samples.

3.1 Site details

In this project study, two distinct datasets, comprising LCC, and NC, were acquired from two different sites in Sweden.

3.1.1 Centralen E02 site

The clay samples stabilized with lime cement (LCC3 - LCC17) were procured from an excavation depth ranging from 5m to 7m at the E02 Centralen site, which is near Gothenburg Central Station (Figure 3.1a). This site is important being a part of the Västlänken railway project, which aims to construct a 6 km tunnel underneath the city to enhance transportation accessibility and connectivity for local commuters (Bozkurt et al., 2023). According to (Wong et al., 2023), the 200-meters long braced excavation is shored with sheet-pile walls. At the base's passive side, lime-cement columns with a binder content of $80kgm^{-3}$ provide additional support, exceeding the $40kgm^{-3}$ content used above the excavation level as shown in Figure 3.1b.

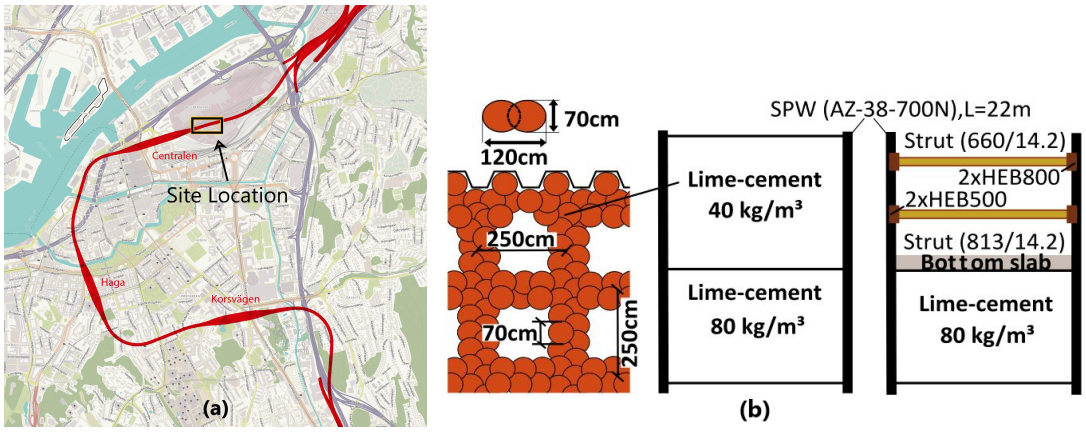

Figure 3.1: *a) E02 Centralen site, Location:*$57°42'\ 25''N, 11°57'59''E$ (Website link) , b) Cross-section of deep excavation of E02 site with column layout adapted from (Bozkurt et al., 2023)

The author Bozkurt et al., described the site's stratigraphy, noting a thick layer of clay sitting over a 2 to 5-meter-deep fill. The geological formation mainly consists of deep

layers of soft, highly plastic glacial and post-glacial clay, reaching 55 to 75 meters. The water table is approximately 2 to 3 meters below the surface and varies seasonally.

Refer to Figure 3.2 for the index properties of the Centralen E02 site.

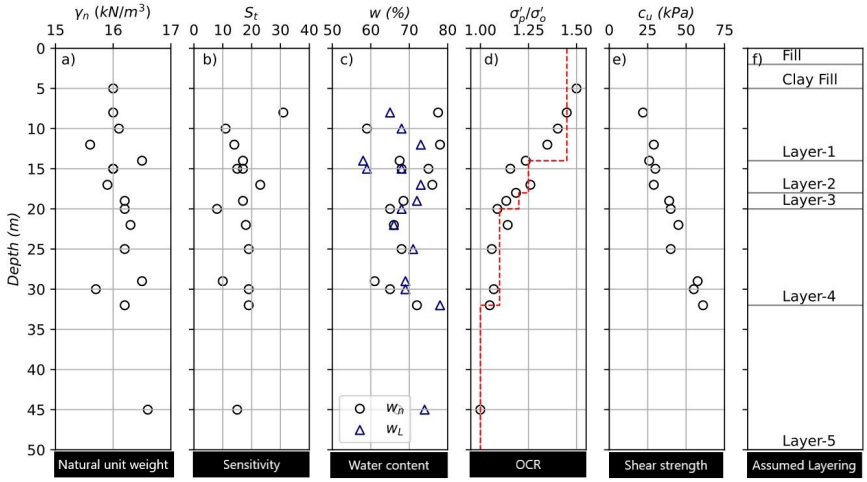

Figure 3.2: *E02 Centralen site clay index properties, adapted from, Bozkurt et al. (2023)*

3.1.2 Kärra test site

The other dataset, comprising natural clay samples (NC04-NC11), was procured from the Kärra test site in the northern region of Gothenburg, as illustrated in Figure 3.3. The sensitive clay specimens were extracted from a depth of 9 meters. According to a thesis study by Tahershamsi, the clay present at the site has been classified as highly plastic clay (CH) according to the Unified Soil Classification System (USCS). The index properties of Kärra clay are presented in the table 3.1 below.

In his 2016 study, Wood, details the composition of Kärra clay, indicating a composition of 71 % clay, with illite as the predominant mineral, 28 % silt, and the remaining 1 % comprising more significant fractions with a grain size exceeding $50\,\mu$m see Figure 3.4. The water table is near the surface, developing in-situ stress conditions with mean effective stress $p'_o = 52kPa$ and deviatoric stress $q_o = 28kPa$. Furthermore, the average shear modulus value at relative depths sharing similar geological conditions in neighboring sites is $G_{max} = 17.5 \pm 2.5$ MPa.

Table 3.1: Index properties of Kärra clay, adapted from (Tahershamsi et al., 2023)

Depth (m)	Unified symbol	ρ_b(g m^{-3})	LL (%)	PL (%)	PI (%)	w_N (%)	S_t (−)
9	CH	1.58	75.2	27.6	47.6	71.6	6.4

Properties of Kärra clay, ρ_b: bulk density; LL: Liquid Limit; PL: Plastic Limit; PI: Plastic Index; w_N: natural water content; S_t: Sensitivity

Figure 3.3: *Kärra test site with sensitive clay, Location:* $57^\circ\ 48'\ 54''$ *N,* $12^\circ\ 0'\ 31''$ *E, Elevation 2.93 m adapted from Google Earch*

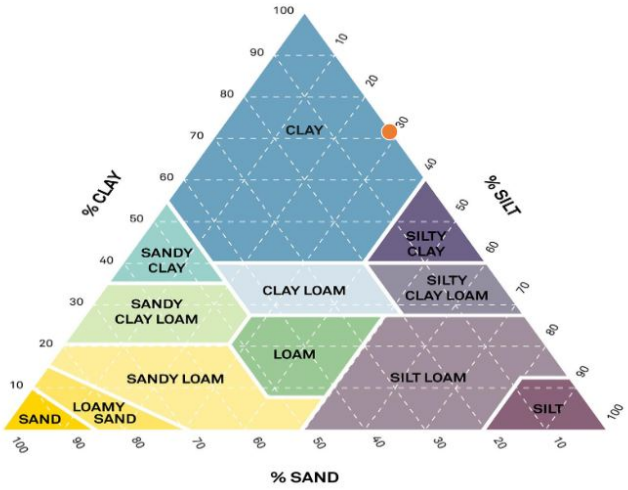

Figure 3.4: *Kärra clay composition at 9-meter depth; adapted from, Tahershamsi (2023)*

3.2 Undrained cyclic triaxial test

3.2.1 Laboratory test setup

The laboratory tests were conducted using a fully automated GDS triaxial system supported by GDSlab in the Geotechnical laboratory at Chalmers. The system's design was upgraded on a classic Bishop & Wesley (1975) type stress path triaxial cell (see Figure 3.5a), which focuses on controlling the stress conditions experienced by soil specimens. The cell can accommodate 50 mm diameter and 100 mm height cylindrical specimens.

Due to the cutting process, achieving perfectly cylindrical samples with a 50/100 mm dimension presented a difficult task, leading to observed variations in sample dimensions. As per the findings of Wong et al. (2023), the X-ray computed tomography (XCT) scan images were utilized to evaluate the diameter and height variations in the

specimens. The detailed uncertainty analysis focusing on sample diameter and height variation is presented in the methodology chapter 3. The sample dimensions are given in Table 3.2 below.

Table 3.2: Samples dimensions for LCC3, LCC17, and NC obtained from laboratory staff

Samples	Diameter, D (mm)	Height, Ho (mm)	Gauge length, Lg (mm)
LCC-03	47.32	103.36	47.37
LCC-17	47.82	100.98	48.57
NC	50	100	-

For the purpose of local strain measurements, gauge lengths were employed that were measured with increased precision using a vernier caliper.

It was essential to measure strain at a local level to accurately determine the sample's stiffness. Failing to measure strain locally could result in testing the combined stiffness of both the triaxial apparatus and the sample, leading to a potential underestimation of the sample's stiffness. To achieve this, two external Linear Variable Differential Transducers (LVDTs) were connected to the center point of the sample to monitor local axial strain. Additionally, measurements of the axial and radial strains on the test specimen were obtained using LVDT sensors installed on a lightweight aluminum holder, as shown in Figure 3.5b. These LVDT's accuracies were high but not super accurate to obtain high-quality displacement values. For a qualitative assessment of a specimen with such a high stiffness, like lime cement, localized measurements provide a clearer picture by concentrating exclusively on the clay's response to stress than global measurements. The propagation error analysis of these sensors is further explained in detail in Section 3.5.

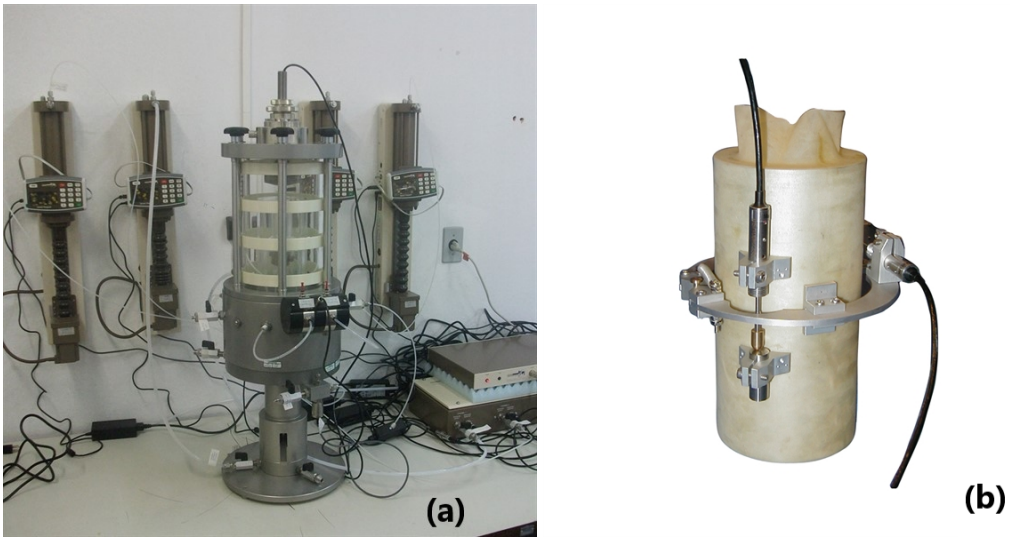

Figure 3.5: *a: Automated stress path type triaxial cell, adapted from website (Link), b: GDS LVDT local strain transducer, adapted from website (Link)*

A cyclic load (sinusoidal load) was applied at a slow pace with a period of ($T = 180s$). Precision controllers were used to manage the cell pressure, back pressure, and

ram pressure during the testing phases, which included consolidation, undrained pre-shearing, and cyclic loading. These controllers are precise, with an accuracy of more than 0.5 kPa. A typical dynamic triaxial testing system is shown in Figure 3.6.

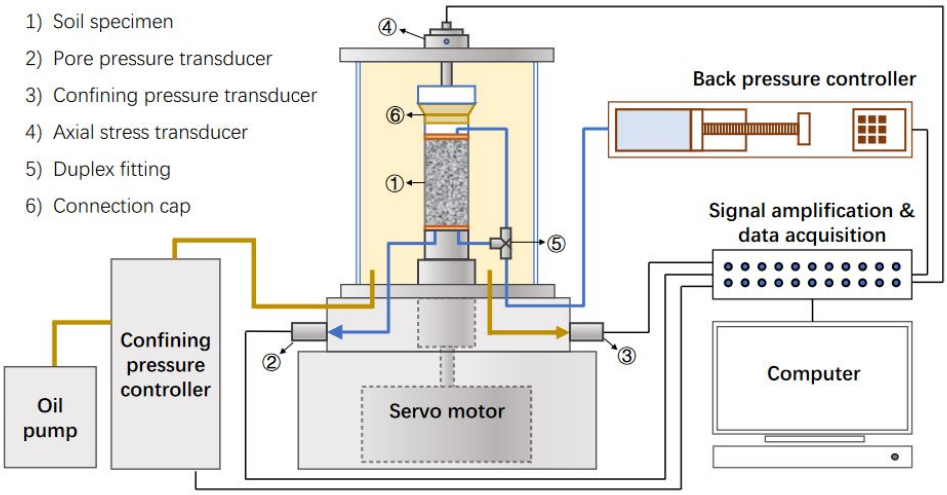

Figure 3.6: *Schematic illustration of the dynamic triaxial testing setup, adapted from, (Wu et al., 2021)*

3.2.2 Test plan for LCC samples

Two cyclic triaxial tests (LCC03, LCC17) were performed on clay with a binder concentration of 40 kg/m³ obtained from a depth range between (5 and 7 meters) at the Centralen site. The testing samples had an estimated in-situ curing period of 1 year. Lime cement-clay (LCC) was subjected to variations in cyclic stress amplitudes in the cyclic triaxial test. These amplitudes mimic the dynamic loading conditions experienced by soft clay within railway embankments. The samples were retrieved from the ground, and there was high variability (heterogeneity) throughout the soil column, causing relatively large stiffness variations within the stabilized specimen. Even though the 40 kg/m³ binder recipe was the same, but it did not mean everything was mixed with an equal percentage, which may lead to scattered test results.
Test LCC3 has been excluded from the calculations for the local strain situation. It was difficult to capture a typical cyclic pattern or fit ellipses for each cycle in this test, as shown in figure 3.7. For one load cycle in test 3, the local axial transducers recorded almost no change in displacement. This is because the sample is very stiff (LCC03 is likely more stiffer than LCC17), and the cyclic load is too small to change height significantly. Thus, it was not possible to meaningfully estimate the local stiffness from test 3 data. Although there is a change in global axial strain, but it cannot be used to accurately measure sample stiffness as it includes displacement from all components of the triaxial setup.

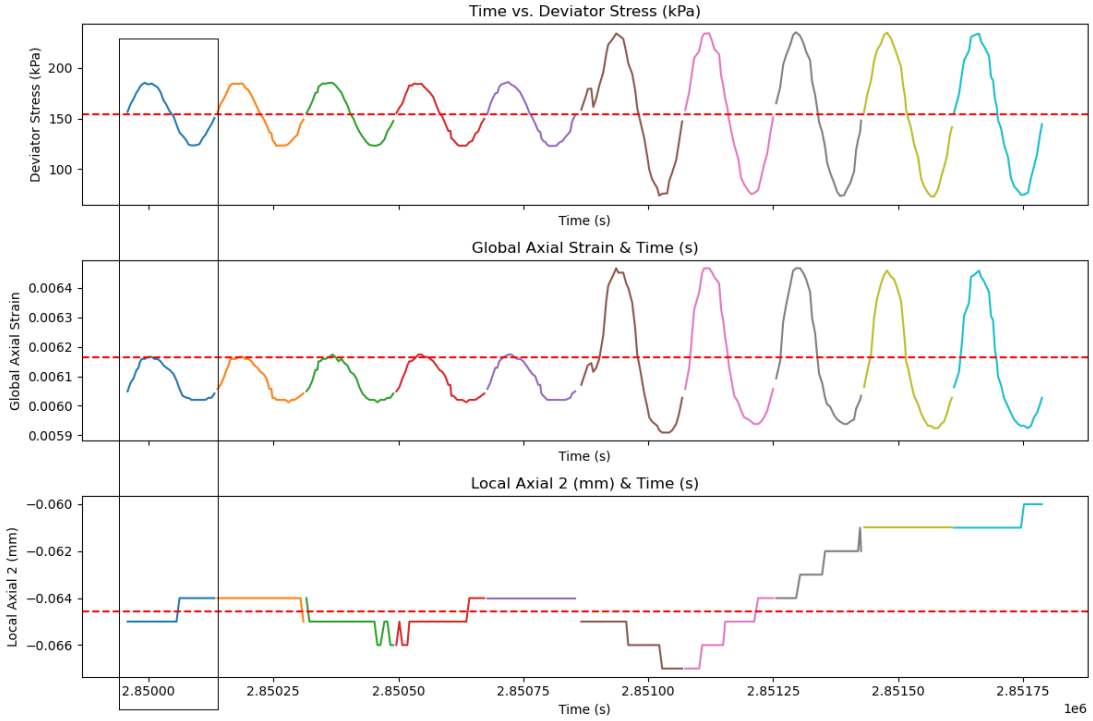

Figure 3.7: *Local and global cyclic pattern for the sample LCC03*

Please refer to the table 3.3 for information on the test plan for both LCC tests. For a comprehensive stage information of samples, kindly consult the detailed Table .1 in the Appendix - B.

Table 3.3: Characteristics of cyclic loading variables in LCC samples

Sample type	Stage Number	Loading Stages	Cyclic loading loading	Cycles nr	p0	q0	qp	qavg	qcyc	qcyc/p0	CSR	qcyc/2Su	qavg/2Su	Cyclic failure
-	-	-	(days)	-	(kPa)	(kPa)	(kPa)	(kPa)	(kPa)	-	-	-	-	-
LCC03	1	I, J, M	32,24	10420	285.2	156.9	0	154.45	31.11	0.109	0.00794	0.01589	0.080	No
LCC03	2	I, J, M	21,01	6383	285.2	156.9	0	154.129	80.3	0.28	0.02051	0.04102	0.080	No
LCC17	1	I, J, M	20,97	10064	309.8	155	0	155.60	77.41	0.25	0.01976	0.03953	0.079	No
LCC17	2	I, J, M	21,24	10196	309.8	155	0	154.72	152.57	0.493	0.03895	0.07791	0.079	No
I = anisotropic consolidation, J = saturation, K = pre–shearing, L = creep, M = cyclic loading, N = post-cyclic (Tahershamsi et.al., 2023)														

Both tests consist of two stages, with loading stages (I, J, M) taking an average of 54 days for LCC3 and 42 days for LCC17. The loading stages for LCC samples are shown in Figure .2 in Appendix - A. There was no pre-shearing stage in LCC tests and the test was stress controlled. The cyclic period was approximately ($T \approx 180s$). LCC tests used larger loading amplitudes (q_{cyc}) compared to NC. The LCC test plan is presented in a ($q_{cyc} - q_m$) plot as shown in the Figure 3.8. The tests were conducted keeping the mean deviatoric stress ($q_{mean} \approx 156kPa$) almost constant while varying the cyclic loading amplitudes ($q_{cyc} = 31kPa - 153kPa$). None of the tests failed under undrained cyclic loading conditions. The ($q_{cyc} - q_m$) plot shows that the LCC tests are in a safe zone, with a high factor of safety ($FS = 5.47 - 12.37$) range. The current distance from the maximum critical failure line (q_{max}) suggests a considerable margin of safety. The detail of ($q_{cyc} - q_m$) plot is further explained in section 3.3.

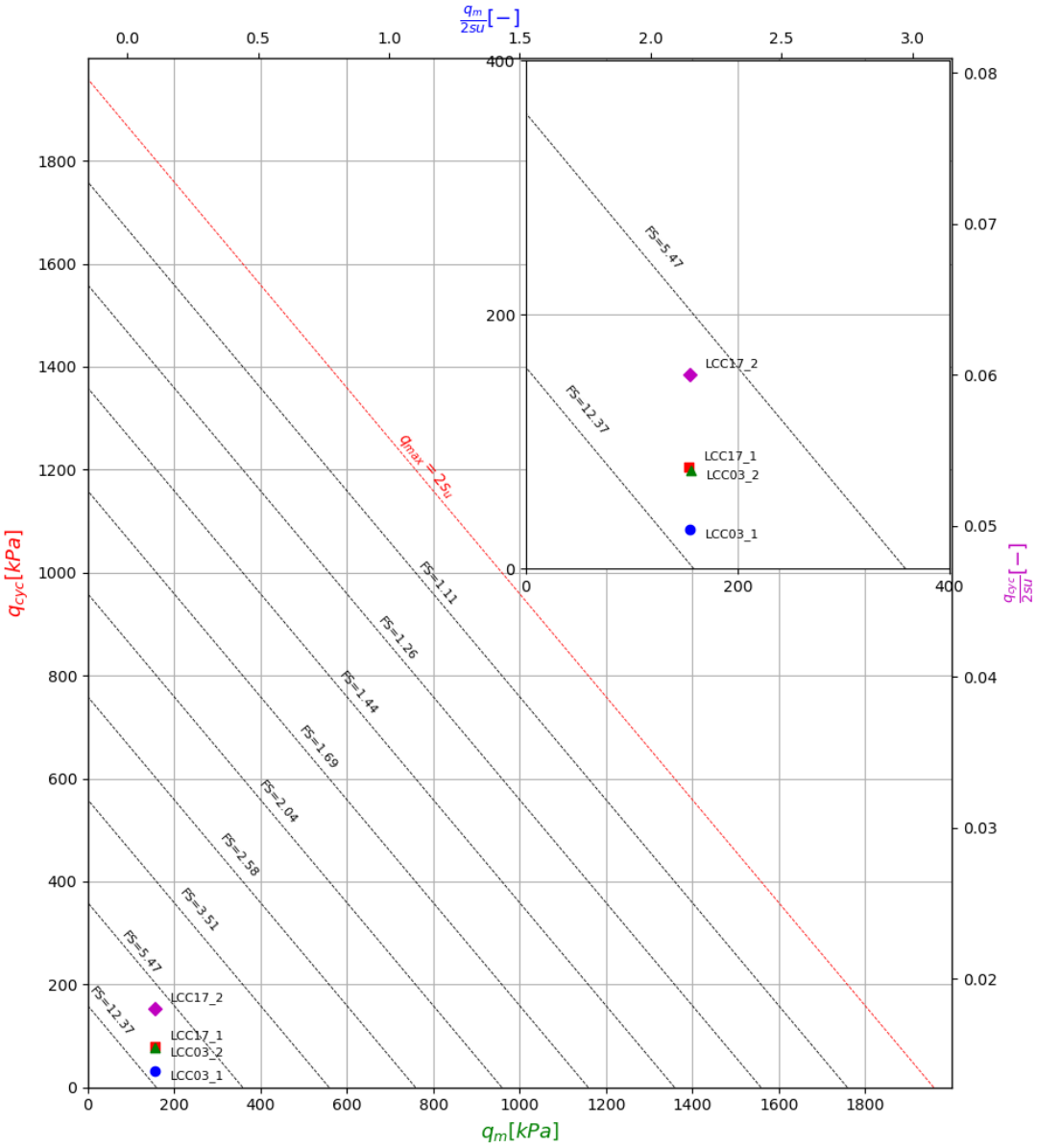

Figure 3.8: *Overview of samples tests of LCC in relation to q_m and q_{cyc}*

3.2.3 Test plan for NC samples

Eight cyclic undrained triaxial tests (NC04 to NC11) were conducted on undisturbed clay obtained from the same depth (9 meters) at the Kärra test site. This approach helps isolate variables that vary with depth, such as density or soil composition, making it easier to evaluate test results and calibrate soil behavior prediction models (Tahershamsi et al., 2023). The testing plan was focused on cyclic loading relevant to the high-speed railway lines planned in Sweden. The entire test was conducted under stress-controlled conditions. The loading stages for all NC samples are shown in Figure .1 in Appendix - A. The summary of the test plan is presented in the table 3.4 below:

Table 3.4: Characteristics of cyclic loading variables in NC samples

Sample type	Stage Number	Loading Stages	Cyclic loading duration	Cycles nr	p0	q0	qp	qavg	qcyc	qcyc/p0	CSR	qcyc/2Su	qavg/2Su	Cyclic failure
-	-	-	(days)	-	(kPa)	(kPa)	(kPa)	(kPa)	(kPa)	-	-	-	-	-
NC04	1	I, J, K, L, M, N	16,98	8148	53.8	28	19	47.014	4.965	0.0922	0.03761	0.07521	0.712	No
NC05	1	I, J, M, N	30,74	14755	49.5	28	0	28.0671	4.93	0.0995	0.03734	0.07469	0.425	No
NC06	1	I, J, M, N	57,09	27401	51.1	29.7	0	28.9950	9.88	0.1936	0.07488	0.14976	0.451	No
NC07	1	I, J, M	100,97	48438	55.7	29.1	0	29.023	19.59	0.351	0.14817	0.29634	0.441	Yes
NC08	1	I, J, K, L, M	1,26	599	53.2	28.6	9.2	36.64	19.53	0.367	0.14794	0.2959	0.572	Yes
NC09	1	I, J, M	12,18	5835	52.6	28.3	0	28.123	27.14	0.516	0.20562	0.41123	0.429	Yes
NC10	1	I, J, K, L, M	21,22	10184	52.4	28.7	-18.4	9.45	21.67	0.414	0.16416	0.3283	0.156	Yes
NC11	1	I, J, K, L, M	0,19	89	49.5	27.9	-7.5	19.16	29.4	0.595	0.2230	0.4459	0.309	Yes

I = anisotropic consolidation, J = saturation, K = pre–shearing, L = creep, M = cyclic loading, N = post-cyclic (Tahershamsi et.al., 2023)

The table presents essential stage information. For more details, refer to Table .1 in the Appendix - B.

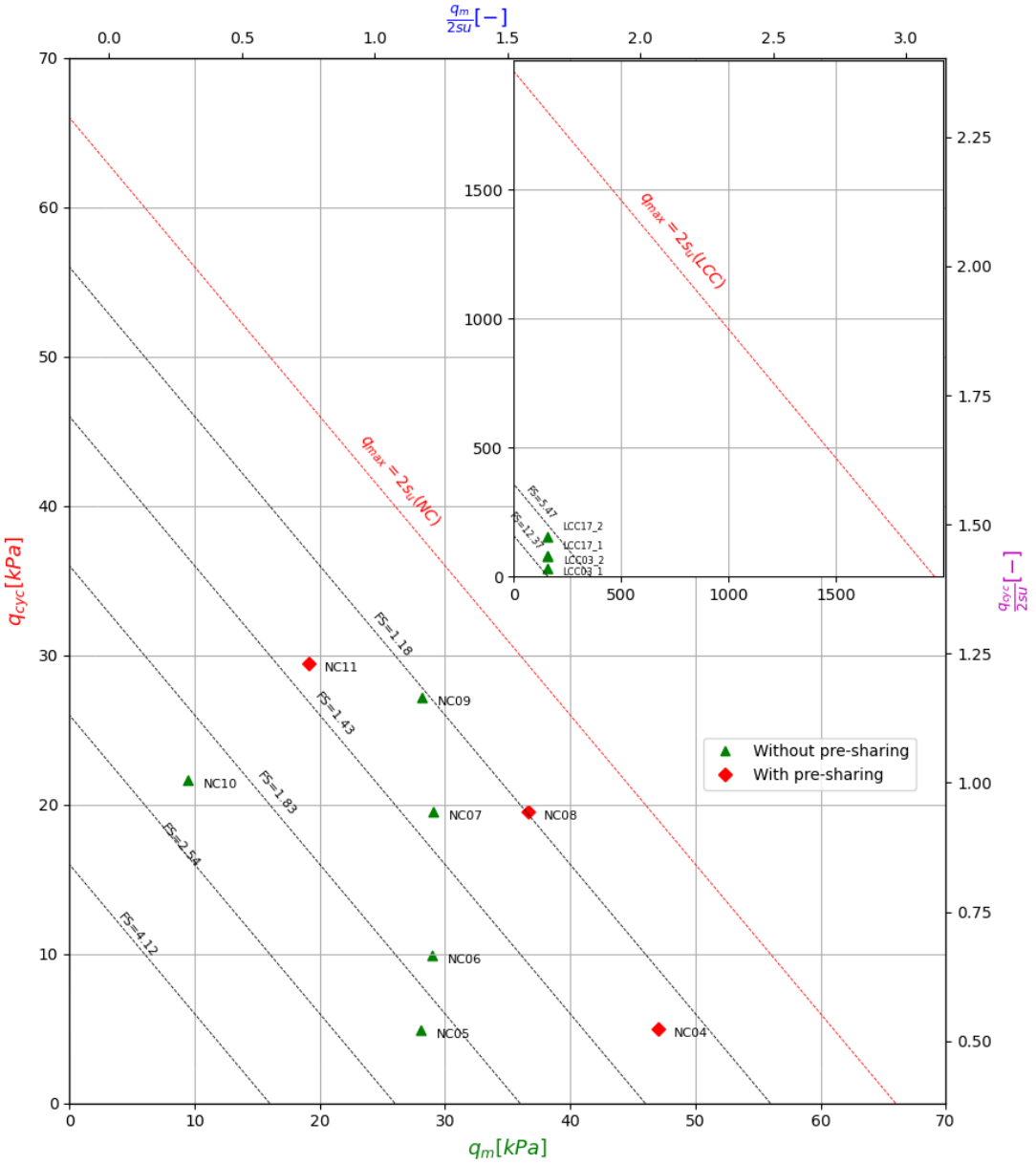

Figure 3.9: *Overview of samples tests of NC in relation to q_m and q_{cyc}* and comparison with test plan for LCC samples that show in the sub-plot

Figure 3.9, shows the test plan of NC samples. All samples comprise a single stage with varying loading stages. It can be seen that the three NC samples have a pre-shearing stage. The duration of cyclic loading differs for each sample, with only the NC07 sample exceeding 100 days due to containing more than 48000 cycles. The cyclic period was approximately the same as LCC test ($T \approx 180s$). Within the ($q_{cyc} - q_m$) test plan, it is evident that samples demonstrate variations in cyclic loading amplitudes (q_{cyc}) and mean deviatoric stress (q_m). Some of the natural clay samples were reached to failure during triaxial testing because they were very close to the maximum critical failure line (q_{max}) as shown in Figure 3.9.

Two sets of data were observed:

(Set 1) without pre-sharing: The cyclic loading amplitude (q_{cyc}) varied while the mean deviatoric stress (q_m) almost stayed constant.

(Set 2) with pre-sharing: The samples were subjected to an undrained pre-shearing step, which caused (q_m) to increase while fluctuating (q_{cyc}) to obtain a reasonable safety factors (FS).

The testing process involves allowing the water in the pores to reach equilibrium after the consolidation stage for several days. This step was taken to differentiate between two potentially confusing effects: slow deformation under continuous pressure (creep) and permanent distortion under repetitive stress (cyclic loading). There are some noticeable differences in the initial mean effective stress (p'_o) and initial deviator stress (q_o) because the extended equilibrium stage ensured that any cyclic loading effects would have disappeared before measurements were taken.

3.3 Maximum critical stress limit in $q_m - q_{cyc}$ space

The triaxial test plans for both the lime-cement and natural clay samples are illustrated in the ($q_m - q_{cyc}$) plots in Figures 3.8, 3.9. The critical maximum stress threshold (q_{max}) is represented by the red diagonal at a -45^o angle. The relationship $(q_{max} = 2s_u)$ for the critical diagonal line is established based on the research study of (Tahershamsi et al., 2023), which involves doubling the undrained shear strength (s_u).

The project used the results of the unconfined compressive strength tests from (Wong et al., 2023), as documented in Table 3.5 for the computation of the ($q_{max_{(LCC)}}$). This involved averaging the undrained shear strength ($s_{u_{avg}}$ = 979 kPa) of all six lime-cement samples used in the study, by considering their respective unconfined compressive strength values (q_u). Following the author's study, ($q_{max_{(LCC)}}$) was derived by equating ($q_u/2$) to the undrained shear strength (s_u) as mentioned below:

$$s_u = q_u/2 \tag{3.1}$$

$$q_{max_{(LCC)}} = 2 \times s_{u_{avg}} = 2 \times 979kPa = 1958kPa \tag{3.2}$$

Based on the ($q_{max_{(LCC)}}$) value, all the remaining diagonal lines were calculated using a uniform interval of 200 kPa along the x-axis (q_m) and the y-axis (q_{cyc}). The factor of safety (FS) along a specific diagonal line is determined as the ratio of (q_{max}) to the

allowable deviatoric stress q_m.

$$FS = \frac{q_{max}}{q_m} \tag{3.3}$$

Based on the plots, it can be observed that LCC samples (LCC-3, LCC-17) are situated significantly distant from the critical maximum stress line, q_{max}, and exhibit higher safety factors ($FS = 5.47 \approx 12.37$) at varying cyclic amplitudes ($q_{cyc} = 31kPa - 153kPa$). The plot also supports the idea of high stiffness in both stabilized clay samples. But for the calculation of ($q_{max_{(NC)}}$) for natural clay, direct undrained shear strength from the monotonic test ($s_u = 33kPa$) was employed from the study of Tahershamsi et al.

$$q_{max_{(NC)}} = 2 \times s_u = 2 \times 33kPa = 66kPa \tag{3.4}$$

All the other diagonal lines were drawn with a 10 kPa gap along the (q_{cyc}) y-axis and (q_m) x-axis respectively. According to the NC test plan, it is evident that all NC samples are close to the maximum critical stress line compared to LLC test plan. However, three out of eight NC samples with pre-sharing are more closer to (q_{max}) with a factor of safety ($FS = 1.18 \approx 1.43$) compared to the other five tests. Upon comparing LCC with NC test plans, observations indicate that the lime cement samples exhibit an approximately 30-fold increase in safety margin over the natural samples before reaching the maximum critical stress limit (q_{max}).

Sample	q_u (MPa)	E (MPa)	E_{tan} (MPa)	E_{sec} (MPa)	E_{50} (MPa)	local (MPa)
S7	2.37	247.10	24.48	247.10	267	1424.36
S8	2.53	398.90	38.19	344.30	305.60	3122.30
S9	1.03	230	11.72	203.60	234.80	589.24
S10	1.34	199.70	7.67	112.50	211.30	1425.50
S11	1.92	305.90	6.70	235.40	312.70	-
S12	2.56	335.60	6.30	268.60	319.50	-

Table 3.5: Strength & stiffness results from Unconfined Compressive Strength test (UCS) adapted from (Wong et al., 2023).

3.4 Data Pre-Processing

This section explains the pre-processing steps in Python to analyze cyclic triaxial raw data. Figure 3.10 shows a flowchart outlining the step-by-step pre-processing with advanced data optimization strategies. The primary objective is to effectively manage GDS files containing extensive data cycles from two different samples: NC, and LCC. Furthermore, the goal is to derive stiffness parameters as output using this established tool accurately. The pre-processing complexities have been carefully addressed to ensure robust data preparation for subsequent analysis. All Python codes are uploaded on GitHub, and for readers' interest access is granted through this (GitHub Link).

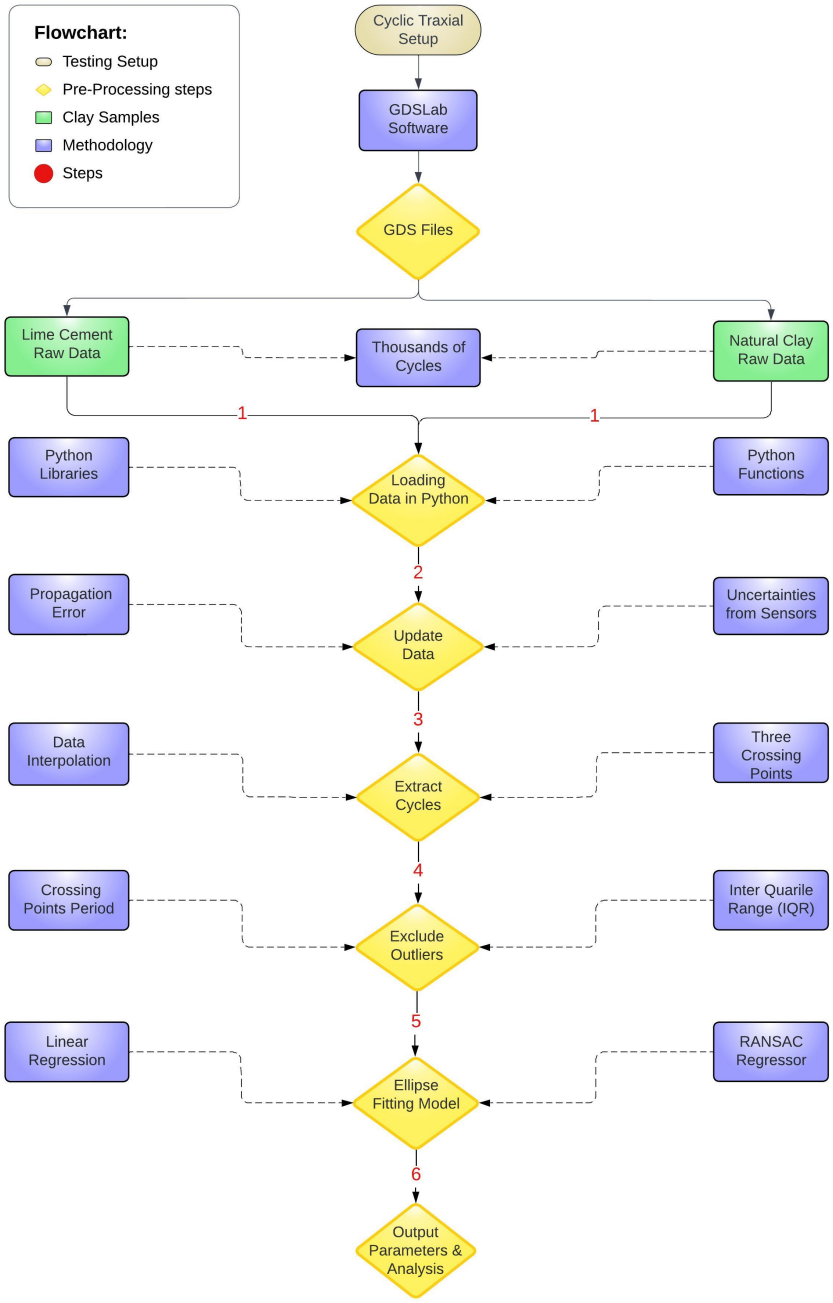

Figure 3.10: *Flowchart illustrating Data Pre-Processing steps*

3.4.1 Step 1: Loading GDS data in Python

Different Python libraries and functions were utilized to load and extract relevant information from the GDS cyclic raw data files efficiently. (Pandas, pd) library provided great features for labeled arrays (series) and spreadsheet-like structures (data frames). For numerical computation, the (NumPy, np) efficiently employed mathematical calculations and multidimensional arrays for data analysis. To extend the functionality of (Numpy, np), (interpolate, and stat), SciPy extensions were utilized to estimate crossing points and for powerful statistical analysis. (Matplotlib) was used to produce a variety of Python visualizations, including interactive plots, static charts, polygons, and ellipse-fitting modeling. To manage calculations with uncertain quantities and understand how

uncertainties propagate and affect calculations, (Uncertainties) libraries were used. In the case of identifying linear trends in the data using (Scikit-learn), outliers posed a challenge. To address this, (RANSAC Regressor) was employed which is a robust alternative that provided a more reliable fit, demonstrating the versatility and adaptability of Python libraries in data analysis and visualization.

The data processing involves more than just calculating the area and volume of the sample. It involves various other functions to handle relative uncertainty, calculate mean uncertainty, determine the polygon's centroid, and analyze the loading stages through calculation steps for different cyclic loading parameters, etc. After carefully selecting the necessary libraries and implementing the required import functions, cyclic raw data files were successfully loaded into the coding environment and revealed testing information for each stage as shown in Table .1 in Appendix - B.

Refer to Appendix - C sections C.1.1, and C.1.2 for specific code details about these libraries and functions.

3.4.2 Step 2: Data files updated

Once the necessary data loading process has been completed, the next step involves obtaining a list of all the column names and displaying the total number of data rows. Following this, the relative uncertainties associated with laboratory measurements were included in our dataset. New index columns containing uncertainties were generated, and each sample's GDS files were updated accordingly. Subsequently, the stage information tables were revised to reflect these updates. The uncertainties and propagation error calculations will be discussed in detail in section 3.5.

3.4.3 Step 3: Extracting cycles

While plotting the data, distinct cyclic loading stages for different samples were discovered with a minimal variation in cyclic amplitudes. It relied on the initial mean deviatoric stress (q_m) represented by the red line in the plots to separate individual cycles. The cyclic plot showed a discrepancy where the starting and ending points of cycles did not intersect with the mean deviatoric stress (q_m) line. To obtain crossing points between cyclic data and (q_m) line, the existing cyclic points were interpolated. However, it's important to note that the interpolated points were not utilized in our extensive calculations. They were just employed to isolate cycles. Three specific crossing points as in Figure 3.11, between the mean deviatoric stress (q_m) line and the cyclic data points were identified to extract individual cycles with an approximate cyclic period $T \approx 180s$ and corresponding frequency (Hz) for each cycle as shown in Table .1 in the Appendix - B.

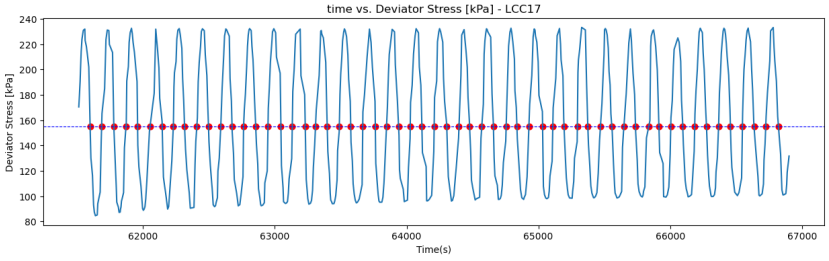

Figure 3.11: *Crossing points between the cycles and the mean line of the stress*

The plots for individual cycles between time (s) and deviatoric stress (q), revealed numerous outliers in the data, which could compromise the modeling of the fitted ellipse into the next-step. These outliers were eliminated based on the crossing points period of less than 20 seconds. During analysis, It was observed that the majority of crossing points exhibited intervals exceeding 20 seconds during each cycle. However, a few cycles displayed crossing points with intervals of less than 20 seconds (distorted cycle) in close proximity. In this case, intersection points less than 20 seconds intervals were considered outliers and terminated from data as shown in Figure 3.12.

Refer to Appendix - C sections C.1.4, and C.1.5 for specific code details about crossing points and individual cycle extractions.

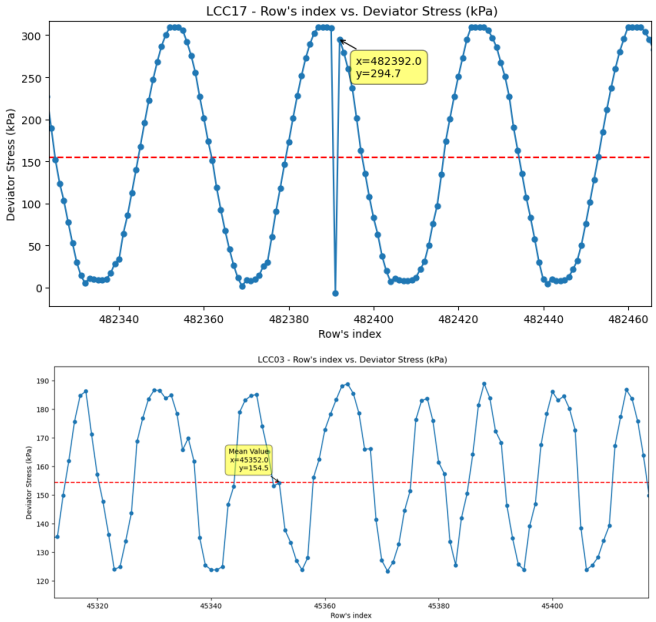

Figure 3.12: *Short intersection with the mean line leads to outliers in the cycles*

3.4.4 Step 4: Exclude outliers from the data

After removing cyclic outliers, more outliers that fall far outside the expected range due to potential errors in the data were discovered and they might significantly skew the interpretation of results. The next step involved carefully filtering the cyclic data and removing all these outliers before fitting the ellipse. This procedure aimed to detect and eliminate outliers by employing the Inter Quartile Range (IQR) as a statistical measure, with the outlier's lower and upper boundaries set at factor ($\pm 1.5 \times IQR$). However, in some samples, the lower boundary was excluded and solely considered the upper boundary to avoid the potential high risk for uncertainty in the coding. Figure 3.13 shows the removal of the outliers by IQR.

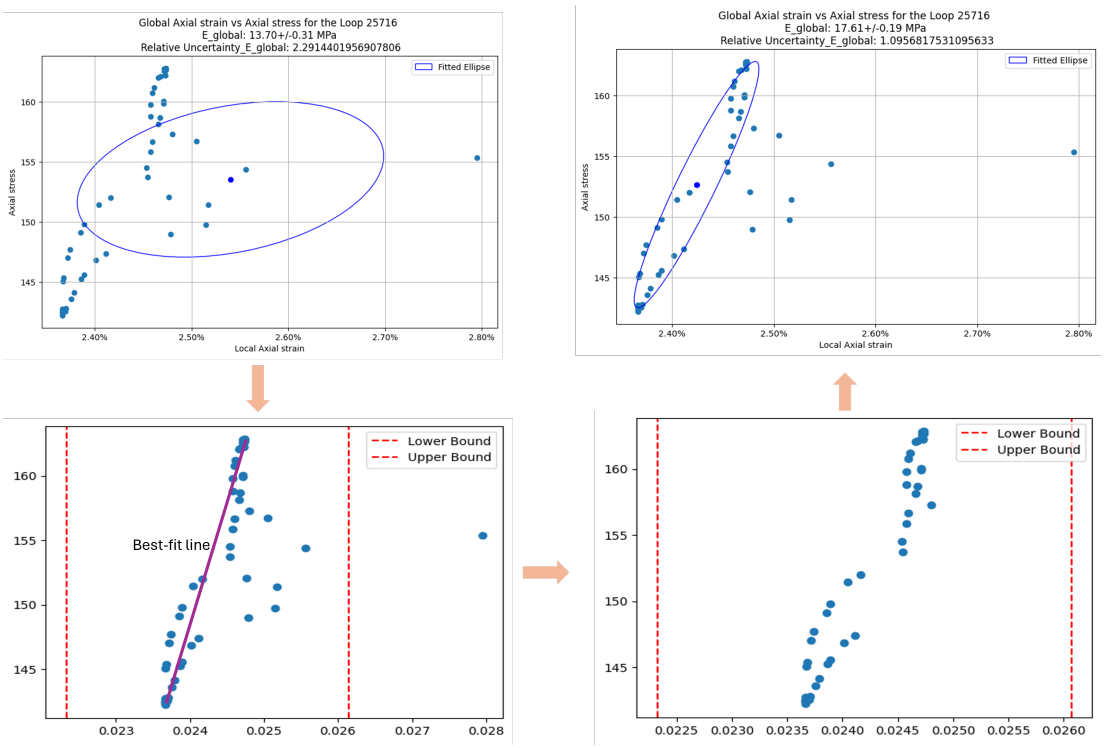

Figure 3.13: *Removing the outliers by IQR*

In statistical measures, the Inter Quartile Range (IQR) denotes 68% distribution of the dataset, extended from 25th to 75th percentiles. By introducing a factor of $\pm 1.5 \times IQR$, the range of distribution to 95% in the data was expanded effectively. Adjusting this factor enables us to selectively exclude outliers from the dataset, with the value of factor (1.5) modifiable to suit the specific characteristics of the outliers in the dataset. Furthermore, utilizing the IQR function in programming facilitates mitigating outlier influence on the dataset. The Figure 3.14 illustrate the IQR methodology used in the study.

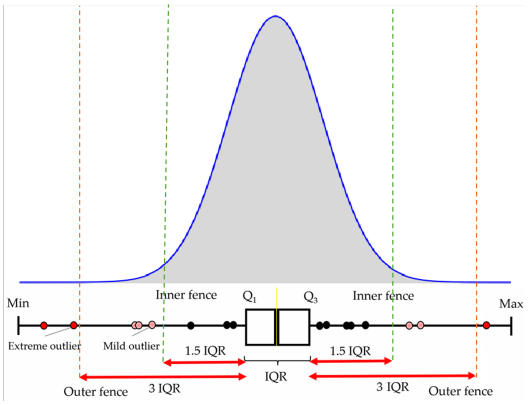

Figure 3.14: *IQR method, redeveloped from Dastjerdy et al. (2023)*

3.4.5 Step 5: Ellipse fitting modeling

Two additional functions have been implemented to address potential outliers that may not have been detected by the initial method, the Inter Quartile Range (IQR). The first

approach involves utilizing linear regression to determine the best-fit line (slope) of the stress-strain cycle, representing the ellipse's major axis. This major axis's maximum and minimum points, center, and inclination (α) were identified. However, the minor length remains undiscovered. These three ellipse parameters (inclination (α), major, and minor axis) are interrelated and crucial for ellipse fitting modeling as shown in Figure 3.15. To address the minor axis, RANSAC regressor function was used in the coding. This methodology has proven more effective than directly applying simple ellipse fitting modeling, as the latter may incorporate outliers and fail to yield a satisfactorily fitted ellipse for all cycles. The utilization of these functions has resulted in the attainment of well-fitted ellipses for all cycles. Refer to the Figures .4, and .3 in Appendix - A for all identified ellipses for all cycles for LCC and NC after ellipse fitting modeling respectively.

3.4.6 Step 6: Output parameters & analysis

In the last step, after fitting the ellipse, the area of an ellipse and a triangle were calculated as shown in Figure 3.15 the calculation of local stiffness's components for the Stress-local Strain cycle number 14311 which was taken as example. The major and minor length of the ellipse fitted are 2a = 310.24, 2b = 5.38×10^{-5} respectively.
The area of ellipse fitted for the cycle is as follows:

$$A_{ellipse} = \frac{\pi * 2a * 2b}{4} = \frac{\pi * 310.242 * 5.38 \times 10^{-5}}{4} = 0.01311 \tag{3.5}$$

The area of triangle which as shown in Figure 3.15d calculated as follows:

$$A_{triangle} = \frac{A * B}{2} = \frac{310.238 * 0.000232}{2} = 0.036 \tag{3.6}$$

That damping ratio (D) was derived using equation 2.17.

$$D = \frac{A_{ellipse}}{\pi A_{Triangle}} = \frac{0.01311}{\pi \cdot 0.036} = 0.1155 \tag{3.7}$$

The secant stiffness (E) value was obtained from the fitted ellipse slope using equation 2.13.

$$E = \frac{A}{B} = \frac{310.238}{0.000232 * 1000} = 1332.75\,[\mathrm{MPa}] \tag{3.8}$$

Propagation's error for value of local stiffness is calculated based on the relative uncertainty of stiffness which calculated in the section 3.5.

$$E_{error} = E \cdot Ru_{E \cdot LCC17 \cdot local} = 1332.75 \cdot 10.5\% = 139.94\,[MPa] \tag{3.9}$$

The value of local Stiffness with its uncertainty is as following:

$$E = 1332.75 \pm 139.94\,[MPa]$$

Additionally, the shear modulus (G) derived from the value of (E) using a specified equation (2.18) was computed.

$$G = \frac{E}{2(1+\nu)} = \frac{1332.75}{2(1+0.2)} = 555.31\,[MPa]$$

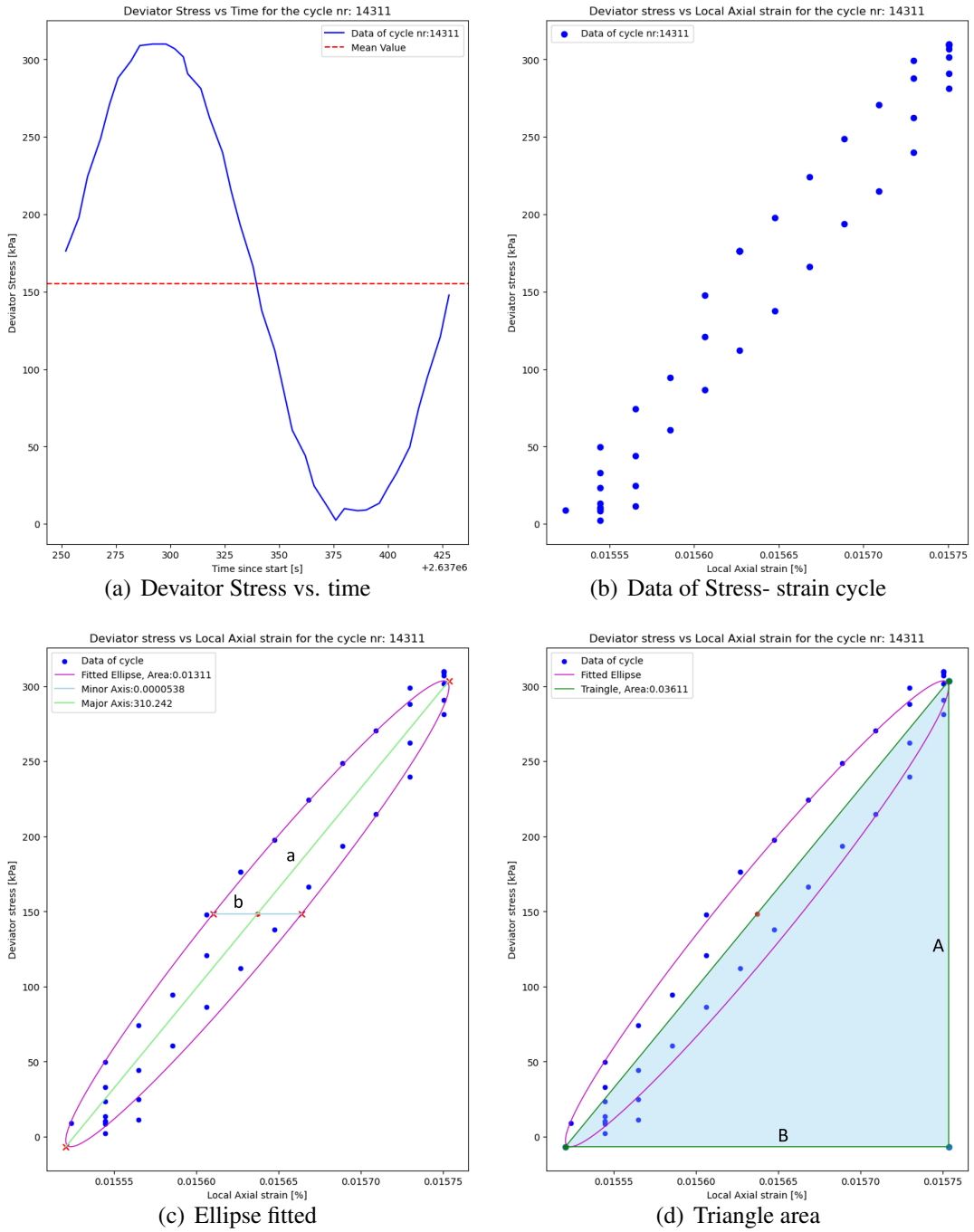

(a) Devaitor Stress vs. time

(b) Data of Stress- strain cycle

(c) Ellipse fitted

(d) Triangle area

Figure 3.15: One single cycle with area of the fitted ellipse and the triangle area

It is worth mentioning that all these parameters were derived with careful consideration of propagation error and the relative uncertainties associated with laboratory measurements. The results chapter 4 comprehensively describes diverse output plots for comparing the performance of lime cement and natural clays using these computed stiffness parameters.

Refer to Appendix - C sections C.1.6, and C.1.7 for specific code details about calculations of damping ratio (D), secant stiffness (E), and shear modulus (G) etc.

3.5 Calculating propagation error

3.5.1 Uncertainties in measurements

In this project, five types of uncertainties have been addressed:

1. Uncertainties in axial loading sensor
2. Uncertainties in displacement transducers
3. Uncertainties in the sample cross-sectional area.
4. Uncertainties in pore pressure transducer
5. Uncertainties in the cell pressure pump

The clay samples were not perfectly cylindrical, affecting the accuracy of the measurements. The NC and LCC samples were prepared using different methods. The NC samples were obtained using sampling tubes, resulting in a more consistent diameter. Therefore, the project discounted the potential error associated with NC sample diameter measurements. In contrast, the LCC samples in the project were part of a larger batch of XCT-scanned samples which was previously utilized by Wong et al. to assess the performance of lime-cement columns using a novel image-based method as described in (Wong et al., 2023). Notably, these samples were hand-cut, resulting in variations in their diameters ranging from 45 to 50 mm. Vernier Caliper measured the diameter at three different positions across the sample height, providing an average, reasonably accurate, but not highly precise measurement. As a result, there is some uncertainty in the sample's cross-sectional areas due to the Vernier Caliper's margin of error. This uncertainty is crucial, as it could significantly impact our stress calculations. Moreover, the measurements obtained from the linear displacement transducers and axial loading sensor used to measure the local axial strain (2 mm) during the cyclic triaxial test have uncertainty.

Datasheets and calibration files related to the relative uncertainties for global and local displacement sensors, axial loading sensors, cell pressure, and pore pressure were acquired from the Chalmers Geotechnical Lab on request. Refer to Appendix - B, Figure .11, for sensor calibration information. This propagation analysis aims to quantify the confidence interval for uncertainties related to laboratory measurement of axial stress, axial strain, secant stiffness (E_{50}), load, and cross-sectional area of the cylindrical sample. The goal is to observe how these uncertainties propagation affect the final results. There is a broader discussion about the uncertainty surrounding lime-cement columns with varying properties in different soil locations. This is due to uncertainty in determining the properties of the sample. The clay was stabilized in the laboratory with such a high stiffness that it was very tough to measure stiffness accurately.

3.5.2 Propagation Error analysis

The formula for calculating the propagation of uncertainty in a function f is as follows: if f depends on two or more variables x, y, ... with errors δ_x, δ_y, ...

$$(\delta f)^2 = \left(\frac{\partial f}{\partial x}\right)^2 (\partial x)^2 + \left(\frac{\partial f}{\partial y}\right)^2 (\delta y)^2 + 2\left(\frac{\partial f}{\partial x}\right)\left(\frac{\partial f}{\partial y}\right)\overline{\delta x \delta y} \tag{3.10}$$

If the variables x, y, .. are uncorrelated, $\delta_x \delta_y$ becomes insignificant and leading to a simplified equation:

$$\delta_f = \sqrt{\left(\frac{\partial f}{\partial x}\right)^2 \delta_x^2 + \left(\frac{\delta f}{\partial y}\right)^2 \delta_y^2} \tag{3.11}$$

And the relative uncertainty in f is as follows:

$$Ru = \frac{\delta_f}{f} = \sqrt{\left(\frac{\delta_x}{x}\right)^2 + \left(\frac{\delta_y}{y}\right)^2} \tag{3.12}$$

The Chalmers geotechnical laboratory staff provided the relative uncertainties associated with various measurement devices used during axial loading tests on a lime-cement clay sample. Specifically, The relative uncertainties in the axial loading sensor Ru_F, the axial displacement transducer for external LVDTs used for global strain $Ru_{d\cdot 50}$ and axial displacement transducer $Ru_{d\cdot local}$ used to assess the local axial 2 to measure local strain in the lime-cement clay sample were reported as 0.00%, 0.02%, and 0.105% respectively. Additionally, the relative uncertainty in pore pressure transducer Ru_w and relative uncertainty in cell pressure pump Ru_{c3} were also provided as 0.86% and 0.35%, respectively.

Uncertainty in the axial stress:
The propagation error in the axial stress σ_x is determined by evaluating the uncertainties in both the cross-sectional area of the samples and the applied axial load as follows:

The cross-section area is directly related to its diameter. Therefore, the uncertainty in diameter is determined by considering the variation observed in diameter measurements for the samples, which is between 45 - 50 mm for samples of LCC, and ignoring the variation in the diameters for samples of NC.

$$\delta_{D.LCC} = \frac{D_{max} - D_{min}}{2} = \frac{50 - 45}{2} = 2.5mm \tag{3.13}$$

$$\delta_{D.NC} = 0 \tag{3.14}$$

$$A = f(D) = \frac{\pi D^2}{4} \implies \frac{\partial A}{\partial D} = \frac{\partial}{\partial D}\left[\left(\frac{4}{\pi D^2}\right)\right] = \frac{\pi \cdot D}{2} \tag{3.15}$$

$$\delta A = \frac{\pi \cdot D}{2} \cdot \delta_D$$

$$\frac{\delta A}{A} = \frac{\frac{\pi \cdot D}{2} \cdot \delta_D}{\frac{\pi \cdot D^2}{4}} = \frac{2 \cdot \delta_D}{D} \tag{3.16}$$

The relative uncertainty in the axial stress Ru_{σ_x} can be determined using Equation (3.12) as follows:

$$\sigma_x = f(F, A) = \frac{F}{A}$$

$$Ru_{\sigma_x} = \sqrt{\left(\frac{\delta F}{F}\right)^2 + \left(\frac{\delta A}{A}\right)^2} = \sqrt{(0)^2 + \left(\frac{2 \cdot \delta_D}{D}\right)^2} = \frac{2 \cdot \delta_D}{D} \tag{3.17}$$

$$Ru_{\sigma_x \cdot NC} = \frac{2 \cdot \delta_D}{D_{NC}} = \frac{2 \times 0}{50} = 0 \tag{3.18}$$

$$Ru_{\sigma_x \cdot LCC03} = \frac{2 \cdot \delta_D}{D_{LCC03}} = \frac{2 \times 2.5}{47.32} = 0.106 = 10.6\% \tag{3.19}$$

$$Ru_{\sigma_x \cdot LCC17} = \frac{2 \cdot \delta_D}{D_{LCC17}} = \frac{2 \times 2.5}{47.82} = 0.105 = 10.5\% \tag{3.20}$$

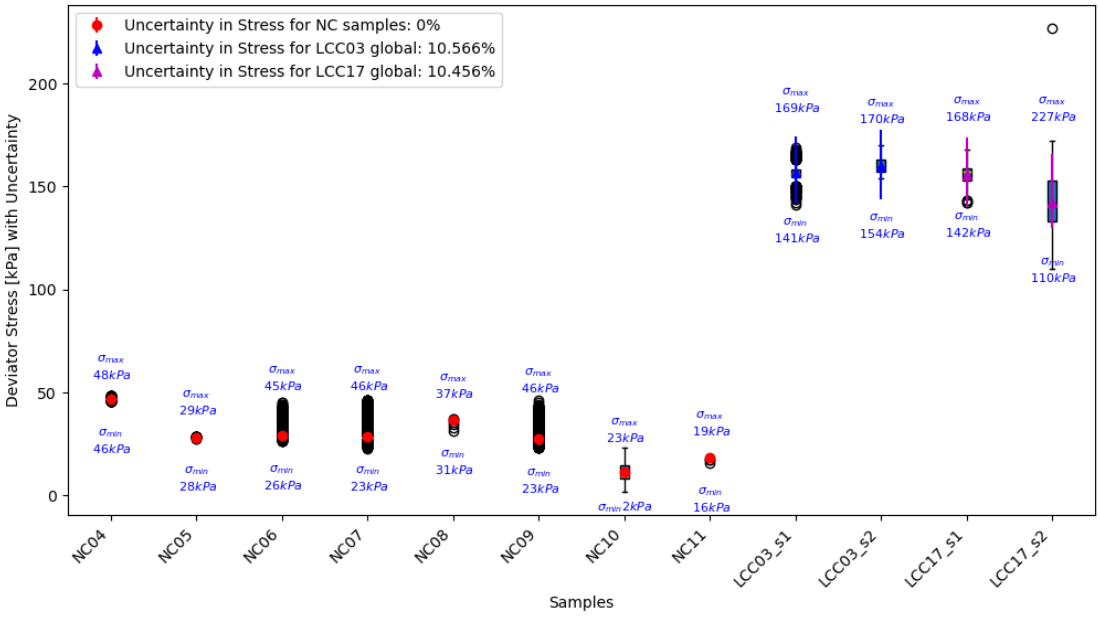

Figure 3.16: *Uncertainty in the stress measurements*

Uncertainty in the axial strain:
The uncertainty in the axial strain ε_x is determined by accounting for the uncertainties in both the axial displacement transducer for external LVDTs $Ru_{\text{d·50}}$ utilized for global strain and the height of the specimens or both the axial displacement transducer $Ru_{\text{d·local}}$ used to assess the local axial 2 to measure local strain and length of gauge as follows:

For global axial strain:
The uncertainty in the height of the specimens was calculated by considering the uncertainty in the Vernier caliper, which is used to measure the length of the gauge and height of the samples, is δ_c = ±0.018 mm (Bi et al., 2020).

The relative uncertainty in the axial strain $Ru_{\varepsilon_x \cdot 50}$ can be determined using Equation

(3.12) as follows:

$$\varepsilon_{x\cdot 50} = f(l, L) = \frac{l}{L}$$

$$Ru_{\varepsilon_{x\cdot 50}} = \sqrt{\left(\frac{\delta l}{l}\right)^2 + \left(\frac{\delta L}{L}\right)^2} = \sqrt{(Ru_d \cdot 50)^2 + \left(\frac{\delta L}{L}\right)^2} = \sqrt{(0.0002)^2 + \left(\frac{0.018}{L}\right)^2}$$

$$Ru_{\varepsilon_x \cdot NC\cdot 50} = \sqrt{(0.0002)^2 + \left(\frac{0.018}{100}\right)^2} = 0.00027 = 0.027\% \tag{3.21}$$

$$Ru_{\varepsilon_x \cdot LCC03\cdot 50} = \sqrt{(0.0002)^2 + \left(\frac{0.018}{103.36}\right)^2} = 0.000265 = 0.0265\% \tag{3.22}$$

$$Ru_{\varepsilon_x \cdot LCC17\cdot 50} = \sqrt{(0.0002)^2 + \left(\frac{0.018}{100.98}\right)^2} = 0.000268 = 0.0268\% \tag{3.23}$$

For local axial strain:
The uncertainty in the length of gauge was also calculated by considering the uncertainty in the Vernier caliper. Moreover, from Equation (3.12) the relative uncertainty in the axial strain $Ru_{\varepsilon_x \cdot local}$ can be calculated as follows:

$$\varepsilon_{x\cdot local} = f(lg, Lg) = \frac{lg}{Lg}$$

$$Ru_{\varepsilon_{x\cdot local}} = \sqrt{\left(\frac{\delta lg}{lg}\right)^2 + \left(\frac{\delta Lg}{Lg}\right)^2} = \sqrt{(Ru_d \cdot local)^2 + \left(\frac{\delta Lg}{Lg}\right)^2} \tag{3.24}$$

$$Ru_{\varepsilon_x \cdot local} = \sqrt{(0.00105)^2 + \left(\frac{0.018}{Lg}\right)^2}$$

$$Ru_{\varepsilon_x \cdot LCC17\cdot local} = \sqrt{(0.00105)^2 + \left(\frac{0.018}{48.57}\right)^2} = 0.0011 = 0.11\% \tag{3.25}$$

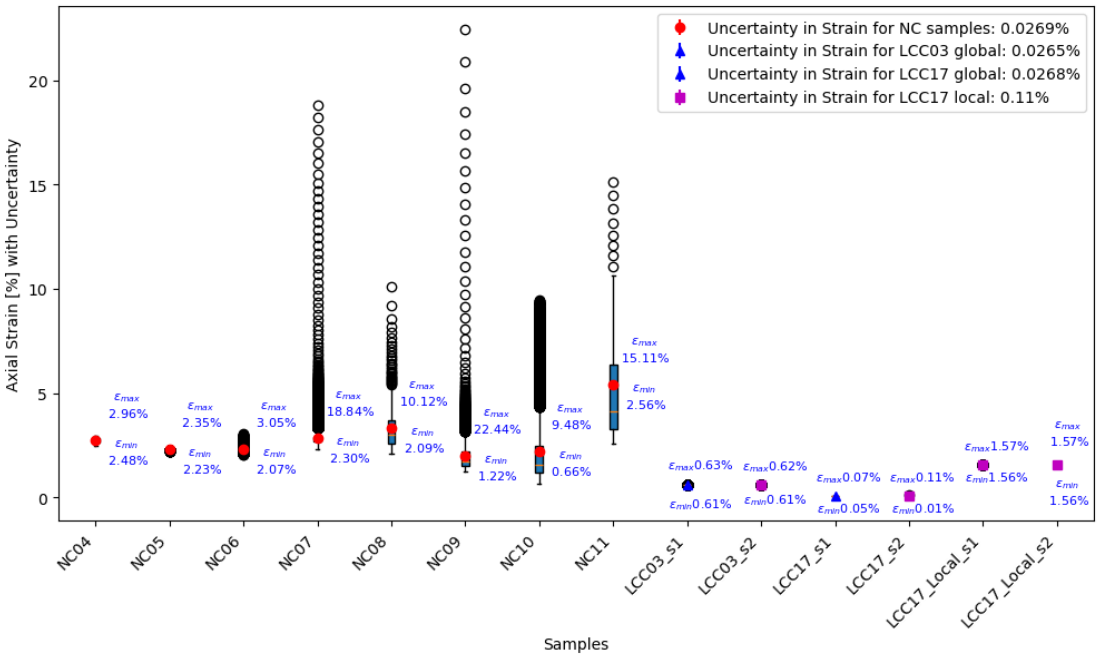

Figure 3.17: *Uncertainty in the strain measurements*

Uncertainty in the secant stiffness:
By applying the equation (3.12) the uncertainty in the secant stiffness E is determined by accounting for both the uncertainties in Axial strain and axial stress.

$$E = f(\sigma_x, \varepsilon_x) = \frac{\sigma_x}{\varepsilon_x}$$

$$\frac{\delta E}{E} = \sqrt{\left(\frac{\delta \sigma_x}{\sigma_x}\right)^2 + \left(\frac{\delta \varepsilon_x}{\varepsilon_x}\right)^2} \tag{3.26}$$

$$Ru_E = \sqrt{(Ru_{\sigma_x})^2 + (Ru_{\varepsilon_x})^2} \tag{3.27}$$

For global Stiffness:

$$Ru_{E \cdot NC \cdot 50} = \sqrt{(Ru_{\sigma_x \cdot NC \cdot 50})^2 + (Ru_{\varepsilon_x \cdot NC \cdot 50})^2} \tag{3.28}$$
$$= \sqrt{(0)^2 + (0.00027)^2} = 0.00027 = 0.027\%$$

$$Ru_{E \cdot LCC03 \cdot 50} = \sqrt{(Ru_{\sigma_x \cdot LCC03 \cdot 50})^2 + (Ru_{\varepsilon_x \cdot LCC03 \cdot 50})^2} \tag{3.29}$$
$$= \sqrt{(0.106)^2 + (0.00026)^2} = 0.106 = 10.6\%$$

$$Ru_{E \cdot LCC17 \cdot 50} = \sqrt{(Ru_{\sigma_x \cdot LCC17 \cdot 50})^2 + (Ru_{\varepsilon_x \cdot LCC17 \cdot 50})^2} \tag{3.30}$$
$$= \sqrt{(0.105)^2 + (0.000268)^2} = 0.105 = 10.5\%$$

For local Stiffness:

$$Ru_{E \cdot LCC17 \cdot local} = \sqrt{(Ru_{\sigma_x \cdot LCC17 \cdot local})^2 + (Ru_{\varepsilon_x \cdot LCC17 \cdot local})^2} \tag{3.31}$$
$$= \sqrt{(0.105)^2 + (0.00111)^2} = 0.105 = 10.5\%$$

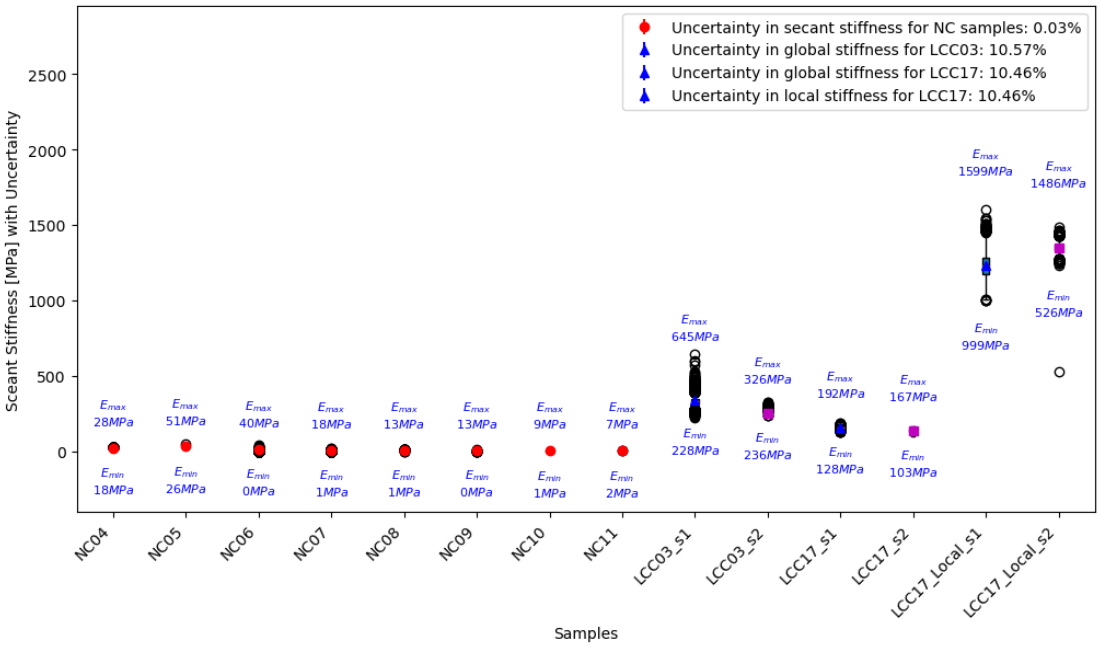

Figure 3.18: *Uncertainty in Secant Stiffness values*

Uncertainty in the deviator stress q:
The propagation error for the deviator stress q is as follows:
$\delta\sigma_3 = Ru_{c3} * \sigma_3$
$q = f(\sigma_1, \sigma_3) = \sigma_1 - \sigma_3 \implies \frac{\partial q}{\partial \sigma_1} = 1, \frac{\partial q}{\partial \sigma_3} = -1 \implies \delta q = \sqrt{{\delta\sigma_1}^2 + {\delta\sigma_3}^2}$

Uncertainty in pore pressure pwp:
The propagation error for pore pressure pwp is as follows: $\delta pwp = Ru_w * pwp$

Refer to Appendix - C section C.1.3 for specific code details about calculations of propagation error.

3.6 Strain Resistance

The capacity of a material, or a specific part of it, to resist deformation can be determined by estimating its response to incremental changes in force. The resistance is characterized by the ratio of the incremental force applied to the corresponding change it produces. This concept of resistance was first introduced by (Janbu, 1969), which mathematically can be represented as follows:

$$R = \frac{Incremental\ action}{Incremental\ response} \tag{3.32}$$

Later, (Janbu, 1985) suggested that the concept of resistance can be used to study the cyclic response of soils with a fixed stress amplitude (deviatoric stress). Within this context, resistance (R) is analogous to the slope of the tangent line drawn on the curve that represents the relationship between the cumulative irreversible strain (ε_{cu}) and the number of loading cycles (N) as shown in Figure 3.19.

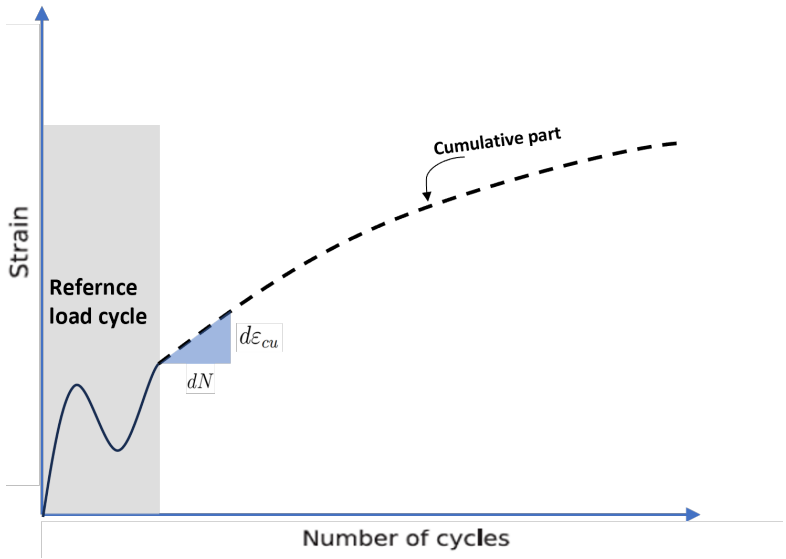

Figure 3.19: *An illustration depicting the correlation between cumulative strain and cycle numbers*

Equation (3.33) represents the strain resistance (R_ε), where (N) denotes the number of

cycles and (ε_{cu}) signifies the cumulative strain.

$$R_{\varepsilon} = \frac{dN}{d\varepsilon_{cu}} \tag{3.33}$$

Tahershamsi et al., stated that naturally sensitive clays in Sweden that show slight over consolidation due to creep processes, an increase in the strain ratio R_{ϵ} is observed nearly linearly with the progression of loading cycles (N). which can be written as;

$$R_{\varepsilon} = m_{\varepsilon} N \tag{3.34}$$

Upon plotting the number of cycles (N) against strain resistance (R_{ϵ}) using the methodology adapted from (Janbu, 1985), the resulting curve is obtained as shown in Figure 3.20.

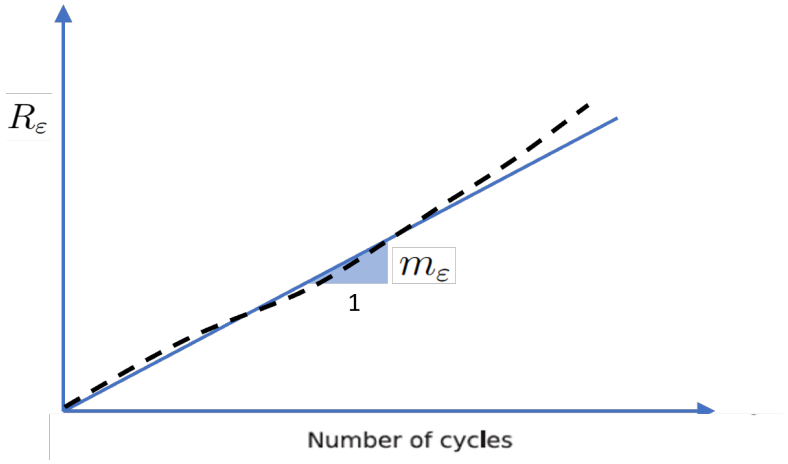

Figure 3.20: *An illustration depicting the linear correlation between R_{ε} and cycle numbers*

Similar curves were obtained for each sample as shown in Appendix - A Figures .5, .7, .6, .8. Identification of the slope of the curve line represents dimensionless strain number (m_{ϵ}). Notably, in the thesis work, the values of (m_{ϵ}) deviate slightly from those reported by Tahershamsi et al. in his thesis research. See Table 3.6 below for the calculated strain resistance numbers (m_{ϵ}) for LCC and NC tests. Further details on the strain resistance of LCC and NC tests are described in the results section, 4.5.

Table 3.6: Strain resistance number for the samples

LCC local	M_{ε}	LCC global	M_{ε}	NC without pre-shearing	M_{ε}	NC with pre-shearing	M_{ε}
LCC17	65079	LCC03	10700	NC05	1527	NC04	377
LCC17	50000	LCC03	29840	NC06	598	NC08	168
		LCC17	20202	NC07	278	NC10	673
		LCC17	10101	NC09	225	NC11	55

4 Results

The following section presents the results for both (LCC, and NC) generated through Python. The evolution of three main stiffness components, damping ratio (D), secant stiffness (E_{sec}), and shear modulus (G) are presented against the progressive cycle numbers (nr). Based on these three components, the subsequent comparison analyses between LCC and NC have been discussed, considering other stiffness-controlling parameters. It should be noted that the local case results of LCC3 were not included due to the reason mentioned in subsection 3.2.2. All results were obtained by considering the estimated propagation errors in the laboratory measurements.

4.1 Cyclic stress ratio CSR

The Figure 4.1 shows the CSR results of LCC and NC. The increasing values of CSR indicate that the clay is experiencing higher cyclic loading amplitudes (q_{cyc}). This can lead to excess pore water pressure generation and may eventually result in failure after a certain number of cycles. In the NC samples (CSR range 0.038 - 0.223), clays with higher CSR values are more prone to failure due to the substantial increase in cyclic loading, which significantly reduces stiffness. Therefore the NC samples (7, 8, 9, 11) failed during cyclic testing. The sample NC10 has fluctuations in deviatoric stress that produced unreliable results. Therefore NC10 is not handled so importantly in the subsequent analyses. In contrast to NC, the lower CSR values in LCC (0.008 - 0.039), demonstrate higher resistance to cyclic loading. This argument will be further verified later in the strain resistance investigation in section 4.5. Refer to Table .1 in Appendix - B for NC and LCC cyclic failure status during triaxial testing.

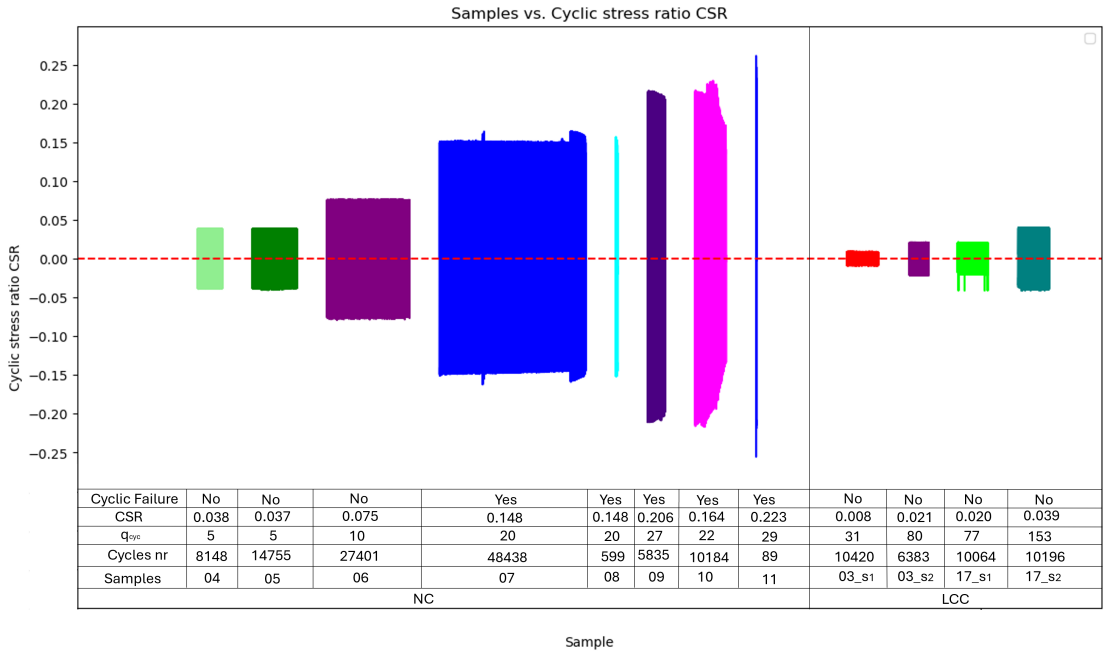

Cyclic Failure	No	No	No	Yes	Yes	Yes	Yes	Yes	No	No	No	No
CSR	0.038	0.037	0.075	0.148	0.148	0.206	0.164	0.223	0.008	0.021	0.020	0.039
q_{cyc}	5	5	10	20	20	27	22	29	31	80	77	153
Cycles nr	8148	14755	27401	48438	599	5835	10184	89	10420	6383	10064	10196
Samples	04	05	06	07	08	09	10	11	03_S1	03_S2	17_S1	17_S2
	NC								LCC			

Figure 4.1: *CSR for LCC and NC*

4.2 Damping ratio D

LCC samples:

The Figure 4.2 shows the results of damping ratio (D) for LCC samples. For global in the first stage ($q_{cyc} = 31.11kPa, 77.41kPa$), the damping ratios observed in both LCC3 and LCC17 showed slight fluctuations, ranging from (0.05 to 0.25) and (0.05 to 0.20) respectively. However, in the second stage ($q_{cyc} = 80.30kPa, 152.57kPa$), global LCC17 displayed an increase in the damping ratio (0.09 to 0.15) as the number of cycles and cyclic amplitudes increased. In contrast, global LCC3 exhibited a decreasing trend in the damping ratio during the same stage (0.18 to 0.08). In the local LCC17 analysis, a gentle increase in damping ratio (0.06 to 0.30) was observed during the first stage ($q_{cyc} = 77.41kPa$). Initially, the intact soil structure effectively dissipated the energy of cyclic loading. However, as the cyclic amplitude ($q_{cyc} = 152.57kPa$) increased, a decrease in the damping ratio (0.20 to 0.13) could lead to a slight stiffness degradation in the second stage. The local LCC17 showed a slight decrease in the damping ratio in the second stage at high cycle numbers (10^4), experiencing a 20% reduction from the first stage.

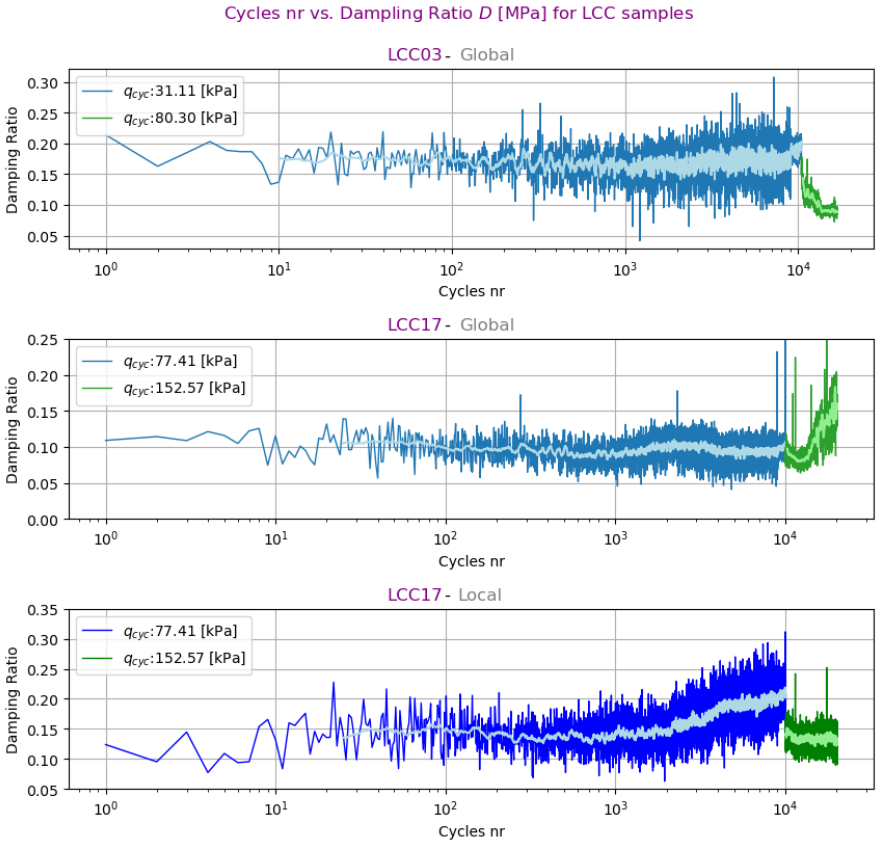

Figure 4.2: *Damping ratio D for LCC samples*

NC samples:

Compared to LCC, the natural clay (NC) tests showed different responses for damping ratio (D) in Figure 4.3. They initially exhibited consistent or very slight fluctuating behavior during the initial 100 cycles with high damping ratios at the lower cyclic amplitudes. However, at higher numbers of cycles exceeding 10^2 and 10^3 with progressive cyclic amplitudes from ($q_{cyc} = 4.96kPa - 29.43kPa$), the NC samples displayed a

sharp fluctuating and increasing trend in damping ratio ranging from (0.1 to 0.5). This contrasting behavior is due to damaged soil structure and its cumulative effect on clay stiffness, leading to a loss of the clay's ability to dissipate energy at a higher number of cycles effectively thus causing cyclic failures.

In contrast, the Natural Clay (NC) samples displayed a significant increase in damping ratio with increasing cyclic amplitudes at high cycle numbers (10^3) to 10^4). For instance, in the maximum case for NC09, the damping ratio increment is 80% after exceeding 10^3, however, for other samples, the increase is $50\% \approx 65\%$. This significant difference from LCC demonstrates the effectiveness of lime cement in improving clay's cyclic resistance.

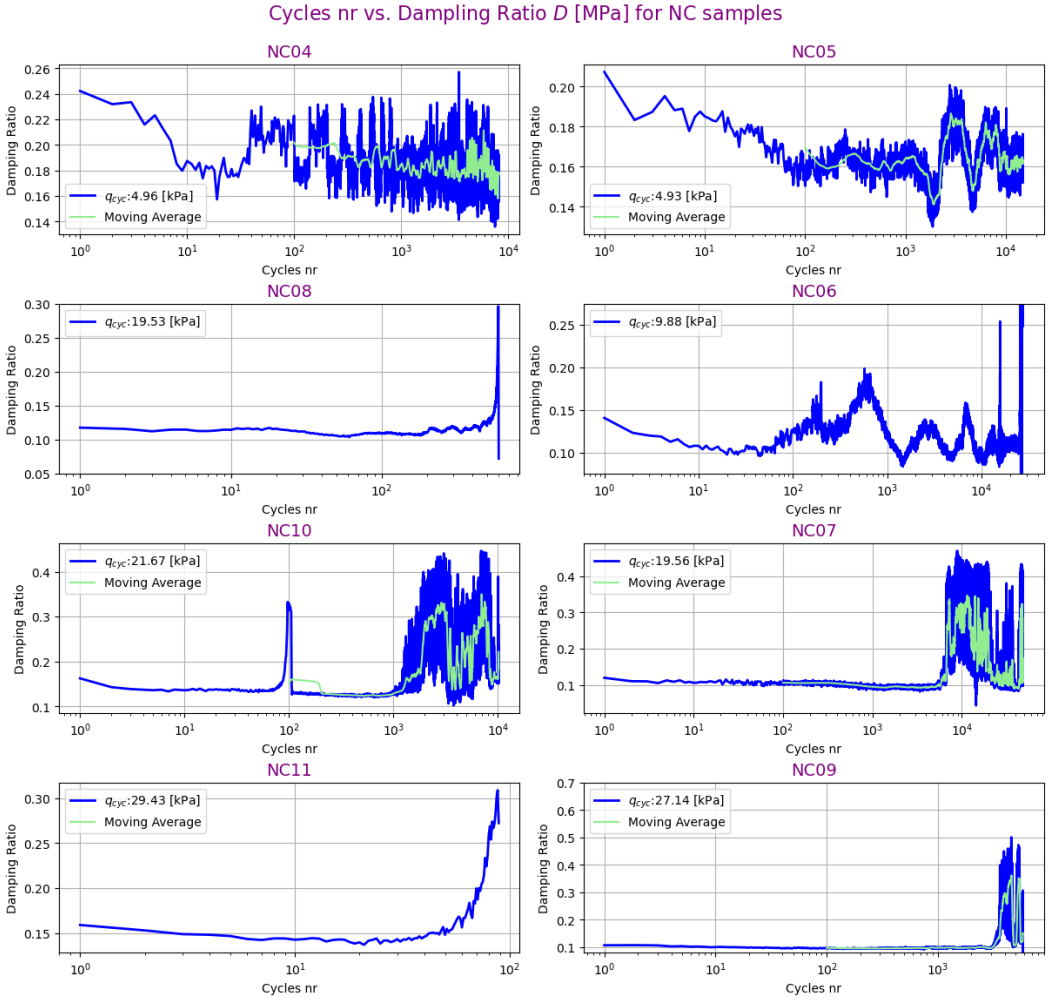

Figure 4.3: *Damping ratio D_{50} for NC samples*

4.3 Secant Stiffness E_{sec}

LCC samples:

The secant stiffness (E_{sec}) results for LCC samples are shown in Figure 4.4. The global secant stiffness (E_{50}) for LCC17 in the first stage ($q_{cyc} = 77kPa$), initially exhibited increasing behavior over 100 cycles and subsequently displayed a slight fluctuating trend (150 MPa to 180 MPa) during the rest of the first stage. In contrast, the (E_{50}) for LCC3 consistently increased throughout the first stage ($q_{cyc} = 31kPa$) ranging from

($250MPa \approx 600MPa$). However, both samples showed a reduction in global secant stiffness in the second stages with cyclic amplitudes ($q_{cyc} = 80kPa$), ($q_{cyc} = 153kPa$), and LCC3 ($400MPa \approx 250MPa$) and LCC17 ($160MPa \approx 110MPa$) respectively. These global measurements are meaningless as they incorporate information from the triaxial apparatus also. But still, this global estimation indicates that sample LCC3 is stiffer than sample LCC17.

The local secant stiffness (E_{local}) for LCC17 during the first stage ($q_{cyc} = 77kPa$) demonstrated a slight increase, ranging from ($1150MPa \approx 1450MPa$). However, in the second stage, with increasing cyclic loading amplitude ($q_{cyc} = 153kPa$) and at a higher number of cycles exceeding (10^4), it was observed to degrade slightly to approximately $1390MPa$. The test reported no cyclic failure in LCC samples under given cyclic loading amplitudes ($q_{cyc} = 77kPa, 153kPa$). The local secant stiffness (E_{local}) for LCC3 was not computed for reasons outlined in subsection 3.2.2.

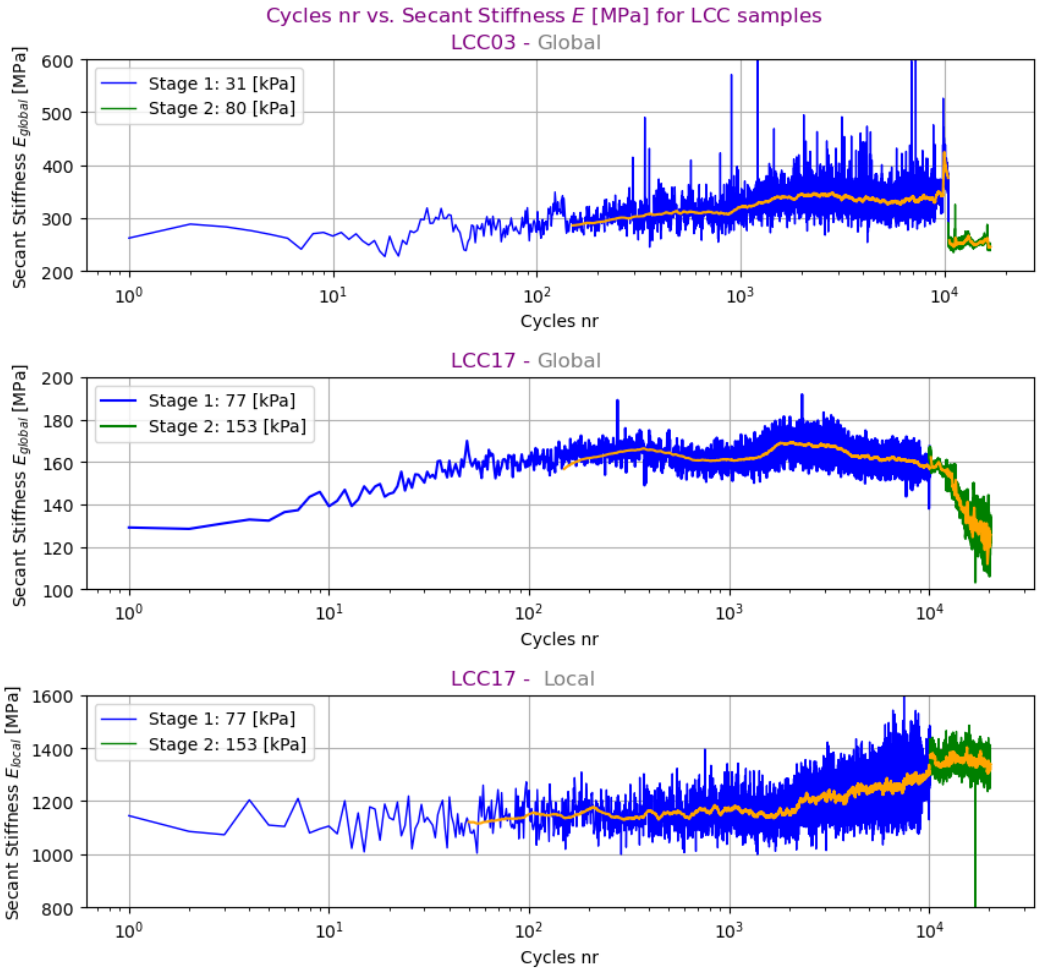

Figure 4.4: *Secant Stiffness E for LCC samples*

NC samples:
The provided Figure 4.5 represents the secant stiffness (E_{sec}) degradation of natural clays over successive cycles under varying cyclic loading amplitudes $q_{cyc} = 4.93kPa \approx 29.43kPa$ only for the global case. An initial clear gradual decline in (E_{sec}) occurs over

a hundred cycles 10^2. However, with an increase in the number of cycles after 10^2 and the cyclic amplitudes (q_{cyc}), a notable degradation in stiffness becomes apparent, leading to a sharp decline but with unclear downward curves. The global stiffness degradation range for all natural tests was approximately ($35MPa \approx 2.5MPa$), as compared to the global LCC samples ranging from LCC3 ($400MPa \approx 250MPa$) and LCC17 ($160MPa \approx 110MPa$) respectively. The natural samples NC07, NC08, NC09, NC10, and NC11 showed an abrupt decline in secant stiffness (E_{sec}) between cycle numbers (10^3) to (10^4) which casued sample failure. It is an important finding here that corresponding high CSR values were also observed for the same NC samples. The reason for this sharp decline and failure trend is also associated with the natural clay strain resistance number (m_ϵ) that will be further discussed later in the section 4.5.

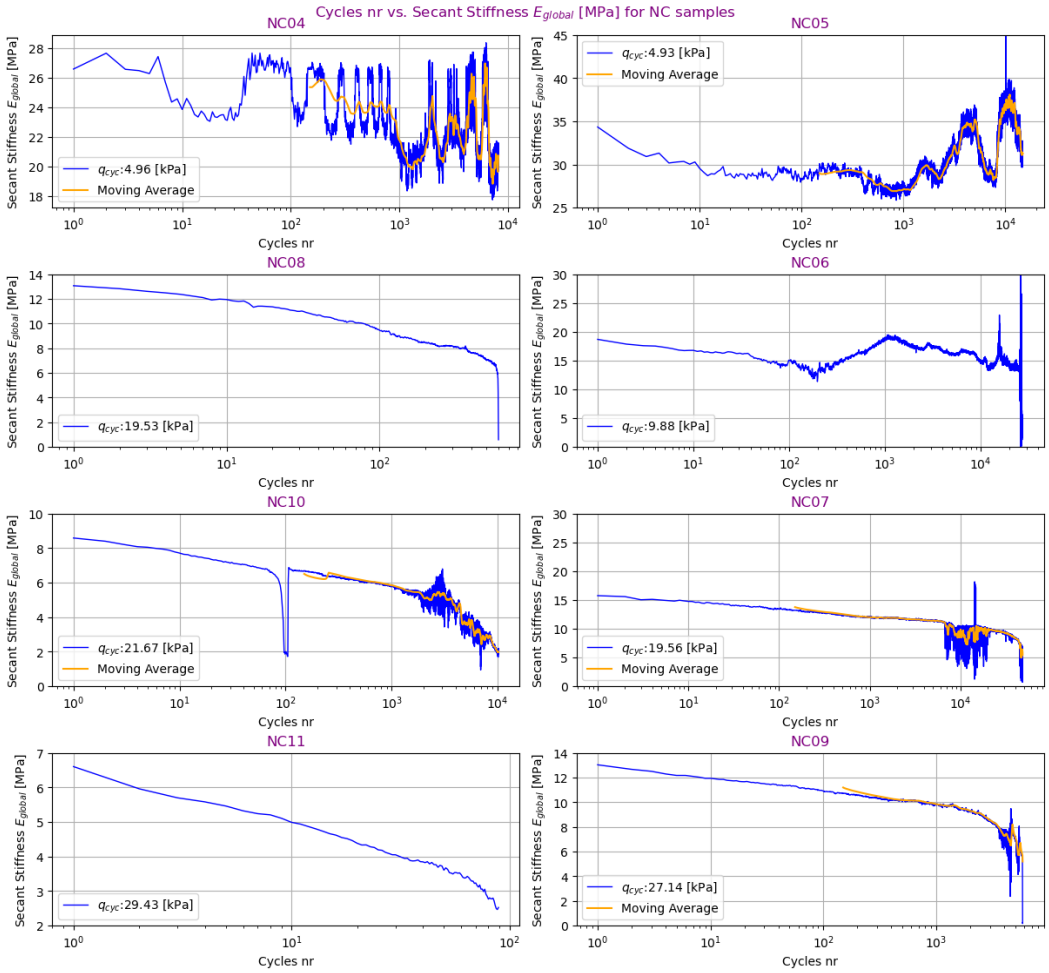

Figure 4.5: *Secant Stiffness E_{50} for NC samples*

4.4 Secant shear Modulus G_{sec}

LCC samples:

The plots in Figures 4.6 and 4.7 present the shear modulus (G) for LCC and NC tests. In the case of global LCC3, there is a reduction in G from (220 MPa to 90 MPa) during the first stage ($q_{cyc} = 31kPa$), with only minimal degradation ($122MPa \approx 95MPa$) during the second stage ($q_{cyc} = 80kPa$). The global shear modulus (G) in LCC17 shows uncertain trends, showing an increasing trend rather than a degrading behavior.

This could be due to strain hardening in the clay sample that increased its stiffness temporarily. However, these global shear modulus are not particularly so important for the discussion, as these measurements are not reliable as mentioned earlier in subsection 3.2.1.

Concerning the local shear modulus in LCC17, a slight degradation is observed. During stage 1, the G predominantly ranges from ($510MPa \approx 440MPa$). A marginal reduction in the local shear modulus ($605MPa \approx 550MPa$) is noted in stage 2, with an increased cyclic amplitude ($q_{cyc} = 153kPa$). Exactly the same trend for the modulus reduction curve is obtained when (G) is normalized by a constant (G_o) with increasing shear strain for LCC samples. Refer to Figure .9 in Appendix -A for the normalized modulus reduction curve. The corresponding shear strain range for two cyclic amplitudes (q_{cyc} = 78 kPa and 153 kPa) lies between 6.20×10^{-3} % and 9.90×10^{-3} %. According to Figure 2.22, mentioned in the background chapter, the range of shear strain 10^{-3} falls in a small strain region, and in the figure, it can be noticed that there is slight degradation trend in modulus reduction curve for this range. Therefore, the LCC shear modulus reduction curve can be compared with this strain range which reports no big difference in stiffness degradation in Figure .9.

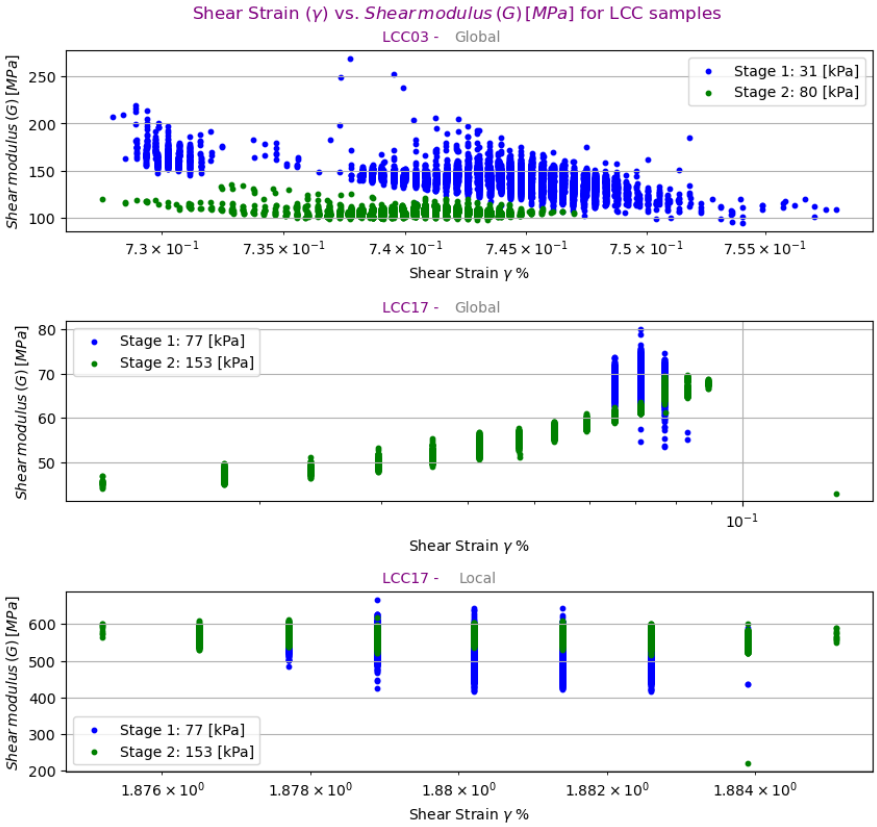

Figure 4.6: *Shear modulus G for LCC samples*

NC samples:
The NC tests exhibit shear modulus reduction behavior except for the NC04, and NC05 samples. In these two samples, the (G) fluctuates between values ($11.5MPa \approx 7MPa$)

and ($13MPa \approx 17MPa$) with increasing shear strain amplitudes (%). The plots also show that the degradation behavior is smooth for other samples. However, there are scattered points along the trend line in some parts. This could be due to damage accumulation. As the cyclic numbers increase, the clay structure may be damaged unevenly, leading to some areas weakening faster than others, causing scattering in the data points. Another potential reason could be the stiffness response of Illite mineral contents in the NC composition. Other NC samples NC06, NC07, NC08, NC09, NC10, and NC11 showed (G) degradation in the range of ($8MPa \approx 0.2MPa$).

There is a very similar modulus reduction curve trend in NC samples shown in Appendix -A Figure .10 like shear modulus (G) with increasing shear strain (%).

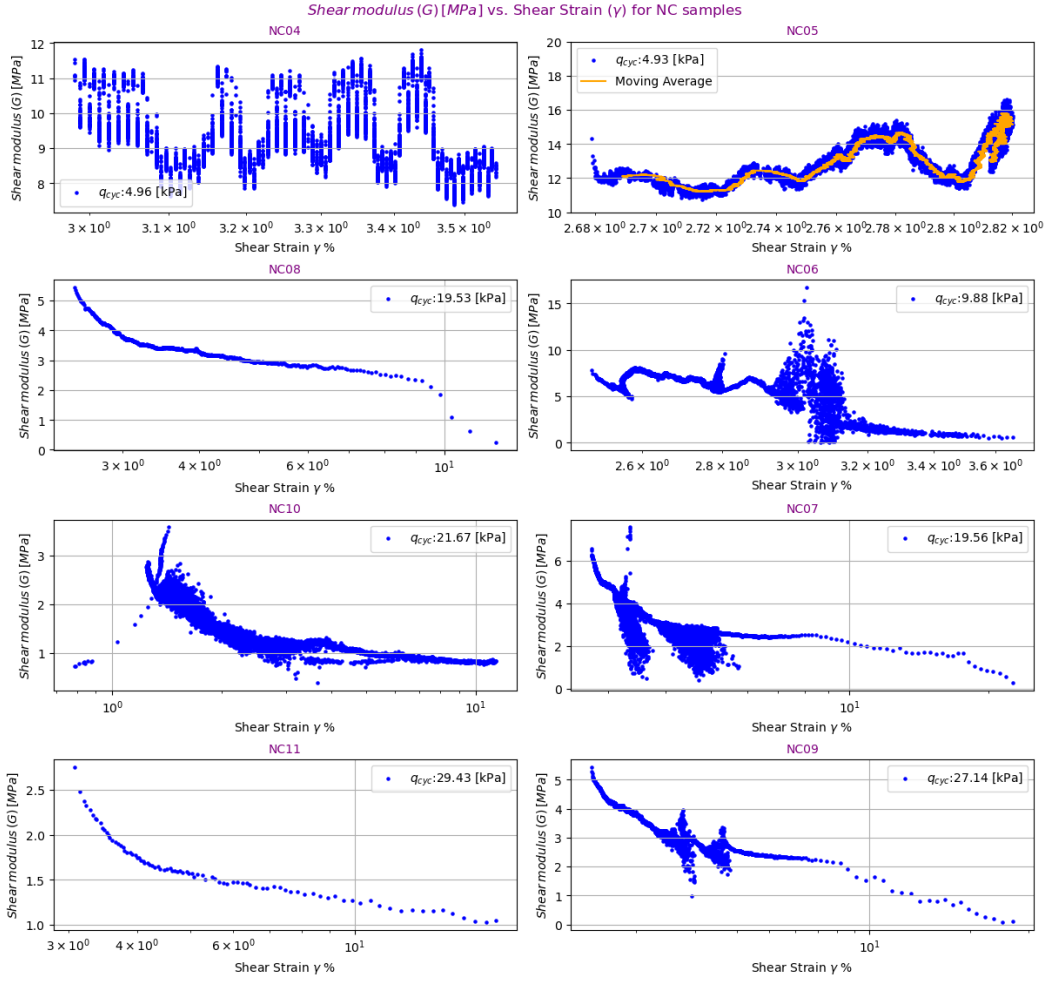

Figure 4.7: *Shear modulus G for NC*

4.5 Strain Resistance R

After computing the (m_ϵ) for each test, the LCC and NC samples were plotted between respective resistance numbers (m_ϵ) and shear mobilization value ($q_{\text{cyc}}/P'_{\text{o}}$) as shown in Figures 4.8, and 4.9. The given equations in the plots were adapted to draw a best-fit line for both samples. It should be noted here the NC10 sample was excluded from the analysis as it contained fluctuated cyclic loading amplitudes that might not have given the true shear mobilization value in the plot. Therefore it lies away and is not a part of

the pre-shearing line in natural clay samples. However, still, in the thesis, other stiffness parameters associated with NC10 were studied for comparing reasons. But in the strain resistance analysis, it was excluded.

In LCC plot, a hypothetical red vertical line was drawn that shows a cyclic failure. Both lime cement samples did not fail during cyclic tests. As it can be seen in the LCC17 plot the local stiffness has a very high value of resistance numbers ($m_\epsilon = 65000 \approx 50000$) under both cyclic amplitudes ($q_{cyc} = 77kPa, 153kPa$) compared to very less resistance values ($m_\epsilon < 1600$) of NC samples. This plot is very important as it signifies the true dynamic stiffness properties of the LCC samples. Although there is a stiffness degradation trend in local LCC17, it might still require very large cyclic loading amplitudes to predict its failure. The global LCC17 also shows a degradation trend with ($m_\epsilon = 20000 \approx 10000$) but its significance is not so important. In contrast LCC17, LCC03 first showed stiffness increment at first amplitude ($q_{cyc} = 31kPa$) but then showed degradation at second amplitude (($q_{cyc} = 80kPa$). Both global stiffnesss are meaningless as they include the stiffness of the overall triaxial setup so we cannot rely on the sample true stiffness value based on global measurement as already discussed in section 3.2.1.

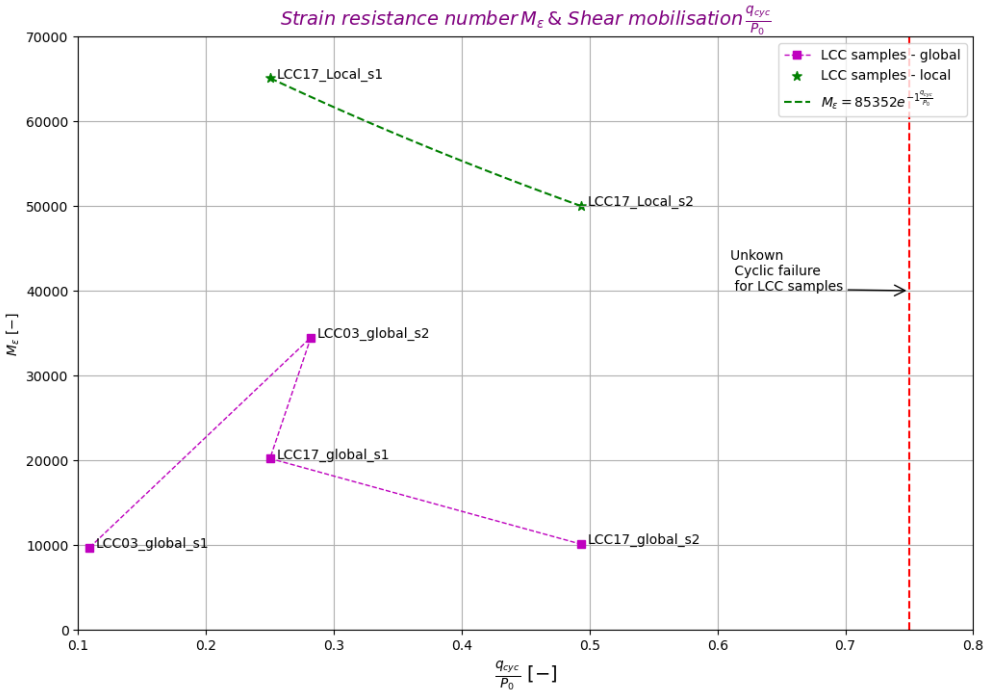

Figure 4.8: Strain resistance number m_ε in relation with shear mobilisation $q_{\text{cyc}}/P'_{\text{o}}$ for LCC samples

In the NC plot, a red vertical line was drawn to indicate cyclic failure, using the first NC sample failure as a reference point. The plot shows that samples NC07, NC08, NC09, and NC11 failed at resistance number values ($m_\epsilon < 245$). A higher resistance number (m_ϵ) corresponds to an increased capacity of the clay samples to withstand deformation. Connecting this information with Figure 4.5, now it is evident that these four NC samples started degrading at an early stage of cycles (10^2) because of lower strain numbers (m_ϵ), high CSR values in Figure 4.1 and high damping ratios in Figure

4.3 associated with them. Therefore, at higher cycle numbers (10^3) to (10^4) the samples could not resist much against deformation and failed.

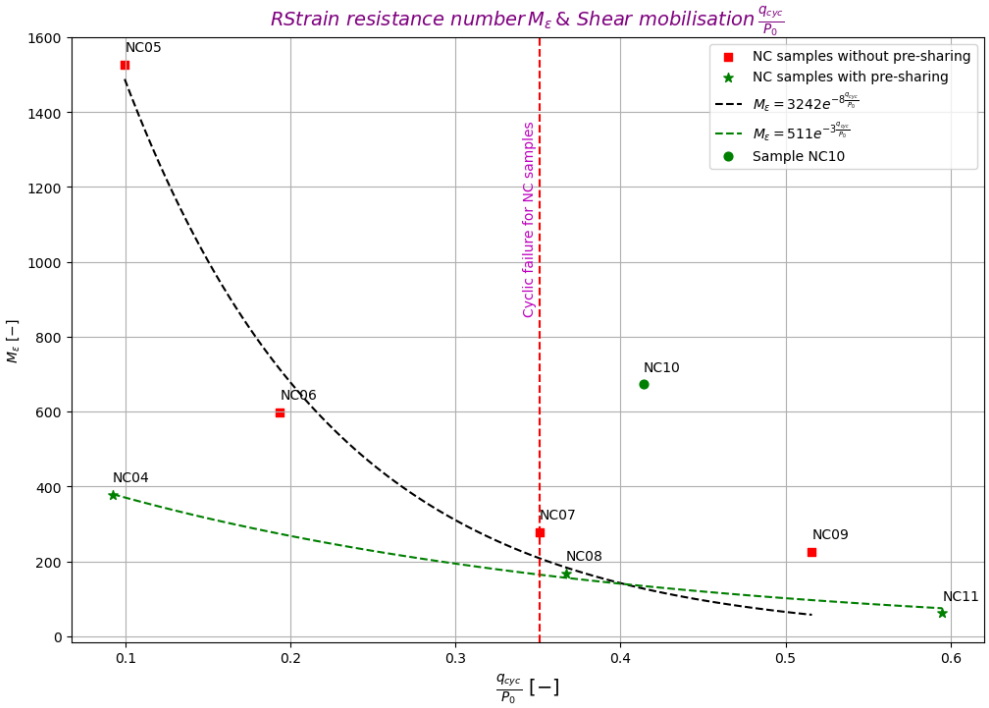

Figure 4.9: Strain resistance number m_ε in relation with shear mobilisation $q_{\text{cyc}}/P'_{\text{o}}$ for NC samples

4.6 LCC local transducer results

Figure 4.10 illustrates exciting trends in the secant stiffness (E_{sec}) and damping ratio (D) with a tenfold cycle increase for two different cyclic amplitudes (q_{cyc} = 78 kPa and 153 kPa). The corresponding axial strain range for these two cyclic amplitudes lies between 5.10×10^{-3} % and 8.20×10^{-3} % with the effect of $\pm$ 0.11% relative uncertainty in the local axial strain measurements. At a cyclic amplitude of 78 kPa, the stiffness is inconsistent with each tenfold cycle increase. There is an initial slight decrease of around 4% (1150 MPa to 1105 MPa), followed by a more prominent increase of around 12% (1105 MPa to 1245 MPa). However, the stiffness further fluctuates with another decrease of 6% (1245 MPa to 1170 MPa) at 10^3 cycles and a final increase of around 10% (1170 MPa to 1310 MPa) at 10^4 cycles. This behavior suggests the absence of a clear degradation trend at this lower amplitude, instead it is fluctuating. In contrast, the response at the higher cyclic amplitude (153 kPa) shows a different pattern. Here, the stiffness remains relatively stable with minor variations throughout most cycles, showing a slight overall increase of less than 1% up to 10^3 cycles. However, at the highest cycle number 10^4, a slight decrease of around 4% (1370 MPa to 1310 MPa) is observed with effect of $\pm$ 10.5% relative uncertainty in local stiffness measurements. Connecting this information with Figure 4.4 makes it more clear. This indicates a possible delayed degradation trend that becomes more pronounced only at higher cycle numbers. These LCC local behavior findings are very important as they provided promising results supporting the thesis hypothesis that adding lime cement significantly reduces stiffness degradation.

The 78 kPa amplitude demonstrates a damping ratio (D) that initially increases, followed by a significant decrease and a substantial recovery, indicating complex material behavior under each ten-fold cycle increase. In contrast, the 153 kPa amplitude exhibits a damping ratio that generally trends downward with some fluctuations, reflecting gradual stiffness degradation with a minor recovery. Connect this information with Figure 4.2 for clear understanding.

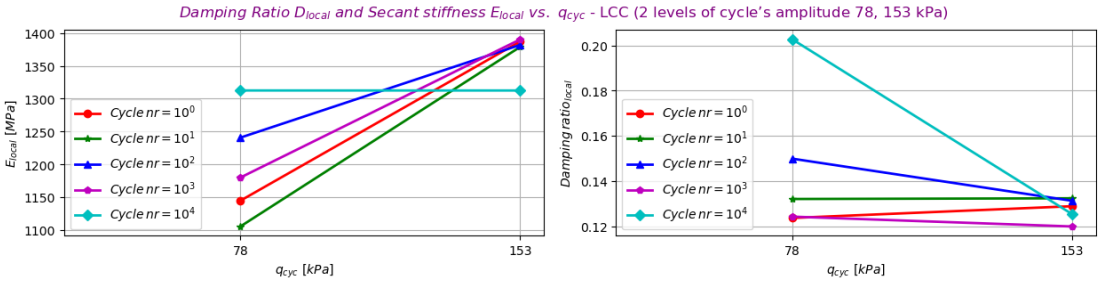

Figure 4.10: *Overview of local secant stiffness (E_{sec}) and damping ratio (D) for LCC tests in relation to cyclic loading amplitude (q_{cyc}) and cycle number (nr)*

4.7 LCC global transducer results

The global secant stiffness (E_{sec}) and damping ratio (D) for LCC tests at three different cyclic amplitudes (31 kPa, 78 kPa, 153 kPa) are shown in Figure 4.11. The corresponding global axial strain range for these three cyclic amplitudes lies between 2.50×10^{-2} % and 1.04×10^{-1} % with the effect of $\pm$ 0.0268 % relative uncertainty in global axial strain measurements. At cyclic amplitude ($q_{cyc} = 31kPa$) the global secant stiffness (E_{sec}) varies between (430 MPa to 250 MPa) with the effect of $\pm$ 10.5% relative uncertainty in global stiffness measurements. The plots indicate fluctuating patterns for the reduction of stiffness in the clay. The cycle numbers and the magnitude of the cyclic amplitude (q_{cyc}) interact complexly. At lower cyclic amplitudes (31 kPa), the clay initially appears stiffer with a few cycles (up to 100 cycles). However, with higher cycle numbers (beyond 10^4 cycles), stiffness significantly increased. On the other hand, for higher cyclic amplitudes (78 kPa and 153 kPa), the trend is more straightforward. Here, it can be observed a clear reduction in stiffness with an increasing number of cycles. Additionally, at any given number of cycles, the stiffness consistently decreases with increasing cyclic amplitude. However, the global measurement is not reliable as it also counts the stiffness of the triaxial apparatus as mentioned in subsection 3.2.1. But still, it provides information to compare the global transducer case of LCC with NC samples.

At ($q_{cyc} = 31kPa$), the damping ratio initially increases, then decreases, finally showing recovery. At 78 kPa, there is a consistent decrease, reflecting a the continuous reduction in damping ratio. When the q_{cyc} reaches 153 kPa, the damping ratio again fluctuates with minor changes initially but increases substantially (0.20) at higher cycles 10^4, suggesting a significant change in material behavior under higher loading conditions.

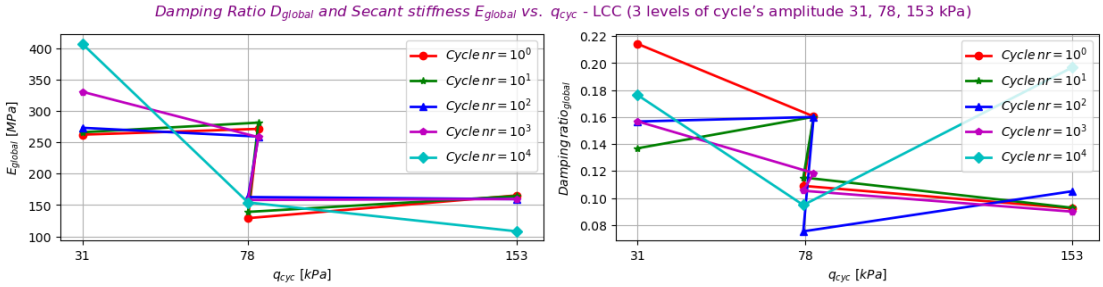

Figure 4.11: *Overview of how global damping ratio D and undrained global secant stiffness E_{sec} for Lime-cement clay degrades in relation to cyclic loading amplitude q_{cyc} and cycle nr*

4.8 NC global transducer results

The secant stiffness (E_{sec}) degradation and damping ratio (D) for NC tests without pre-shearing at four different cyclic loading amplitudes ($q_{cyc} = 5, 10, 20, 27kPa$) is presented in Figure 4.12. The corresponding axial strain range for these four cyclic amplitudes lies between 2.81×10^{-4} % and 3.30×10^{-3} % with the effect of $\pm$ 0.027% relative uncertainty in the global axial strain measurements. For the lowest amplitude ($q_{cyc} = 5kPa$), the secant stiffness (E_{sec}) lies between 38 MPa and 27 MPa with the effect of $\pm$ 0.027% relative uncertainty in global stiffness measurements. It can be noticed that the secant stiffness (E_{sec}) consistently decreases with increasing cyclic loading amplitudes (q_{cyc}). However, there are fluctuations in secant stiffness with each tenfold increase in cycle numbers under each cyclic amplitude. Finally, at 27 kPa, the stiffness decreases, with no values at 10^4 cycles. This suggests that the samples might have reached the failure stage before reaching 10^4 cycles. Connect this information with Figure 4.5.

At the lowest cyclic amplitude ($q_{cyc} = 5kPa$), the damping ratio has high values which later decline with increasing cyclic amplitude until ($q_{cyc} = 27kPa$) is reached. It is important to note here that the decline is gentle below cycle numbers (10^3) but as the cycle number exceeds (10^4), an abrupt increase in damping ratio from (0.09 to 0.20) is observed. This is a clear sign that the NC sample has reached the failure stage. Connect this information with Figure 4.3.

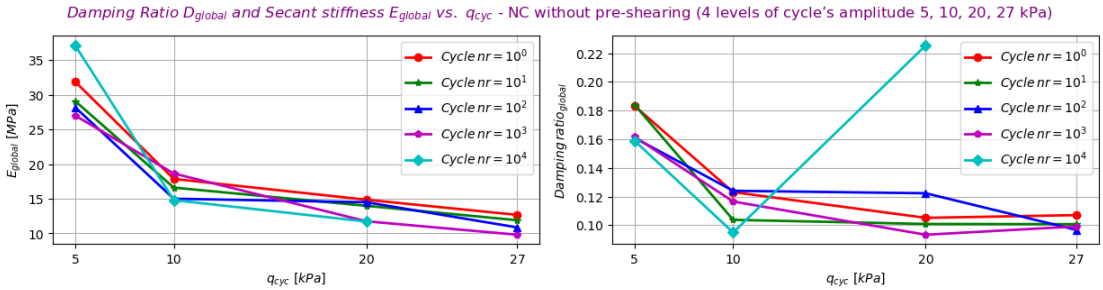

Figure 4.12: *Overview of how undrained global secant stiffness E_{sec} for Natural clay degrades in relation to cyclic loading amplitude q_{cyc} and cycle nr*

5 Conclusions

The thesis project addressed a critical research gap by conducting a comprehensive investigation into the degradation behavior of Swedish lime cement mixed clay (LCC), primarily focusing on the evolution of its dynamic stiffness properties such as damping ratio (D), secant stiffness (E), and shear modulus (G). The utilization of lime cement mixing represents a promising technique for the stabilization of soils, particularly in regions struggling with challenges associated with natural soft clays. The report summarizes the following achievements:

- A Python-based automated pre-processing tool has been successfully implemented to manage GDS raw data with a high volume of cycles. This implementation aims to expedite the calculation of stiffness parameters to facilitate comprehensive stiffness degradation analysis for both LCC and NC samples.
- A thorough investigation of a precise estimation of propagation error originating from the sensors of the triaxial setup has been conducted. The magnitude of the final estimated propagation error related to local stiffness measurement in LCC is high (10.46 %). This is because the relative uncertainties in axial stresses are high (LCC03 = 10.566 %, LCC17 = 10.456 %) compared to low relative uncertainties in local axial strain (0.11%).
- The criteria for future prediction for the cyclic failure for LCC has been taken into consideration in the project based on strain resistance numbers (m_ϵ) associated with each soil type.

The results indicate that the LCC samples have much lower cyclic stress ratios (CSRs) than the NC samples, even when subjected to high cyclic amplitudes and numerous cycles. This suggests that these factors do not significantly affect CSR in LCC samples. In the case of the LCC17 sample, the damping ratio initially increased but then experienced a slight decline, resulting in an overall 20% reduction. This contrasts with the NC samples, which showed a significant increase ($50\% \approx 80\%$). The local secant stiffness in LCC17 increased during the first stage ($1150MPa \approx 1450MPa$) but slightly degraded (1390 MPa) during the second stage under higher cyclic loading. At the same time, the NC samples exhibited a notable decrease in stiffness. Similarly, the local shear modulus in LCC17 showed minor degradation, whereas the NC samples experienced a marked reduction. Overall, the LCC samples demonstrate better stiffness stability under cyclic loading than the NC samples.

The axial loading sensors in the LCC samples had higher uncertainties in axial stresses at around 10.5%, while the NC samples had 0% uncertainty. However, the local strain transducers indicated much lower uncertainties, around 0.11%, for LCC samples and 0.0269% for NC. This discrepancy led to significant uncertainty in local stiffness measurements for the LCC samples, at around 10.46%. This high propagation error resulted in less precise stiffness measurements. Additionally, the strain resistance numbers for LCC samples were notably higher than those for NC samples, both with and without pre-shearing, indicating better strain resistance in LCC samples. Overall, the LCC samples showed good stiffness behavior under cyclic loading, although there were some uncertainties in axial stress measurements.

Although there were limited samples with local transducer cases in this study, the comparison analysis still provided a good indication of the high quality of lime-cement mixed clays (LCC). Both samples are very stiff (LCC3 more stiffer than LCC17). It also supported the thesis hypothesis that adding binder content significantly improves the LCC clay's resistance to cyclic failure.

5.1 Recommendations

The project has identified the following key recommendations that could significantly enhance the robustness of the findings for future research initiatives on similar topics:

- Further high-quality cyclic triaxial testing on LCC samples, particularly with much higher cyclic loading amplitudes (q_{cyc}), is imperative to analyze LCC's stiffness degradation behavior comprehensively. Such tests at high cycle numbers will provide valuable insights into the material's behavior under varying loading conditions.
- An in-depth analysis of a series of mixtures featuring varied curing periods and mixing ratios is essential for understanding the complex interplay among stiffness parameters.
- Minimizing the uncertainty levels associated with global and local sensors in a triaxial setup and the variation of diameters are prerequisites for improving the accuracy of stiffness measurements. This is because these uncertainties, if not managed, can lead to significant error propagation. Future studies should address this concern regarding high propagation error in stiffness.
- Providing comprehensive details concerning the composition of clay (especially for minerals) within the lime-cement mixture for each sample taken at varying depths in the project case would significantly enhance the depth of stiffness analysis for the LCC samples.
- Future studies on cyclic constitutive strain accumulation model (CreepSclay1S model), soil structure interactions model, and modeling with moving train loads with evolving dynamic stiffness properties of LCC can provide in-depth analysis of stiffness degradation.

6 References

Abdellaziz, M., Karray, M., Chekired, M., Delisle, M.-C., Locat, P., Ledoux, C., & Mompin, R. (2021). Shear modulus and hysteretic damping of sensitive eastern Canada clays. *Canadian Geotechnical Journal*, *58*(8), 1118–1134. https://doi.org/10.1139/cgj-2020-0254

Alves Costa, P., Calçada, R., Silva Cardoso, A., & Bodare, A. (2010). Influence of soil non-linearity on the dynamic response of high-speed railway tracks. *Soil Dynamics and Earthquake Engineering*, *30*(4), 221–235. https://doi.org/10.1016/j.soildyn.2009.11.002

Andersen, K. H. (2009). Bearing capacity under cyclic loading — offshore, along the coast, and on land. The 21st Bjerrum Lecture presented in Oslo, 23 November 2007This paper represents the written version of the 21st Bjerrum Lecture. While it has been edited for the present publication, it retains the general structure of the original lecture, which was intended for a general geotechnical audience. The Bjerrum Lecture is presented in Oslo in alternate years by the Norwegian Geotechnical Society with the support of the Bjerrum Memorial Fund (Laurits Bjerrums Minnefond). *Canadian Geotechnical Journal*, *46*(5), 513–535. https://doi.org/10.1139/T09-003

Andersen, K. H., Rosenbrand, W. F., Brown, S. F., & Pool, J. H. (1980). Cyclic and Static Laboratory Tests on Drammen Clay. *Journal of the Geotechnical Engineering Division*, *106*(5), 499–529. https://doi.org/10.1061/AJGEB6.0000957

Anna Wildt, P. (2021). *Summary of "A direction framework for long-term infrastrucutureplanning, for the periods 2022-2033 and 2022-2036"* (tech. rep. No. TRV 2020/73376). Traffikverket. Röda vägen 1, 781 89 Borlänge. https://trafikverket.diva-portal.org/smash/get/diva2:1568062/FULLTEXT01.pdf

Atkinson, J. H. (2000). Non-linear soil stiffness in routine design. *Géotechnique*, *50*(5), 487–508. https://doi.org/10.1680/geot.2000.50.5.487

Bear, J., & Verruijt, A. (2012, December). *Modeling Groundwater Flow and Pollution* [Google-Books-ID: NTHsCAAAQBAJ]. Springer Science & Business Media.

Bharti, R. K., & Dixit, M. (2019). Dynamic Analysis on Multilayer of Cohesionless Soil Subgrade of Railway Track with PLAXIS and MATLAB. In R. Sundaram, J. T. Shahu, & V. Havanagi (Eds.), *Geotechnics for Transportation Infrastructure* (pp. 337–349). Springer. https://doi.org/10.1007/978-981-13-6701-4_21

Bi, G., Guan, Y., Chen, X., Tan, W., Huang, W., Gao, Y., & Wang, M. (2020). Evaluation of Uncertainty in Determining Average Grain Size by ASTM E112 Standard. *IOP Conference Series: Materials Science and Engineering*, *733*(1), 012045. https://doi.org/10.1088/1757-899X/733/1/012045

Birmpilis, G., & Dijkstra, J. (2021). Testing sensitive clays through time and length scales [Publisher: IOP Publishing]. *IOP Conference Series: Earth and Environmental Science*, *710*(1), 012021. https://doi.org/2022020801014900

Bogusz, W., & Godlewski, T. (2019). Geotechnical design of railway embankments – requirements and challenges [Publisher: EDP Sciences]. *MATEC Web of Conferences*, *262*, 11002. https://doi.org/10.1051/matecconf/201926211002

Bozkurt, S., Abed, A., & Karstunen, M. (2023). Finite element analysis for a deep excavation in soft clay supported by lime-cement columns. *Computers and Geotechnics*, *162*, 105687. https://doi.org/10.1016/j.compgeo.2023.105687

Cai, Y., & Wang, J. (2008). Modeling of Stress-Strain Behavior of Soft Clay under Cyclic Loading. In H. Liu, A. Deng, & J. Chu (Eds.), *Geotechnical Engineering for Disaster Mitigation and Rehabilitation* (pp. 277–283). Springer Berlin Heidelberg. https://doi.org/10.1007/978-3-540-79846-0_26

Dastjerdy, B., Saeidi, A., & Heidarzadeh, S. (2023). Review of Applicable Outlier Detection Methods to Treat Geomechanical Data. *Geotechnics*, *3*(2), 375–396. https://doi.org/10.3390/geotechnics3020022

Dijkstra, Tahershamsi, Hossein, & Naghdeh, Reza Ahmadi. (2019, February). *Degradation of a natural sensitive clay under cyclic loading* (Technical report A2019-02 No. 978-91-986927-0-9). Chalmers Tekniska Högskola. Goteborg. https://biggeo.se/wp-content/uploads/2023/01/BIG-Rapport-A2019-02-Nedbrytning.pdf

Esveld, C. (2001). *Modern railway track* (2. ed). MRT-Productions.

Fernández-Ruiz, J., Castanheira-Pinto, A., Costa, P. A., & Connolly, D. P. (2022). Influence of non-linear soil properties on railway critical speed. *Construction and Building Materials*, *335*, 127485. https://doi.org/10.1016/j.conbuildmat.2022.127485

Guler, H., Jovanovic, S., & Evren, G. (2011). Modelling railway track geometry deterioration. *Proceedings of the Institution of Civil Engineers - Transport*, *164*(2), 65–75. https://doi.org/10.1680/tran.2011.164.2.65

Hall, L. (2000, April). *Simulations and analyses of train-induced ground vibrations: A comparative study of two-and three-dimensional calculations with actual measurements.* [Doctoral dissertation].

Hall, L. (2003). Simulations and analyses of train-induced ground vibrations in finite element models. *Soil Dynamics and Earthquake Engineering*, *23*(5), 403–413. https://doi.org/10.1016/S0267-7261(02)00209-9

Idriss, I. M., Dobry, R., & Singh, R. D. (1978). Nonlinear Behavior of Soft Clays during Cyclic Loading. *Journal of the Geotechnical Engineering Division*, *104*(12), 1427–1447. https://doi.org/10.1061/AJGEB6.0000727

Janbu. (1969). The resistance concept applied to deformations of soils. *In Proceedings of 7th International Conference on Soil Mechanics and Foundation Engineering (Mexico)*, 191–196.

Janbu. (1985). Soil models in offshore engineering. *Géotechnique*, *35*(3), 241–281. https://doi.org/10.1680/geot.1985.35.3.241

Kokusho, T. (1980). Cyclic Triaxial Test of Dynamic Soil Properties for Wide Strain Range. *Soils and Foundations*, *20*(2), 45–60. https://doi.org/10.3208/sandf1972.20.2_45

Larsson, S. (2021). The Nordic dry deep mixing method: Best practice and lessons learned, 30 p. Retrieved February 12, 2024, from https://urn.kb.se/resolve?urn=urn:nbn:se:kth:diva-296588

Lazorenko, G., Kasprzhitskii, A., Khakiev, Z., & Yavna, V. (2019). Dynamic behavior and stability of soil foundation in heavy haul railway tracks: A review. *Construction and Building Materials*, *205*, 111–136. https://doi.org/10.1016/j.conbuildmat.2019.01.184

Lee, C.-J., & Sheu, S.-F. (2007). The stiffness degradation and damping ratio evolution of Taipei Silty Clay under cyclic straining. *Soil Dynamics and Earthquake Engineering*, *27*(8), 730–740. https://doi.org/10.1016/j.soildyn.2006.12.008

Lei, H., Liu, J., Liu, M., Zhang, Z., & Jiang, M. (2017). Effects of frequency and cyclic stress ratio on creep behavior of clay under cyclic loading [Publisher: Taylor

& Francis _eprint: https://doi.org/10.1080/1064119X.2016.1157659]. *Marine Georesources & Geotechnology*, *35*(2), 281–291. https://doi.org/10.1080/1064119X.2016.1157659

Likitlersuang, S., Teachavorasinskun, S., Surarak, C., Oh, E., & Balasubramaniam, A. (2013). Small strain stiffness and stiffness degradation curve of Bangkok Clays. *Soils and Foundations*, *53*(4), 498–509. https://doi.org/10.1016/j.sandf.2013.06.003

Liu, B., Kong, L., Sun, Z., & Zhou, Z. (2022). Undrained dynamic response of naturally high-strength sensitive clay to bidirectional cyclic loadings under the plane strain condition. *Soil Dynamics and Earthquake Engineering*, *163*, 107517. https://doi.org/10.1016/j.soildyn.2022.107517

Luca Pirozzolo. (2017). *Simulation of railway infrastructure with asphalt layer for tracks in Sweden* [Doctoral dissertation, Universidad de Granada.]. http://hdl.handle.net/10481/47126

Lundström, K., & Dehlbom, B. (2019). Soil property changes below existing embankments. *Proceedings of the XVII European Conference on Soil Mechanics and Geotechnical Engineering*, (Geotechnical Engineering, foundation of the future), 786–793. https://doi.org/10.32075/17ECSMGE-2019-0149

Massobrio, M., & Mora, R. (Eds.). (2021). *Hexapod External Fixator Systems: Principles and Current Practice in Orthopaedic Surgery*. Springer International Publishing. https://doi.org/10.1007/978-3-030-40667-7

Matasovic, N., & Vucetic, M. (1992). A Pore Pressure Model for Cyclic Straining of Clay. *Soils and Foundations*, *32*(3), 156–173. https://doi.org/10.3208/sandf1972.32.3_156

Nagaraj, T., & Miura, N. (2001, January). *Soft Clay Behaviour Analysis and Assessment* (0th ed.). CRC Press. https://doi.org/10.1201/9780367800345

Narasimha Rao, S., & Panda, A. (1998). Non-linear analysis of undrained cyclic strength of soft marine clay. *Ocean Engineering*, *26*(3), 241–253. https://doi.org/10.1016/S0029-8018(97)10028-2

Nielsen, J. C., & Li, X. (2018). Railway track geometry degradation due to differential settlement of ballast/subgrade – Numerical prediction by an iterative procedure. *Journal of Sound and Vibration*, *412*, 441–456. https://doi.org/10.1016/j.jsv.2017.10.005

Okur, D., & Ansal, A. (2007). Stiffness degradation of natural fine grained soils during cyclic loading. *Soil Dynamics and Earthquake Engineering*, *27*(9), 843–854. https://doi.org/10.1016/j.soildyn.2007.01.005

Paniagua, P., Bache, B. K., Karlsrud, K., & Lund, A. K. (2022). Strength and stiffness of laboratory-mixed specimens of stabilised Norwegian clays. *Proceedings of the Institution of Civil Engineers - Ground Improvement*, *175*(2), 150–163. https://doi.org/10.1680/jgrim.19.00051

Peck, R. B. (1969). Advantages and Limitations of the Observational Method in Applied Soil Mechanics. *Géotechnique*, *19*(2), 171–187. https://doi.org/10.1680/geot.1969.19.2.171

Prevost, J.-H., & Hoeg, K. (1975). Effective Stress-Strain-Strength Model for Soils. *Journal of the Geotechnical Engineering Division*, *101*(3), 259–278. https://doi.org/10.1061/AJGEB6.0000154

Randolph, M., & Gourvenec, S. (2017, July). *Offshore Geotechnical Engineering* [Google-Books-ID: HjoPEAAAQBAJ]. CRC Press. https://books.google.se/books?hl=

en&lr=&id=HjoPEAAAQBAJ&oi=fnd&pg=PP1&dq=Randolph,+M.+and+Gourvenec,+S.+(2017).+Offshore+geotechnical+engineering.&ots=FzJlk-ABtK&sig=Ti2bugIethMyg-cDdaF19kjocPM&redir_esc=y#v=onepage&q=Randolph%2C%20M.%20and%20Gourvenec%2C%20S.%20(2017).%20Offshore%20geotechnical%20engineering.&f=false

Riyad, A. S. M., Ferreira, F. B., Indraratna, B., & Ngo, T. (2021). A Critical Review on the Performance of Pile-Supported Rail Embankments under Cyclic Loading: Numerical Modeling Approach [Number: 5 Publisher: Multidisciplinary Digital Publishing Institute]. *Sustainability*, *13*(5), 2509. https://doi.org/10.3390/su13052509

Roshan, M. J., A Rashid, A. S., Abdul Wahab, N., Tamassoki, S., Jusoh, S. N., Hezmi, M. A., Nik Daud, N. N., Mohd Apandi, N., & Azmi, M. (2022). Improved methods to prevent railway embankment failure and subgrade degradation: A review. *Transportation Geotechnics*, *37*, 100834. https://doi.org/10.1016/j.trgeo.2022.100834

Selig, E. T., & Li, D. (1994). TRACK MODULUS: ITS MEANING AND FACTORS INFLUENCING IT [ISBN: 9780309061018]. *Transportation Research Record*, (1470). Retrieved January 31, 2024, from https://trid.trb.org/View/425388

Sharma, S. S., & Fahey, M. (2003). Degradation of Stiffness of Cemented Calcareous Soil in Cyclic Triaxial Tests. *Journal of Geotechnical and Geoenvironmental Engineering*, *129*(7), 619–629. https://doi.org/10.1061/(ASCE)1090-0241(2003)129:7(619)

Shih, J., Thompson, D., & Zervos, A. (2017). The influence of soil nonlinear properties on the track/ground vibration induced by trains running on soft ground. *Transportation Geotechnics*, *11*, 1–16. https://doi.org/10.1016/j.trgeo.2017.03.001

Staubach, P., Machaček, J., Tafili, M., & Wichtmann, T. (2022). A high-cycle accumulation model for clay and its application to monopile foundations. *Acta Geotechnica*, *17*(3), 677–698. https://doi.org/10.1007/s11440-021-01446-9

Subramaniam, P., & Banerjee, S. (2014). Factors affecting shear modulus degradation of cement treated clay. *Soil Dynamics and Earthquake Engineering*, *65*, 181–188. https://doi.org/10.1016/j.soildyn.2014.06.013

Suiker, A. S. J., & De Borst, R. (2003). A numerical model for the cyclic deterioration of railway tracks. *International Journal for Numerical Methods in Engineering*, *57*(4), 441–470. https://doi.org/10.1002/nme.683

Tahershamsi, H. (2023). *On Cyclic Accumulation Models for Degradation of Railway Foundations* [Ph.D.]. Chalmers Tekniska Hogskola (Sweden) [ISBN: 9798379653064].

Tahershamsi, H., Ahmadi Naghadeh, R., Zuada Coelho, B., & Dijkstra, J. (2023). Low amplitude strain accumulation model for natural soft clays below railways. *Transportation Geotechnics*, *42*, 101011. https://doi.org/10.1016/j.trgeo.2023.101011

Tang, W. H., Yucemen, M. S., & Ang, A. H.-S. (1976). Probability-based short term design of soil slopes. *Canadian Geotechnical Journal*, *13*(3), 201–215. https://doi.org/10.1139/t76-024

Teachavorasinskun, S., Thongchim, P., & Lukkunaprasit, P. (2002). Stress rate effect on the stiffness of a soft clay from cyclic, compression and extension triaxial tests. *Géotechnique*, *52*(1), 51–54. https://doi.org/10.1680/geot.2002.52.1.51

Tornborg, J., Karlsson, M., Kullingsjö, A., & Karstunen, M. (2021). Modelling the construction and long-term response of Göta Tunnel. *Computers and Geotechnics*, *134*, 104027. https://doi.org/10.1016/j.compgeo.2021.104027

Trafikverket. (2021, December). Improved Capacity [Last Modified: 12/2/2021 12:55:22 PM Publisher: trafikverket@trafikverket.se]. Retrieved June 12, 2024, from https://bransch.trafikverket.se/en/startpage/operations/Operations-railway/improved-capacity/

Vardanega, P. J., & Bolton, M. D. (2013). Stiffness of Clays and Silts: Normalizing Shear Modulus and Shear Strain. *Journal of Geotechnical and Geoenvironmental Engineering*, *139*(9), 1575–1589. https://doi.org/10.1061/(ASCE)GT.1943-5606.0000887

Vucetic, M., & Dobry, R. (1991). Effect of Soil Plasticity on Cyclic Response. *American Society of Civil Engineers*, *117*, 89–107. https://doi.org/10.1061/(ASCE)0733-9410(1991)117:1(89)

Wang, D. X., Abriak, N. E., Zentar, R., & Xu, W. (2012). Solidification/stabilization of dredged marine sediments for road construction. *Environmental Technology*, *33*(1), 95–101. https://doi.org/10.1080/09593330.2011.551840

Wang, D., & Korkiala-Tanttu, L. (2020). 1-D compressibility behaviour of cement-lime stabilized soft clays. *European Journal of Environmental and Civil Engineering*, *24*(7), 1013–1031. https://doi.org/10.1080/19648189.2018.1440633

Wang, J., Guo, L., Cai, Y., Xu, C., & Gu, C. (2013). Strain and pore pressure development on soft marine clay in triaxial tests with a large number of cycles. *Ocean Engineering*, *74*, 125–132. https://doi.org/10.1016/j.oceaneng.2013.10.005

Wang, M., Kong, L., Zhao, C., & Zang, M. (2012). Dynamic characteristics of lime-treated expansive soil under cyclic loading. *Journal of Rock Mechanics and Geotechnical Engineering*, *4*(4), 352–359. https://doi.org/10.3724/SP.J.1235.2012.00352

Wong, D. Y.-C., Sadasivan, V., Isaksson, J., Karlsson, A., & Dijkstra, J. (2023, October). Trans-Scale Spatial Variability of Lime-Cement Mixed Clay. https://doi.org/10.2139/ssrn.4600941

Wood, T. (2016). *On the Small Strain Stiffness of Some Scandinavian Clays and Impact on Deep Excavation* [Ph.D.]. Chalmers Tekniska Hogskola (Sweden) [ISBN: 9781392555095]. Retrieved January 26, 2024, from https://www.proquest.com/docview/2402396933/abstract/2B3CEA72FBF04E87PQ/1

Wood, T., & Karstunen, M. (2022). Modelling the creep of deep foundations in soft Gothenburg clays. *European Journal of Environmental and Civil Engineering*, *26*(7), 2581–2599. https://doi.org/10.1080/19648189.2017.1344146

Woodward, P., Laghrouche, O., Mezher, S., & Connolly, D. (2015). Application of Coupled Train-Track Modelling of Critical Speeds for High-Speed Trains using Three-Dimensional Non-Linear Finite Elements. *International Journal of Railway Technology*, *4*(3), 1–35. https://doi.org/10.4203/ijrt.4.3.1

Wu, T., Han, J., Cai, Y., Guo, L., & Wang, J. (2021). Relationship between monotonic and cyclic behavior of saturated soft clay in undrained triaxial compression tests. *Canadian Geotechnical Journal*, *58*(12), 1812–1824. https://doi.org/10.1139/cgj-2019-0356

Yang, L., & Woods, R. D. (2015). Shear stiffness modeling of cemented clay. *Canadian Geotechnical Journal*, *52*(2), 156–166. https://doi.org/10.1139/cgj-2012-0377

Yu, H.-j., & Liu, E.-l. (2020). Cyclic Properties of Artificially Cemented Gravel-Silty Clay Mixed Soils. *Experimental Techniques*, *44*(5), 573–589. https://doi.org/10.1007/s40799-020-00376-7

Zhang, J., Dias, D., & Jenck, O. (2023). 3D numerical modeling of a rigid inclusion reinforced railway embankment under cyclic loading. *Transportation Geotechnics*, *41*, 101003. https://doi.org/10.1016/j.trgeo.2023.101003

Zhu, Z., Zhang, C., Wang, J., Zhang, P., & Zhu, D. (2021). Cyclic Loading Test for the Small-Strain Shear Modulus of Saturated Soft Clay and Its Failure Mechanism [Publisher: Hindawi]. *Geofluids*, *2021*, e2083682. https://doi.org/10.1155/2021/2083682

Zuada Coelho, B., Dijkstra, J., & Karstunen, M. (2021). Viscoplastic cyclic degradation model for soft natural soils. *Computers and Geotechnics*, *135*, 104176. https://doi.org/10.1016/j.compgeo.2021.104176

Appendix A

A.1 Loading stage

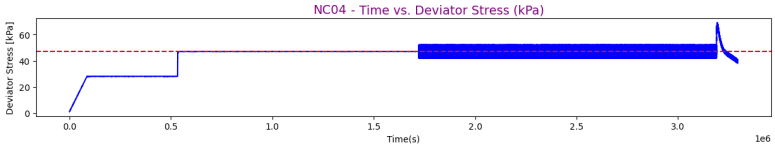

(a) NC04

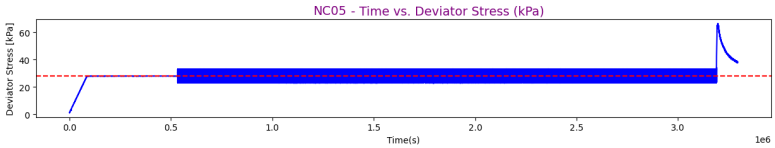

(b) NC05

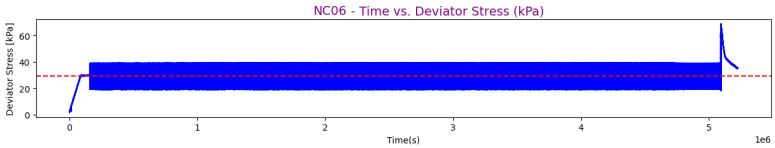

(c) NC06

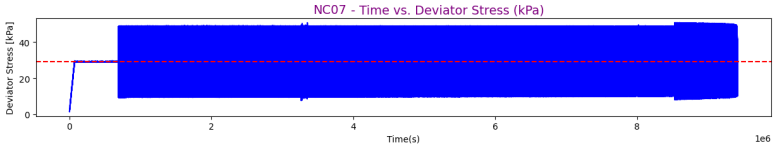

(d) NC07

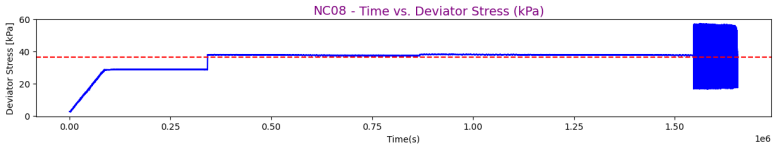

(e) NC08

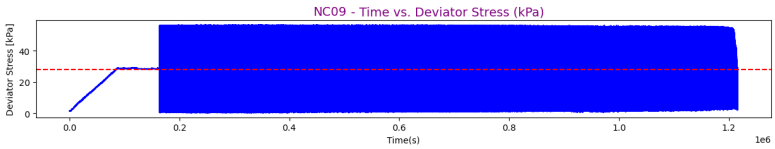

(f) NC09

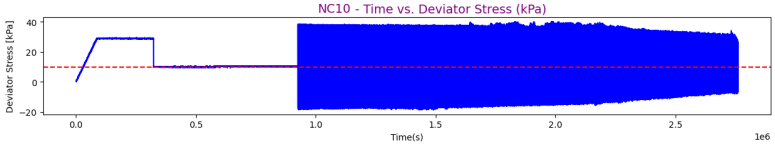

(g) NC10

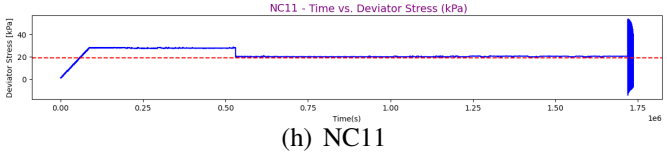

(h) NC11

Figure .1: Loading stages under cyclic triaxial test for NC samples

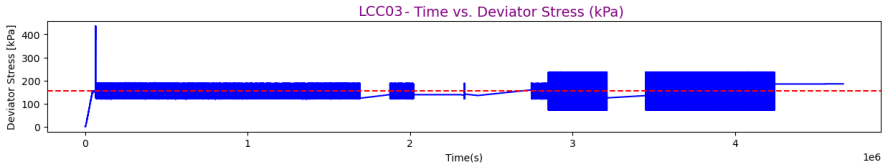

(a) LCC03

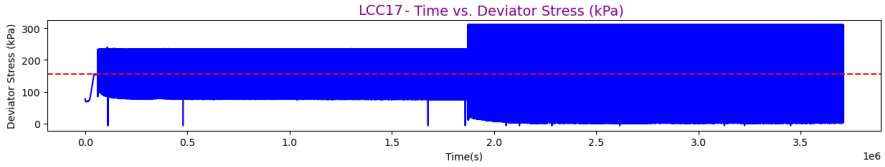

(b) LCC17

Figure .2: Loading stages under cyclic triaxial test for LCC samples

A.2 Ellipse fitted to each sample

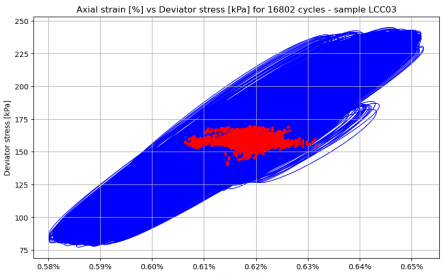

(a) LCC03 Global

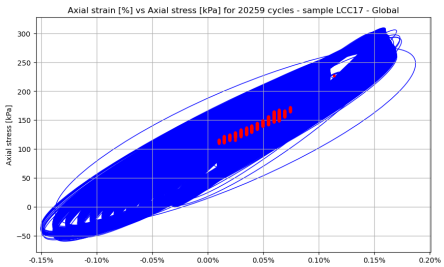

(b) LCC17 Global

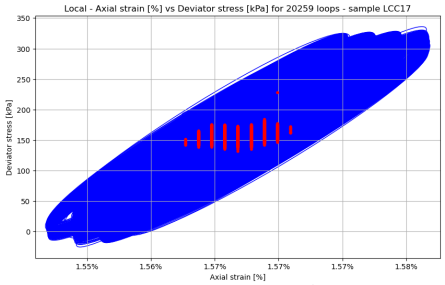

(c) LCC17 Local

Figure .3: All identified ellipse includes centers for each LCC sample

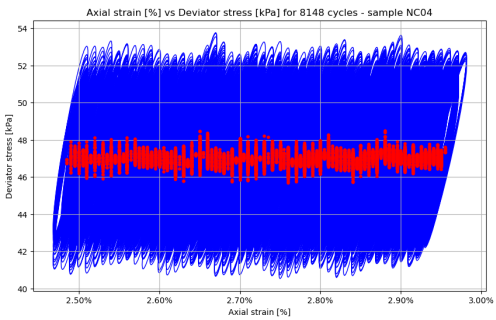

(a) NC04

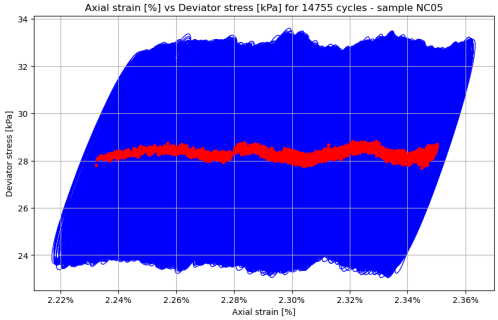

(b) NC05

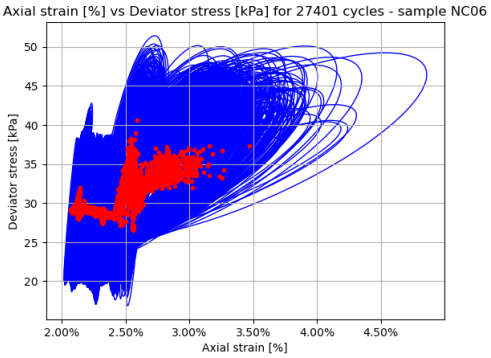

(c) NC06

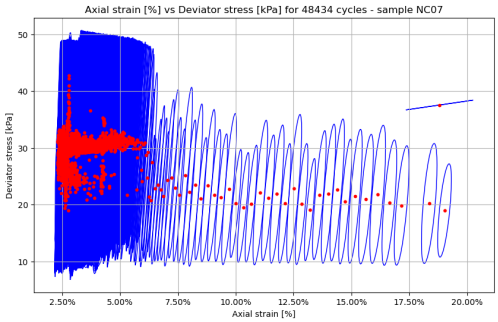

(d) NC07

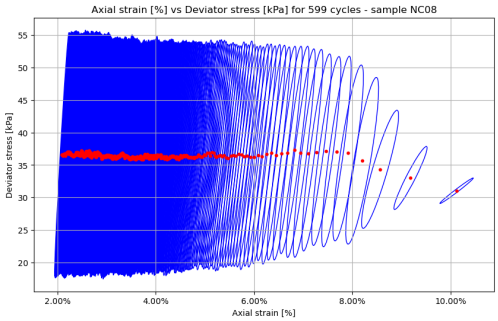

(e) NC08

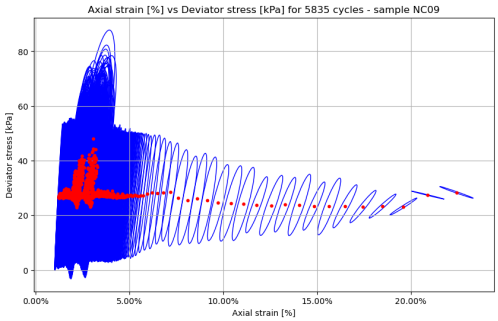

(f) NC09

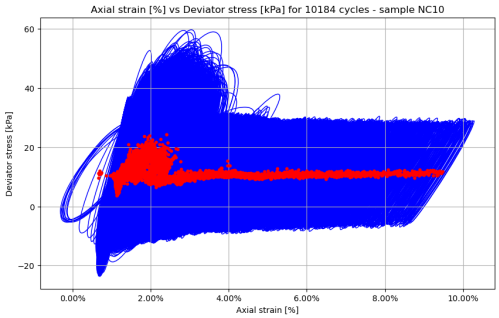

(g) NC10

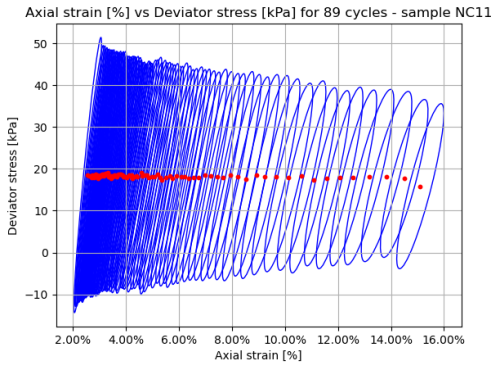

(h) NC11

Figure .4: All identified ellipse includes centers for each NC sample

A.3 Strain resistance number for samples

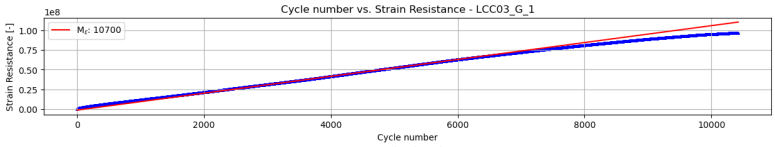

(a) LCC03 Global Stage 1

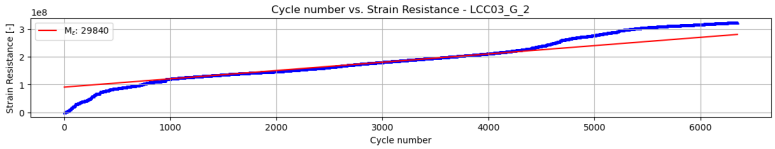

(b) LCC03 Global Stage 2

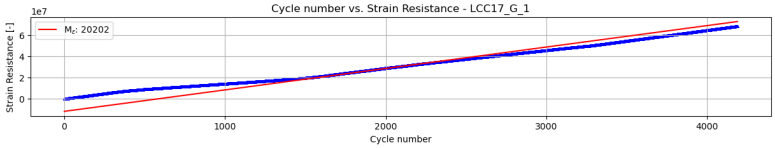

(c) LCC17 Global Stage 1

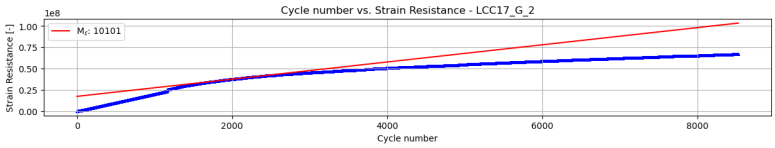

(d) LCC17 Global Stage 2

Figure .5: Strain resistance and M_ε for each LCC global sample

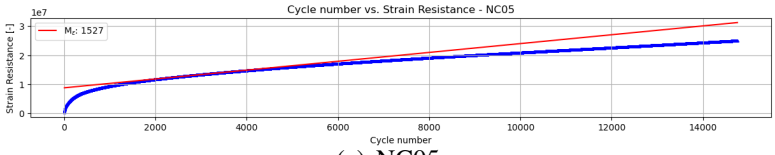

(a) NC05

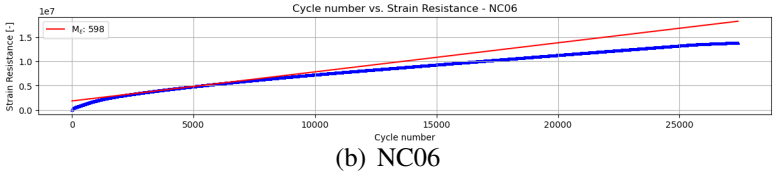

(b) NC06

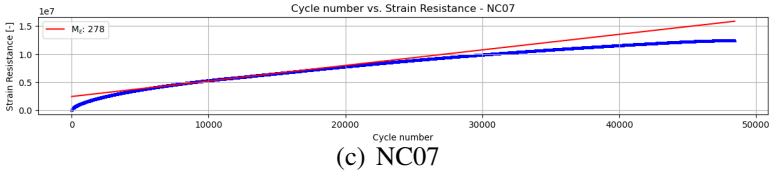

(c) NC07

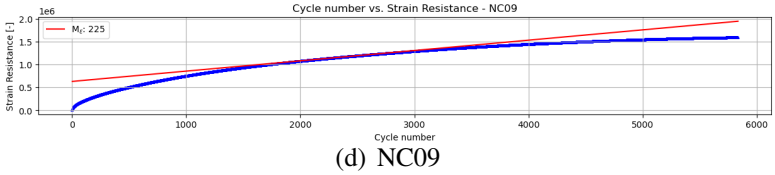

(d) NC09

Figure .6: Strain resistance and M_ε for each NC sample without pre-sharing stage

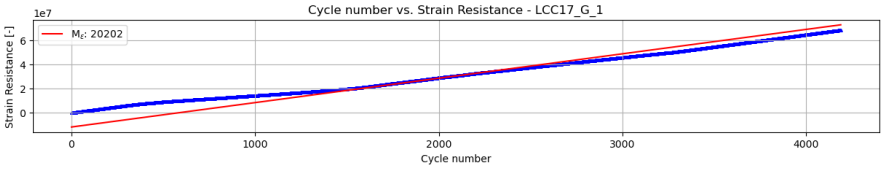

(a) LCC17 Local Stage 1

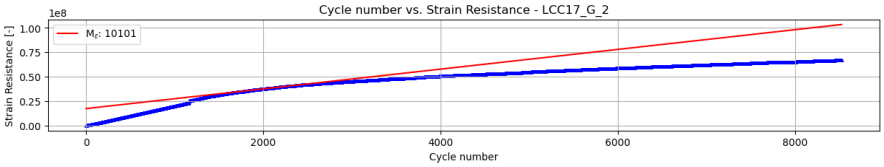

(b) LCC17 Local Stage 2

Figure .7: Strain resistance and M_ε for each LCC local sample

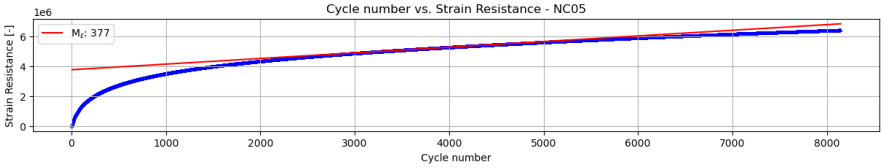

(a) NC04

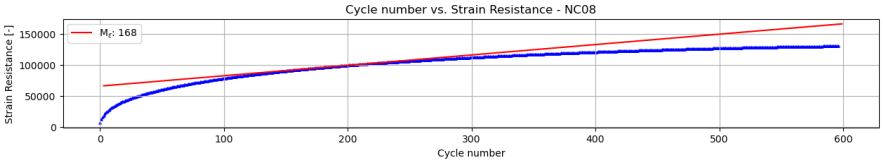

(b) NC08

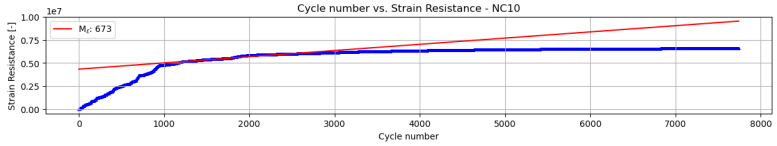

(c) NC10

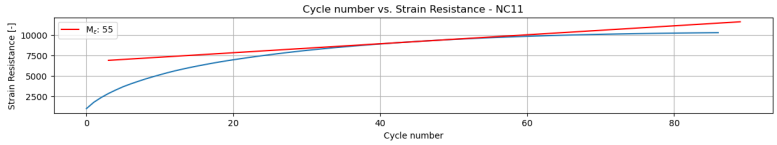

(d) NC11

Figure .8: Strain resistance and M_ε for each NC sample with pre-sharing stage

A.4 Shear modulus ratio

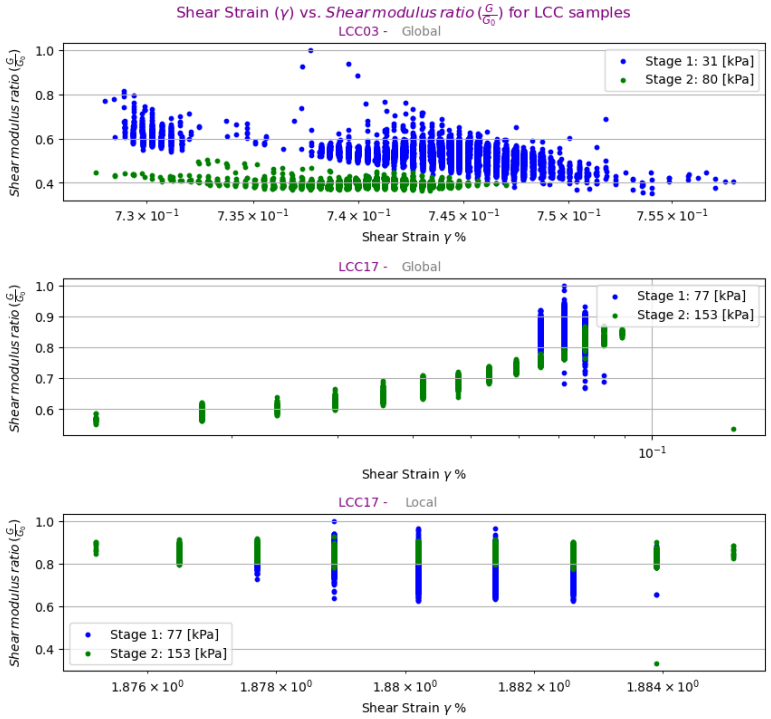

Figure .9: *Shear modulus ratio* $\frac{G}{G_0}$ *for LCC samples*

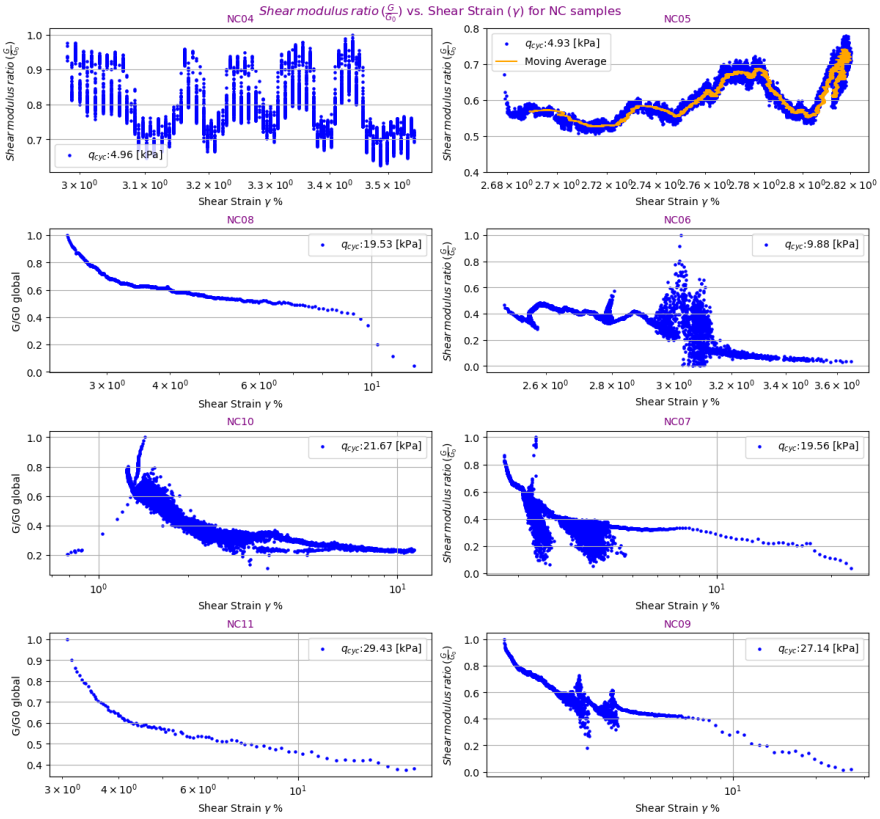

Figure .10: *Shear modulus ratio* $\frac{G}{G_0}$ *for NC*

Appendix B

B.1 Information of loading stages

Table .1: The comprehensive information for each phase of the studied samples

qavg	qcyc	qcyc/p0	CSR	qcyc/2Su	qm/2Su	Cyclic failure
[kPa]	[kPa]	-	-	-	-	-
154.45+/-0.11	31.11+/-0.30	0.109+/-0.006	0.00794+/-0.00008	0.01589+/-0.00015	0.080+/-0.022	No
154.12+/-0.09	80.3+/-0.4	0.282+/-0.014	0.02051+/-0.00010	0.04102+/-0.00020	0.080+/-0.022	No
155.60+/-0.10	77.41+/-0.31	0.250+/-0.011	0.01976+/-0.00008	0.03953+/-0.00016	0.079+/-0.022	No
154.72+/-0.08	152.57+/-0.35	0.493+/-0.023	0.03895+/-0.00009	0.07791+/-0.00018	0.079+/-0.022	No
47.0135+/-0.0017	4.964+/-0.008	0.0922+/-0.0013	0.03761+/-0.00006	0.07521+/-0.00013	0.712+/-0.016	No
28.0671+/-0.0012	4.929+/-0.006	0.0995+/-0.0015	0.03734+/-0.00005	0.07469+/-0.00009	0.425+/-0.016	No
28.9950+/-0.0009	9.884+/-0.005	0.1936+/-0.0029	0.074880+/-0.000034	0.14976+/-0.00007	0.451+/-0.016	No
29.0224+/-0.0012	19.558+/-0.006	0.351+/-0.005	0.14817+/-0.00005	0.29634+/-0.00009	0.441+/-0.016	No
36.643+/-0.005	19.527+/-0.031	0.367+/-0.005	0.14794+/-0.00023	0.2959+/-0.0005	0.572+/-0.016	Yes
28.1232+/-0.0015	27.141+/-0.010	0.516+/-0.008	0.20562+/-0.00007	0.41123+/-0.00015	0.429+/-0.016	Yes
9.450+/-0.005	21.669+/-0.031	0.414+/-0.006	0.16416+/-0.00024	0.3283+/-0.0005	0.156+/-0.016	Yes
19.157+/-0.012	29.43+/-0.08	0.595+/-0.009	0.2230+/-0.0006	0.4459+/-0.0012	0.309+/-0.016	Yes

Cyclic loading duration	**Cycles nr**	**Cycle period**	**Frequency**	**p0**	**q0**	**qp**	**qmin**	**qmax**
[days]	**-**	**[s]**	**[Hz]**	**[kPa]**	**[kPa]**	**[kPa]**	**[kPa]**	**[kPa]**
32,24	10420	179,63	0,00557	285.2+/-1.4	156.9+/-2.2		123.4+/-0.4	185.7+/-0.5
21,01	6383	179,69	0,00557	285.2+/-1.4	156.9+/-2.2		73.8+/-0.4	234.4+/-0.7
20,97	10064	180,09	0,00555	309.8+/-1.4	155.0+/-2.2		78.28+/-0.29	233.1+/-0.6
21,24	10196	180,00	0,00556	309.8+/-1.4	155.0+/-2.2		4.82+/-0.16	310.0+/-0.7
16,98	8148	180,01	0,00556	53.8+/-0.8	28.0+/-1.1	19.0+/-1.5	42.050+/-0.012	51.978+/-0.012
30,74	14755	180,03	0,00555	49.5+/-0.8	28.0+/-1.1		23.196+/-0.009	33.055+/-0.009
57,09	27401	180,00	0,00556	51.1+/-0.8	29.7+/-1.1		19.135+/-0.006	38.903+/-0.006
100,97	48438	180,04	0,00555	55.7+/-0.8	29.1+/-1.1		9.841+/-0.008	48.958+/-0.008
1,26	599	180,02	0,00556	53.2+/-0.8	28.6+/-1.1	9.2+/-1.5	17.22+/-0.04	56.27+/-0.04
12,18	5835	180,01	0,00556	52.6+/-0.8	28.3+/-1.1		1.358+/-0.014	55.641+/-0.014
21,22	10184	180,01	0,00556	52.4+/-0.8	28.7+/-1.1	-18.4+/-1.5	-10.43+/-0.04	32.91+/-0.04
0,19	89	180,24	0,00555	49.5+/-0.8	27.9+/-1.1	-7.5+/-1.5	-9.37+/-0.11	49.50+/-0.11

Sample type	Stage Number	Loading Stages	Start index	End index	Rows nr	Star time	End time	Test duration
-	-	-	-	-	-	[s]	[s]	[days]
LCC03	1	I, J, M	1103	166709	165607	65614	2850879	54,01
LCC03	2	I, J, M	166710	415166	248457	2850886	4666569	54,01
LCC17	1	I, J, M	1026	216770	215745	61498	1872958	42,92
LCC17	2	I, J, M	216771	603730	386960	1872964	3708268	42,92
NC04	1	I, J, K, L, M, N	28885	439870	410986	1722356	3189337	38,12
NC05	1	I, J, M, N	8883	744042	735160	532920	3189195	38,12
NC06	1	I, J, M, N	15851	1412213	1396363	158580	5091023	60,48
NC07	1	I, J, M	11554	2400346	2388793	693322	9417181	108,99
NC08	1	I, J, K, L, M	25799	80311	54513	1546320	1655516	19,16
NC09	1	I, J, M	2733	528093	525361	163918	1215882	14,07
NC10	1	I, J, K, L, M	306457	1214271	907815	925578	2760393	31,95
NC11	1	I, J, K, L, M	28779	36874	8096	1719594	1735837	20,09

I = anisotropic consolidation, J = saturation, K = pre-shearing, L = creep, M = cyclic loading, N = post-cyclic
(Tahershamsi, 2023)

B.2 Sensor Calibration data

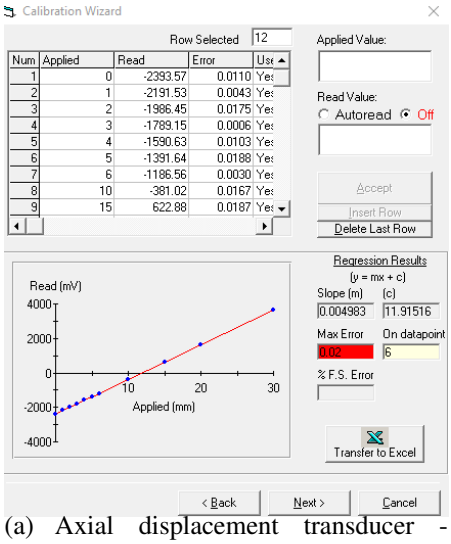

(a) Axial displacement transducer - global

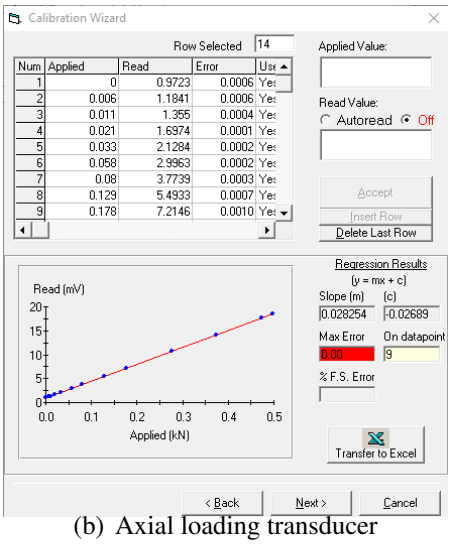

(b) Axial loading transducer

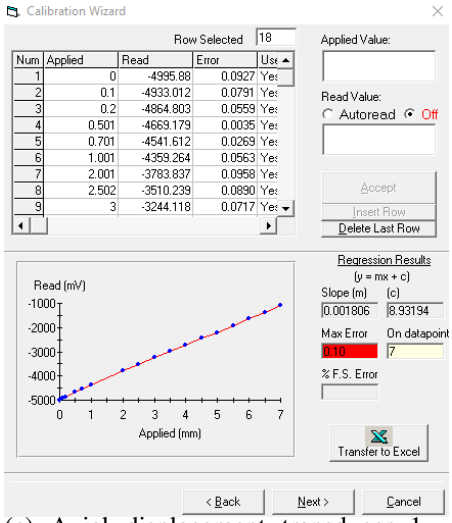

(c) Axial displacement transducer 1 - global

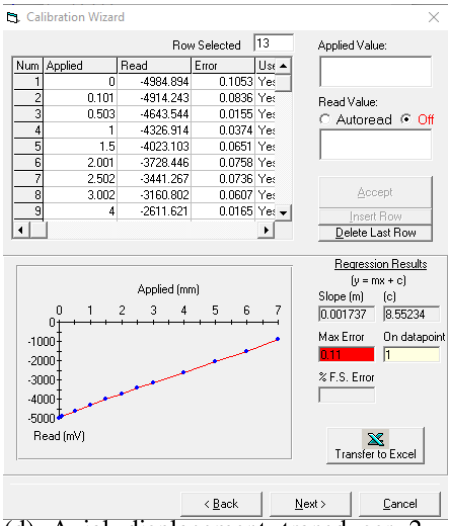

(d) Axial displacement transducer 2 - global

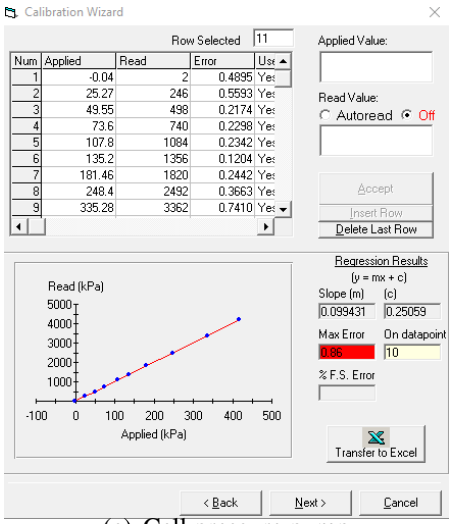

(e) Cell pressure pump

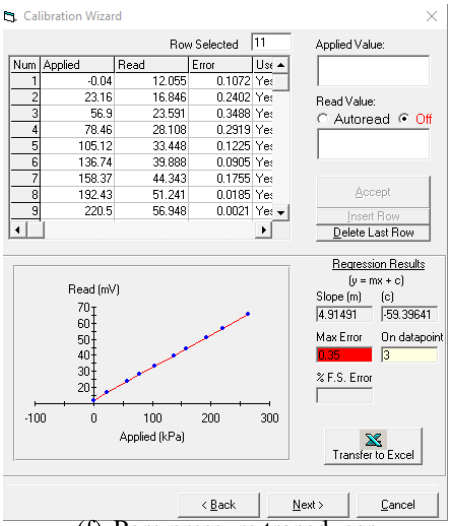

(f) Pore pressure transducer

Figure .11: The uncertainties obtained from Chalmers Laboratory for different sensors used

Appendix C

C.1 Python-Code

C.1.1 Python Libraries Imported

```
""" Libraries and reading gds files """

import pandas as pd
import numpy as np
import os
import matplotlib.pyplot as plt
from scipy import interpolate
from scipy import stats
import matplotlib.patches as patches
from matplotlib.patches import Polygon
from matplotlib.patches import Ellipse
from matplotlib.ticker import PercentFormatter, MultipleLocator,
   FuncFormatter
import math
from skimage.measure import ransac
import uncertainties
from uncertainties import unumpy as unp
from uncertainties import ufloat
from skimage.measure import EllipseModel
import ipywidgets as widgets
import seaborn as sns
import mplcursors as mpc
import mpld3
from shapely.geometry import Polygon
from uncertainties import ufloat_fromstr
from matplotlib.transforms import BlendedGenericTransform
from sklearn.linear_model import LinearRegression
from sklearn.linear_model import RANSACRegressor
```

C.1.2 Python Functions Created

```

""" Function to calculate the centroid and area of the """
polygon for data of cycles
def calculate_centroid(x_values, y_values):
    A = abs( 0.5 * np.abs(np.dot(x_values, np.roll(y_values, 1)) - np
   .dot(y_values, np.roll(x_values, 1))))
    C_x = np.sum((x_values + np.roll(x_values, 1)) * (x_values * np.
   roll(y_values, 1) - np.roll(x_values, 1) * y_values)) / (6 * A)
    C_y = np.sum((y_values + np.roll(y_values, 1)) * (x_values * np.
   roll(y_values, 1) - np.roll(x_values, 1) * y_values)) / (6 * A)
    return C_x, C_y, A


""" define the function for area and volume of the samples."""

def A(D):
    return (np.pi * (D/1000) ** 2) / 4
def V(A, H):
    return (A*(H/1000))

```

```
""" define the function for Relative Uncertainty from the values with uncertainty (ufloat)"""

def ur(data):
    return (unp.std_devs(data)/unp.nominal_values(data)) * 100

""" Calculates the uncertainty mean and uncertainty for a list of ufloats."""

def umean(data):
    nominal_values = unp.nominal_values(data)
    std_deviations = unp.std_devs(data)
    mean_value = np.mean(nominal_values)
    uncertainty = (np.sqrt(np.sum(np.square(std_deviations)))/len(data))
    return (ufloat(mean_value, uncertainty))

""" Function to calculate  variables at each stage of cyclic loading in the samples """
def calculate_stage_info_base(df, cycles_data, name, P0q0_stage_nr, qm_stage_nr, qf, Su):
    # Perform the initial aggregation
    stage_info = df.groupby('Stage Number').agg({
        'Time since start of test (s)': ('min', 'max'),
        'index': ('first', 'last', 'count'),
        'Cycle nr': 'nunique',
        'Cycle time': 'mean'
    }).reset_index()

    # Rename columns
    stage_info.columns = ['Stage Number', 'Start time', 'End time', 'Start index', 'End index', 'Rows nr', 'Cycles nr', 'Cycle period (s)']

    # Adding more columns:
    stage_info['Frequency(Hz)'] = 1 / stage_info['Cycle period (s)']
    stage_info['Sample type'] = name
    stage_info['Test duration(d)'] = (stage_info['End time'] - stage_info['Start time']) / (3600 * 24)

    stage_info['Cyclic loading duration(d)'] = stage_info.apply(lambda row: (row['End time'] - row['Start time']) / (3600 * 24) if row['Cycles nr'] != 0 else 0, axis=1)

    ## Calculate 'p_0', 'q_0', 'qm' at 'start_index' row of different stage nr due to there is presharing
    stage_info['q_0'] = stage_info.apply(lambda row: df.loc[row['Start index'], 'Deviator Stress & Uncertainty (kPa)'] if row['Stage Number'] == P0q0_stage_nr else 0, axis=1)
    stage_info['p_0'] = stage_info.apply(lambda row: df.loc[row['Start index'], 'Eff. Stress & Uncertainty (kPa)'] if row['Stage Number'] == P0q0_stage_nr else 0, axis=1)
    stage_info['q_m'] = stage_info.apply(lambda row: df.loc[row['Start index'], 'Deviator Stress & Uncertainty (kPa)'] if row['Stage Number'] == qm_stage_nr else 0, axis=1)

    mask = (stage_info['Cycles nr'] != 0)
    mask2 = np.where((stage_info['q_0'] != 0) | (stage_info['Cycles
```

```
    nr'] != 0) , True, False)
59
60      stage_info.loc[mask2, 'q_m'] = stage_info.loc[stage_info['Stage
    Number'] == qm_stage_nr, 'q_m'].values[0]
61      stage_info.loc[mask, 'p_0'] = stage_info.loc[stage_info['Stage
    Number'] == P0q0_stage_nr, 'p_0'].values[0]
62      stage_info.loc[mask, 'q_0'] = stage_info.loc[stage_info['Stage
    Number'] == P0q0_stage_nr, 'q_0'].values[0]
63
64      stage_info['q_p'] = stage_info['q_m'] - stage_info['q_0']
65
66
67      stage_info['Cycles_accumulated'] = (stage_info['Cycles nr'] - 1).
    cumsum()
68
69      q_max_values = []
70      q_min_values = []
71      q_avg_values = []
72      # Iterate over the DataFrame rows using iterrows()
73      for index, row in stage_info.iterrows():
74          if row['Cycles nr'] == 0:
75              q_max = 0
76              q_min = 0
77              q_avg = 0
78          else:
79              if index == 0:
80                  range_start = 0
81              else:
82                  range_start = stage_info.loc[index - 1, '
    Cycles_accumulated']
83                  range_end = row['Cycles_accumulated']
84
85              q_max = [np.max(cycles_data[i]['Deviator Stress &
    Uncertainty (kPa)']) for i in range(range_start, range_end)]
86              q_min = [np.min(cycles_data[i]['Deviator Stress &
    Uncertainty (kPa)']) for i in range(range_start, range_end)]
87              q_avg = [umean(cycles_data[i]['Deviator Stress &
    Uncertainty (kPa)']) for i in range(range_start, range_end)]
88              q_max = umean(q_max)
89              q_min = umean(q_min)
90              q_avg = umean(q_avg)
91          q_max_values.append(q_max)
92          q_min_values.append(q_min)
93          q_avg_values.append(q_avg)
94
95      stage_info['q_max'] = q_max_values
96      stage_info['q_min'] = q_min_values
97      stage_info['q_avg'] = q_avg_values
98      stage_info['qcyc'] = (stage_info['q_max'] - stage_info['q_min'])
    / 2
99
100
101     stage_info['qcyc/p0'] = stage_info.apply(lambda row: row['qcyc']
    / row['p_0'] if row['p_0'] != 0 else 0, axis=1)
102     stage_info['CSR'] = stage_info.apply(lambda row: row['qcyc'] / (2
     * qf) if row['qcyc'] != 0 else 0, axis=1)
103     stage_info['qc/2Su'] = stage_info.apply(lambda row: row['qcyc'] /
     (2 * Su) if row['qcyc'] != 0 else 0, axis=1)
```

```
    stage_info['qm/2Su'] = stage_info.apply(lambda row: row['q_m'] / (2 * Su) if row['q_m'] != 0 else 0, axis=1)

    stage_info = stage_info[['Sample type', 'Stage Number', 'Start index', 'End index', 'Rows nr', 'Start time', 'End time', 'Test duration(d)', 'Cyclic loading duration(d)', 'Cycles nr', 'Cycle period (s)', 'Frequency(Hz)', 'p_0', 'q_0', 'q_p', 'q_m', 'q_min', 'q_max', 'q_avg', 'qcyc', 'qcyc/p0', 'CSR','qc/2Su','qm/2Su']]
    #total_df = pd.DataFrame([total_info])  # Create a DataFrame for total info
    stage_info = pd.concat([stage_info], ignore_index=True)  # Concatenate without resetting index
    return stage_info

def calculate_stage_info_all(df, cycles_data, name, P0q0_stage_nr, qm_stage_nr, qf, Su):
    stage_info_all = calculate_stage_info_base(df, cycles_data, name, P0q0_stage_nr, qm_stage_nr, qf, Su)
    # Concatenate without resetting index
    stage_info_all = pd.concat([stage_info_all], ignore_index=True)

    return stage_info_all


def calculate_total_info(stage_info, name, line_ranges):
    total_infos = []  # List to store results for each line number
    for line_number, (start_stage, end_stage) in enumerate(line_ranges, start=1):
        mask_after_stage = (stage_info['Stage Number'] >= start_stage) & (stage_info['Stage Number'] <= end_stage)
        filtered_data_Cycleperiod = stage_info.loc[mask_after_stage, 'Cycle period (s)'].dropna()
        filtered_data_Frequency = stage_info.loc[mask_after_stage, 'Frequency(Hz)'].dropna()
        filtered_data_p_0 = stage_info.loc[mask_after_stage, 'p_0'].dropna()
        filtered_data_q_0 = stage_info.loc[mask_after_stage, 'q_0'].dropna()
        filtered_data_q_m = stage_info.loc[mask_after_stage, 'q_m'].dropna()
        filtered_data_q_p = stage_info.loc[mask_after_stage, 'q_p'].dropna()
        filtered_data_q_min = stage_info.loc[mask_after_stage, 'q_min'].dropna()
        filtered_data_q_max = stage_info.loc[mask_after_stage, 'q_max'].dropna()
        filtered_data_q_avg = stage_info.loc[mask_after_stage, 'q_avg'].dropna()
        filtered_data_qcyc = stage_info.loc[mask_after_stage, 'qcyc'].dropna()
        filtered_data_qcyc_p0 = stage_info.loc[mask_after_stage, 'qcyc/p0'].dropna()
        filtered_data_CSR = stage_info.loc[mask_after_stage, 'CSR'].dropna()
        filtered_data_qc_2Su = stage_info.loc[mask_after_stage, 'qc/2Su'].dropna()
        filtered_data_qm_2Su = stage_info.loc[mask_after_stage, 'qm/2Su'].dropna()
```

```
137
138
139         total_info = {
140             'Sample type': name,
141             'Stage Number': line_number,
142             'Start index': stage_info.loc[mask_after_stage, 'Start
    index'].min(),
143             'End index': stage_info.loc[mask_after_stage, 'End index'
    ].max(),
144             'Rows nr': stage_info.loc[mask_after_stage, 'Rows nr'].
    sum(),
145             'Star time': stage_info.loc[mask_after_stage, 'Start time
    '].min(),
146             'End time': stage_info.loc[mask_after_stage, 'End time'].
    max(),
147             'Test duration(d)': stage_info['Test duration(d)'].sum(),
148             'Cyclic loading duration(d)': stage_info.loc[
    mask_after_stage, 'Cyclic loading duration(d)'].sum(),
149             'Cycles nr': stage_info.loc[mask_after_stage, 'Cycles nr'
    ].sum(),
150             'Cycle period (s)': stage_info.loc[mask_after_stage, '
    Cycle period (s)'].sum() / filtered_data_Cycleperiod[
    filtered_data_Cycleperiod != 0].shape[0] if
    filtered_data_Cycleperiod[filtered_data_Cycleperiod != 0].shape[0]
     != 0 else 0,
151             'Frequency(Hz)': stage_info.loc[mask_after_stage, '
    Frequency(Hz)'].sum() / filtered_data_Frequency[
    filtered_data_Frequency != 0].shape[0] if filtered_data_Frequency[
    filtered_data_Frequency != 0].shape[0] != 0 else 0,
152             'p_0': stage_info.loc[mask_after_stage, 'p_0'].sum() /
    filtered_data_p_0[filtered_data_p_0 != 0].shape[0] if
    filtered_data_p_0[filtered_data_p_0 != 0].shape[0] != 0 else 0,
153             'q_0': stage_info.loc[mask_after_stage, 'q_0'].sum() /
    filtered_data_q_0[filtered_data_q_0 != 0].shape[0] if
    filtered_data_q_0[filtered_data_q_0 != 0].shape[0] != 0 else 0,
154             'q_m': stage_info.loc[mask_after_stage, 'q_m'].sum() /
    filtered_data_q_m[filtered_data_q_m != 0].shape[0] if
    filtered_data_q_m[filtered_data_q_m != 0].shape[0] != 0 else 0,
155             'q_p': stage_info.loc[mask_after_stage, 'q_p'].sum() /
    filtered_data_q_p[filtered_data_q_p != 0].shape[0] if
    filtered_data_q_p[filtered_data_q_p != 0].shape[0] != 0 else 0,
156             'q_min': stage_info.loc[mask_after_stage, 'q_min'].sum()
    / filtered_data_q_min[filtered_data_q_min != 0].shape[0] if
    filtered_data_q_min[filtered_data_q_min != 0].shape[0] != 0 else
    0,
157             'q_max': stage_info.loc[mask_after_stage, 'q_max'].sum()
    / filtered_data_q_max[filtered_data_q_max != 0].shape[0] if
    filtered_data_q_max[filtered_data_q_max != 0].shape[0] != 0 else
    0,
158             'q_avg': stage_info.loc[mask_after_stage, 'q_avg'].sum()
    / filtered_data_q_avg[filtered_data_q_avg != 0].shape[0] if
    filtered_data_q_avg[filtered_data_q_avg != 0].shape[0] != 0 else
    0,
159             'qcyc': stage_info.loc[mask_after_stage, 'qcyc'].sum() /
    filtered_data_qcyc[filtered_data_qcyc != 0].shape[0] if
    filtered_data_qcyc[filtered_data_qcyc != 0].shape[0] != 0 else 0,
160             'qcyc/p0': stage_info.loc[mask_after_stage, 'qcyc/p0'].
    sum() / filtered_data_qcyc_p0[filtered_data_qcyc_p0 != 0].shape[0]
```

```
    if filtered_data_qcyc_p0[filtered_data_qcyc_p0 != 0].shape[0] != 0 else 0,
            'CSR': stage_info.loc[mask_after_stage, 'CSR'].sum() / filtered_data_CSR[filtered_data_CSR != 0].shape[0] if filtered_data_CSR[filtered_data_CSR != 0].shape[0] != 0 else 0,
            'qc/2Su': stage_info.loc[mask_after_stage, 'qc/2Su'].sum() / filtered_data_qc_2Su[filtered_data_qc_2Su != 0].shape[0] if filtered_data_qc_2Su[filtered_data_qc_2Su != 0].shape[0] != 0 else 0,
            'qm/2Su': stage_info.loc[mask_after_stage, 'qm/2Su'].sum() / filtered_data_qm_2Su[filtered_data_qm_2Su != 0].shape[0] if filtered_data_qm_2Su[filtered_data_qm_2Su != 0].shape[0] != 0 else 0
        }
        total_infos.append(total_info)

    # Create a DataFrame from the list of total information
    total_info_df = pd.DataFrame(total_infos)
    return total_info_df

def calculate_stage_info(df, cycles_data, name, P0q0_stage_nr, qm_stage_nr, qf, Su, line_ranges):
    stage_info = calculate_stage_info_base(df, cycles_data, name, P0q0_stage_nr, qm_stage_nr, qf, Su)
    total_info = calculate_total_info(stage_info, name, line_ranges)
    total_info_df = pd.DataFrame(total_info)
    return total_info_df

""" Filter the outliers in the cycles """

def Filter_outliers(data_x, data_y, f_b):

    ## remove outliers of the cycles when project it on horizontal axis.
    data = list(zip(data_x, data_y))
    q1 = np.percentile(data_x, 25)
    q3 = np.percentile(data_x, 75)

    # Calculate the interquartile range (IQR)
    iqr = q3 - q1
    #lower_bound = q1 - (f_b1 * abs(iqr))
    upper_bound = q3 + (f_b * abs(iqr))

    outlier_data = [(x, y) for x, y in data if x > upper_bound]
    cleaned_data = [(x, y) for x, y in data if x <= upper_bound]

    #outlier_x = [x for x, y in outlier_data]
    #outlier_y = [y for x, y in outlier_data]
    cleaned_x = [x for x, y in cleaned_data]
    cleaned_y = [y for x, y in cleaned_data]

    ###
    ## get angle of max and min values of y.

    # Identify the maximum and minimum points of x_values
    X = np.array(cleaned_x)
    y = np.array(cleaned_y)

```

```
    # Define the model (linear regression)
    X = X.reshape(-1, 1)
    model = LinearRegression()

    # Initialize a large residual_threshold
    residual_threshold = 1000
    max_trials = 1000

    # Iteratively decrease residual_threshold until boundaries are
    captured
    while True:
        ransac = RANSACRegressor(model, min_samples=2,
    residual_threshold=residual_threshold, max_trials=max_trials)
        ransac.fit(X, y)
        inlier_mask = ransac.inlier_mask_
        inlier_x = X[inlier_mask][:, 0]

        # Check if the minimum and maximum x-values are captured
        min_x = np.min(inlier_x)
        max_x = np.max(inlier_x)
        if min_x == np.min(X[:, 0]) and max_x == np.max(X[:, 0]):
           break

        # Decrease residual_threshold if boundaries are not captured
        residual_threshold /= 2

    # Get the fitted line parameters (slope and intercept)
    slope = ransac.estimator_.coef_[0]
    intercept = ransac.estimator_.intercept_

    # Calculate min_y and max_y using the captured boundaries
    min_y = slope * min_x + intercept
    max_y = slope * max_x + intercept

    # Calculate the area of the triangle
    base = abs(max_x - min_x )
    height = abs(max_y - min_y)
    Cx_l  = min_x + base/ 2
    Cy_l  = min_y + height / 2
    angle_in_radians_ = np.arctan(slope)
    prefixed_major_axis_length = np.sqrt(height)**2 + (base)**2
    angle_in_degrees_ = np.degrees(angle_in_radians_)


    return cleaned_x, cleaned_y, min_x, max_x, min_y, max_y, Cx_l,
    Cy_l, angle_in_radians_, angle_in_degrees_,
    prefixed_major_axis_length
```

C.1.3 Calculated propagation errors in LCC17 (used as an example)

```
""" The ingiven Data from lab for the sample and Propogation error in
    Stress, Strain, pwp and deviator stress
"""

""" The peak deviatoric stress (qf ) which is taken from monotonic
   tests, in our study the value is
no available, so the value is taken from previous research project
   which search the same soil and site ((Wong et al., 2023, p. 7)"""
```

```

qf_LCC = np.mean([2.37, 2.53, 1.03, 1.34, 1.92, 2.56]) *1000   ## Unconfined compressive strength  from monotonic test
Su_LCC = qf_LCC / 2    ## the undrained Shear strength from monotonic test


## Poisson's ratio
v = 0.2
#the Uncertainties in the measurements
Ru_d_G = 0.0002      #    Relative Uncertainty in Global displacement sensor
Ru_d_L = 0.00105     #    Relative Uncertainty in Local displacement sensor
Ru_l = 0.00          #    Relative Uncertainty in axial loading sensor
v_error = 0.018      # mm error in vernier caliper
Ru_c3 = 0.0086       #    Relative Uncertainty in cell pressure
Ru_w = 0.0035        #    Relative Uncertainty in pore pressure

H0_LCC17 = 100.98   # mm  initial height
Lg_LCC17 = 48.57  # mm gauge length
D0_LCC17 = 47.82 # mm  initial diameter
A0_LCC17 = A(D0_LCC17)     # m^2
V0_LCC17 = V(A0_LCC17, Lg_LCC17)   # m^3

d_error_LCC = (50-45) / 2 # mm
Ru_A_LCC17 = (2 * d_error_LCC)/(D0_LCC17)    #Relative Uncertainty in Area
Ru_H_G_LCC17 = (v_error/H0_LCC17)  #Relative Uncertainty in change of the hieght of specimne for global strain.
Ru_H_L_LCC17 = (v_error/Lg_LCC17)  #Relative Uncertainty in change of the hieght of specimne for local strain.
Ru_strain_G_LCC17 = np.sqrt(((Ru_d_G)**2) + ((Ru_H_G_LCC17)**2)) # Relative Uncertainty in Global strain
Ru_strain_L_LCC17 = np.sqrt(((Ru_d_L)**2) + ((Ru_H_L_LCC17)**2)) # Relative Uncertainty in Local strain
Ru_stress_LCC17 = np.sqrt(((Ru_l)**2) + ((Ru_A_LCC17)**2)) # Relative Uncertainty in Local stress
Ru_E_G_LCC17 = np.sqrt(((Ru_stress_LCC17)**2) + ((Ru_strain_G_LCC17)**2)) #  Relative Uncertainty in global E
Ru_E_L_LCC17 = np.sqrt(((Ru_stress_LCC17)**2) + ((Ru_strain_L_LCC17)**2))#  Relative Uncertainty in Local E
```

C.1.4 Determine the crossing points in Dataset of LCC17 (used as an example)

```

# Create a new DataFrame for the range of cyclic loading

br1 = 1026     # start index for cyclic loading
br2 = 603708   # end index for cyclic loading
df_range = df_LCC17_P.iloc[br1:br2].copy()

# Calculate the mean value of the 'Deviator Stress (kPa)' column starting from row 1027 (start cycing)
mean_val_LCC17_P = np.mean(df_range.loc[:,'Deviator Stress (kPa)'])

```

```
# Calculate the difference between the mean value.
df_range.loc[:, 'diff'] = df_range.loc[:,'Deviator Stress (kPa)'] - mean_val_LCC17_P

# Find where the difference changes sign (crosses zero)
crossings = np.where(np.diff(np.sign(df_range['diff'])))[0]

# Interpolate to find more accurate crossing points
#Include the first point if the first points of cyclic points are above the mean value so the first cycle cannot be identified without the including.
if df_range.iloc[0]['Deviator Stress (kPa)'] > mean_val_LCC17_P:
    crossing_points = [df_range.iloc[0]['Time since start of test (s)']]
else:
    crossing_points = []
crossing_values = []

for idx in crossings:
    x1, y1 = df_range.iloc[idx]['Time since start of test (s)'], df_range.iloc[idx]['Deviator Stress (kPa)']
    x2, y2 = df_range.iloc[idx+1]['Time since start of test (s)'], df_range.iloc[idx+1]['Deviator Stress (kPa)']
    x = x1 - (y1 - mean_val_LCC17_P) * ((x2 - x1) / (y2 - y1))
    crossing_points.append(x)

# Convert crossing_points to a DataFrame
crossing_df_LCC17 = pd.DataFrame(crossing_points, columns=['corresponding_time'])

## Interpolate the values from 'Deviator Stress (kPa)' at the crossing points
crossing_df_LCC17['corresponding_Deviator_Stress'] = np.interp(crossing_points, df_range.loc[:,'Time since start of test (s)'], df_range.loc[:,'Deviator Stress (kPa)'])
crossing_df_LCC17['crossing_points_number'] = range(1, len(crossing_points) + 1)
#crossing_df_LCC17['time_diff_crossing'] = crossing_df_LCC17['corresponding_time'].diff().fillna(0)

crossing_df_LCC17 = crossing_df_LCC17[['crossing_points_number', 'corresponding_time', 'corresponding_Deviator_Stress']]

# Create a new column 'time of the cycle'
crossing_df_LCC17['Cycle time'] = np.nan

# Calculate the time difference between cycle time
for i in range(0, len(crossing_df_LCC17), 1):
    if i + 1 < len(crossing_df_LCC17):
        time_crossing_diff = crossing_df_LCC17.iloc[i+1]['corresponding_time'] - crossing_df_LCC17.iloc[i]['corresponding_time']
        crossing_df_LCC17.loc[i, 'time_diff_crossing'] = time_crossing_diff

crossing_df_LCC17 = crossing_df_LCC17[['crossing_points_number', 'corresponding_time', 'corresponding_Deviator_Stress', 'time_diff_crossing']]
```

C.1.5 Filter the crossing points if there are short intersections between them (LCC17 used as an example)

```

## Filter crossing_df_LCC17 based on the time difference condition
filtered_crossing_df_LCC17 = pd.DataFrame(columns=['crossing_points_number', 'corresponding_time', 'corresponding_Deviator_Stress', 'time_diff_crossing', 'Cycle time'])

time_threshold = 20  # Set the time threshold in seconds for the diff time in the short intersection

for i in range(len(crossing_df_LCC17)):
    if crossing_df_LCC17.iloc[i]['time_diff_crossing'] >= time_threshold:
        filtered_crossing_df_LCC17 = pd.concat([filtered_crossing_df_LCC17, pd.DataFrame(crossing_df_LCC17.iloc[i,:]).T], ignore_index=True)

# Reset the index and crossing_points_number column
filtered_crossing_df_LCC17 = filtered_crossing_df_LCC17.reset_index(drop=True)
filtered_crossing_df_LCC17['crossing_points_number'] = range(1, len(filtered_crossing_df_LCC17) + 1)


# Calculate the time difference between cycle time
for i in range(0, len(filtered_crossing_df_LCC17), 2):
    if i + 2 < len(filtered_crossing_df_LCC17):
        time_cycle_diff = filtered_crossing_df_LCC17.iloc[i+2]['corresponding_time'] - filtered_crossing_df_LCC17.iloc[i]['corresponding_time']
        filtered_crossing_df_LCC17.loc[i, 'Cycle time'] = time_cycle_diff




""" The cycles below identified from the last code which these cycles cannot be fitted as ellipse"""
pairs_to_remove = []

# Divide the data into cycles and produce a new dataframe "df_cycles_LCC17" that has columns for cycle nr
pairs_LCC17 = [(filtered_crossing_df_LCC17.loc[i,'corresponding_time'], filtered_crossing_df_LCC17.loc[i+2,'corresponding_time']) for i in range(0, len(filtered_crossing_df_LCC17)-2, 2)]

# Filter pairs with at least 5 indices and exclude pairs in pairs_to_remove
filtered_pairs_LCC17 = []
for i, (start_index, end_index) in enumerate(pairs_LCC17):
  cycle_indices = df_LCC17_P[df_LCC17_P['Time since start of test (s)'].between(start_index, end_index)].index
  if len(cycle_indices) >= 4 and i not in pairs_to_remove:  # Check for both conditions
    filtered_pairs_LCC17.append((start_index, end_index))
```

```
37
38 cycles_LCC17 = []
39 for start_index, end_index in filtered_pairs_LCC17:
40     cycle_indices = df_LCC17_P[(df_LCC17_P['Time since start of test
    (s)'] >= start_index) & (df_LCC17_P['Time since start of test (s)'
    ] <= end_index)].index
41     time_cycle_index = filtered_crossing_df_LCC17[
    filtered_crossing_df_LCC17['corresponding_time'] == start_index].
    index[0]
42     time_cycle_value = filtered_crossing_df_LCC17.loc[
    time_cycle_index, 'Cycle time']
43     df_LCC17_P.loc[cycle_indices, 'Cycle time'] = time_cycle_value
44     df_LCC17_P.loc[cycle_indices, 'Cycle nr'] = len(cycles_LCC17) + 1
45     cycle_LCC17 = df_LCC17_P[df_LCC17_P['Cycle nr'] == len(
    cycles_LCC17) + 1]
46     cycles_LCC17.append(cycle_LCC17)
47
48 # Reorder columns in df_LCC17_P
49 cols = df_LCC17_P.columns.tolist()
50 cols.insert(1, cols.pop(cols.index('Cycle nr')))
51 cols.append(cols.pop(cols.index('Cycle time')))
52 df_LCC17_P = df_LCC17_P[cols]
53
54 # Reorder columns in cycles_LCC17
55 for i, cycle in enumerate(cycles_LCC17):
56     cols = cycle.columns.tolist()
57     cols.insert(1, cols.pop(cols.index('Cycle nr')))
58     cols.append(cols.pop(cols.index('Cycle time')))
59     cycles_LCC17[i] = cycle[cols]
60
61 df_LCC17_new = df_LCC17_P.copy()
62
63 """ Export this DataFrame to a CSV file """
64 Path_df_LCC17_new = os.path.join('Outputs_csv', 'df_LCC17_new.csv')
65 df_LCC17_new.to_csv(Path_df_LCC17_new, index=False)
```

C.1.6 Global Stress-Strain Cycle - Fit Ellispe (LCC17 used as an example)

```
1 # For each loop, get the start and end times
2 #plt.figure(figsize=(10, 6))
3 f_b = 100
4 cycle_info_LCC17 = []
5 for n, loop in enumerate(cycles_LCC17):
6   try:
7     start_time = loop.iloc[0,2]
8     end_time = loop.iloc[-1,2]
9
10
11     x_values = cycles_LCC17[n]['Global Axial Strain'].tolist()     ##
     Axial Strain
12     y_values = cycles_LCC17[n]['Deviator Stress (kPa)'].tolist()
    ## Axial Stress kPa
13
14     ## the cycle amplitude
15     qmax = np.max(cycles_LCC17[n]['Deviator Stress & Uncertainty (kPa
    )'])
16     qmin = np.min(cycles_LCC17[n]['Deviator Stress & Uncertainty (kPa
```

```
    )'])
    qcyc = (qmax - qmin) / 2


    ## Excess pore water pressure
    pwp =  umean(cycles_LCC17[n]['Pore Pressure & Uncertainty (kPa)'
    ])
    pwp0 = umean(cycles_LCC17[0]['Pore Pressure & Uncertainty (kPa)'
    ])
    delta_pwp = pwp - pwp0


    ## Loading period T and Frequency of loading f
    Tmax = np.max(cycles_LCC17[n]['Time since start of test (s)'])
    Tmin = np.min(cycles_LCC17[n]['Time since start of test (s)'])
    T = Tmax - Tmin
    f = 1 / T

    ################################
    # Ellipse calculation    #######
    ################################
    ########################################

    ###############
    # Filter the outliers in the cycle
    ########################################
    x_o, y_o, min_x, max_x, min_y, max_y, Cx_l, Cy_l,
    angle_in_radians, angle_in_degrees, prefixed_major_axis_length = (
    Filter_outliers(x_values, y_values, f_b) )

    ########################################
    # Plot the fit ellipse   ################
    ########################################

    # Fit an ellipse model using RANSAC
    model = EllipseModel()
    points = np.column_stack((x_o, y_o))
    model.estimate(points)
    center = model.params[0:2]
    center_projection_x = center[0]
    center_projection_y = center[1]
    major_axis_length = model.params[2] * 2
    minor_axis_length = model.params[3] * 2
    angle = np.degrees(model.params[4])
    prefixed_minor_axis_length = minor_axis_length * (
    prefixed_major_axis_length / major_axis_length )

    ## The centriod and lateral values with uncertainty
    Error_C_x = abs(Cx_l * Ru_strain_G_LCC17)
    Error_C_y = abs(Cy_l * Ru_stress_LCC17)

    C_X = ufloat(Cx_l, Error_C_x) * 100  ##       %
    C_Y_MPa = ufloat(Cy_l, Error_C_y) /1000  ## MPa


    height_y = abs(max_y - min_y)
    height_y_MPa = height_y / 1000     ## MPa
    width_x  = abs(max_x - min_x)
```

```
70
71      E =  height_y_MPa / width_x  ## MPa
72      E_error = E *  Ru_E_G_LCC17
                              ####
73      E_U = ufloat(E, E_error)
74
75      ellipse_area = np.pi * prefixed_major_axis_length *
        prefixed_minor_axis_length / 4
76      tri_area = 0.5 * (height_y) * (width_x)
77      damping_ratio = (1/np.pi) * (ellipse_area/tri_area)
78
79      shear_modulus_mPa = E / (2*(1+v))  ## MPa
80
81      shear_strain = (1+v) * C_X  ## %       = (1+v)         Shear strain
82      shear_stress_mPa = C_Y_MPa / 2    ##        =      /2   Shear
        stress
83
84      CSR      = qcyc / (2* qf_LCC)
85      qcyc_po  = qcyc / (Stage_info_LCC17.loc[0]['p_0'])
86      qcyc_2su = qcyc / (2 * Su_LCC)
87      qm_2su   = Stage_info_LCC17.loc[0]['q_m'] / (2 * Su_LCC)
88
89
90      # Append the loop information to the list
91      cycle_info_LCC17.append([n+1, start_time, end_time, ellipse_area,
         tri_area, damping_ratio, C_X, C_Y_MPa, width_x, height_y_MPa,
        shear_strain, shear_stress_mPa, E, E_error, E_U, shear_modulus_mPa
        , qmax, qmin, qcyc, pwp, delta_pwp, qm_2su, qcyc_2su, qcyc_po, CSR
        , T, f])
92
93      #plt.scatter(Cx_l, Cy_l, s=10, c='r', marker='o', zorder=2)
94      #ellipse_cstr = Ellipse(xy =(Cx_l, Cy_l), width=
        prefixed_major_axis_length, height=prefixed_minor_axis_length,
        angle=angle_in_degrees, edgecolor='b', fill = False, label='Fitted
         Ellipse', zorder=1)
95      #plt.gca().add_patch(ellipse_cstr)
96
97    except Exception as e:  # Catch any exceptions during processing
98     print(f"Error encountered for loop {n}: {e}")
99     pass  # Continue to the next loop iteration
100
101 #plt.gca().xaxis.set_major_formatter(FuncFormatter(lambda x, pos: f'{
       x*100:.2f}%'))  # Format ticks as percentages
102 #plt.xlabel('Axial strain [%]')
103 #plt.ylabel('Axial stress [kPa]')
104 #plt.title(f"Axial strain [%] vs Axial stress [kPa] for {n+1} cycles
       - sample LCC17 - Global")
105 #plt.grid(True)
106 #plt.show()
107
108 # Convert loop_info to a DataFrame
109 cycle_info_LCC17_G  = pd.DataFrame(cycle_info_LCC17[:], columns=['
       Loop_Number', 'Start_Time', 'End_Time', 'Ellipse_area', '
       Triangle_area', 'Damping_ratio', 'C_X(%)' ,'C_Y(MPa)', 'Delta_x',
       'Delta_y(MPa)', 'Shear Strain', 'Shear Stress(mPa)', 'E(MPa)', '
       E_error', 'E_u (MPa)', 'Shear_modulus_(MPa)', 'qmax', 'qmin', '
       qcyc', 'pwp', 'delta_pwp', 'qm/2su', 'qcyc/2su', 'qcyc/po', 'CSR',
        'T_(s)', 'f(Hz)'])
```

```

# Split the DataFrame into two parts
split_index = 10065
cycle_info_LCC17_G_1 = cycle_info_LCC17_G.iloc[:split_index]
cycle_info_LCC17_G_2 = cycle_info_LCC17_G.iloc[split_index:]

# Export this DataFrame to a CSV file
Path_cycle_info_LCC17_G = os.path.join('Outputs_csv', '
    cycle_info_LCC17_G.csv')
cycle_info_LCC17_G.to_csv(Path_cycle_info_LCC17_G, index=False)
```

C.1.7 Local Stress-Strain Cycle - Fit Ellispe (LCC17 used as an example)

```
# For each loop, get the start and end times
#plt.figure(figsize=(10, 6))
f_b = 100

cycle_info_LCC17 = []
for n, loop in enumerate(cycles_LCC17):
  try:
    start_time = loop.iloc[0,2]
    end_time = loop.iloc[-1,2]


    x_values = cycles_LCC17[n]['Local Axial Strain'].tolist()     ##
    Axial Strain
    y_values = cycles_LCC17[n]['Deviator Stress (kPa)'].tolist()
    ## Axial Stress kPa

    ## the cycle amplitude
    qmax = np.max(cycles_LCC17[n]['Deviator Stress & Uncertainty (kPa
    )'])
    qmin = np.min(cycles_LCC17[n]['Deviator Stress & Uncertainty (kPa
    )'])
    qcyc = (qmax - qmin) / 2


    ## Excess pore water pressure
    pwp =  umean(cycles_LCC17[n]['Pore Pressure & Uncertainty (kPa)'
    ])
    pwp0 = umean(cycles_LCC17[0]['Pore Pressure & Uncertainty (kPa)'
    ])
    delta_pwp = pwp - pwp0


    ## Loading period T and Frequency of loading f
    Tmax = np.max(cycles_LCC17[n]['Time since start of test (s)'])
    Tmin = np.min(cycles_LCC17[n]['Time since start of test (s)'])
    T = Tmax - Tmin
    f = 1 / T



    ################################
    # Ellipse calculation    #######
    ################################
    ########################################
```

```
39
40      ###############
41      # Filter the outliers in the cycle
42      ########################################
43      x_o, y_o, min_x, max_x, min_y, max_y, Cx_l, Cy_l,
        angle_in_radians, angle_in_degrees, prefixed_major_axis_length = (
44      Filter_outliers(x_values, y_values, f_b) )
45
46      ########################################
47      # Plot the fit ellipse   ################
48      ########################################
49
50      # Fit an ellipse model using RANSAC
51      model = EllipseModel()
52      points = np.column_stack((x_o, y_o))
53      model.estimate(points)
54      center = model.params[0:2]
55      center_projection_x = center[0]
56      center_projection_y = center[1]
57      major_axis_length = model.params[2] * 2
58      minor_axis_length = model.params[3] * 2
59      angle = np.degrees(model.params[4])
60      prefixed_minor_axis_length = minor_axis_length * (
        prefixed_major_axis_length / major_axis_length )
61
62      ## The centriod and lateral values with uncertainty
63      Error_C_x = abs(Cx_l * Ru_strain_L_LCC17)
64      Error_C_y = abs(Cy_l * Ru_stress_LCC17)
65
66
67      C_X = ufloat(Cx_l, Error_C_x) * 100  ##       %
68      C_Y_MPa = ufloat(Cy_l, Error_C_y) /1000  ## MPa
69
70
71      height_y = abs(max_y - min_y)
72      height_y_MPa = height_y / 1000     ## MPa
73      width_x  = abs(max_x - min_x)
74
75      E =  height_y_MPa / width_x  ## MPa
76      E_error = E *  Ru_E_L_LCC17
                              ####
77      E_U = ufloat(E, E_error)
78
79      ellipse_area = np.pi * prefixed_major_axis_length *
        prefixed_minor_axis_length / 4
80      tri_area = 0.5 * (height_y) * (width_x)
81      damping_ratio = (1/np.pi) * (ellipse_area/tri_area)
82
83      shear_modulus_mPa = E / (2*(1+v))  ## MPa
84
85      shear_strain = (1+v) * C_X  ## %      = (1+v)        Shear strain
86      shear_stress_mPa = C_Y_MPa / 2    ##       =      /2   Shear
        stress
87
88
89      CSR      = qcyc / (2* qf_LCC)
90      qcyc_po  = qcyc / (Stage_info_LCC17.loc[0]['p_0'])
91      qcyc_2su = qcyc / (2 * Su_LCC)
```

```
    qm_2su    = Stage_info_LCC17.loc[0]['q_m'] / (2 * Su_LCC)


    # Append the loop information to the list
    cycle_info_LCC17.append([n+1, start_time, end_time, ellipse_area,
     tri_area, damping_ratio, C_X, C_Y_MPa, width_x, height_y_MPa,
    shear_strain, shear_stress_mPa, E, E_error, E_U, shear_modulus_mPa
    , qmax, qmin, qcyc, pwp, delta_pwp, qm_2su, qcyc_2su, qcyc_po, CSR
    , T, f])


    #plt.scatter(Cx_l, Cy_l, s=10, c='r', marker='o', zorder=2)
    #ellipse_cstr = Ellipse(xy =(Cx_l, Cy_l), width=
    prefixed_major_axis_length, height=prefixed_minor_axis_length,
    angle=angle_in_degrees, edgecolor='b', fill = False, label='Fitted
     Ellipse', zorder=1)
    #plt.gca().add_patch(ellipse_cstr)

  except Exception as e:  # Catch any exceptions during processing
   print(f"Error encountered for loop {n}: {e}")
   pass  # Continue to the next loop iteration

#plt.gca().xaxis.set_major_formatter(FuncFormatter(lambda x, pos: f'{
    x*100:.2f}%'))  # Format ticks as percentages
#plt.xlabel('Axial strain [%]')
#plt.ylabel('Axial stress [kPa]')
#plt.title(f"Local - Axial strain [%] vs Axial stress [kPa] for {n+1}
     loops - sample LCC17")
#plt.grid(True)
#plt.show()

# Convert loop_info to a DataFrame
cycle_info_LCC17_L = pd.DataFrame(cycle_info_LCC17, columns=['
    Loop_Number', 'Start_Time', 'End_Time', 'Ellipse_area', '
    Triangle_area', 'Damping_ratio', 'C_X(%)', 'C_Y(MPa)', 'Delta_x',
    'Delta_y(MPa)', 'Shear Strain', 'Shear Stress(MPa)', 'E(MPa)', '
    E_error', 'E_U(MPa)', 'Shear_modulus_(MPa)', 'qmax', 'qmin', 'qcyc
    ', 'pwp', 'delta_pwp', 'qm/2su', 'qcyc/2su', 'qcyc/po', 'CSR', 'T_
    (s)', 'f(Hz)'])

# Split the DataFrame into two parts
split_index = 10065
cycle_info_LCC17_L_1 = cycle_info_LCC17_L.iloc[:split_index]
cycle_info_LCC17_L_2 = cycle_info_LCC17_L.iloc[split_index:]


Path_cycle_info_LCC17_L = os.path.join('Outputs_csv', '
    cycle_info_LCC17_L.csv')
cycle_info_LCC17_L.to_csv(Path_cycle_info_LCC17_L, index=False)

cycle_info_LCC17_L_2
```

DEPARTMENT OF ARCHITECTURE AND
CIVIL ENGINEERING
CHALMERS UNIVERSITY OF TECHNOLOGY
Gothenburg, Sweden 2024
www.chalmers.se

CHALMERS
UNIVERSITY OF TECHNOLOGY